Electronic properites of MoS2/MoSe2 van der Waals heterostructures

Zhang Nan

Université Fédérale
Toulouse Midi-Pyrénées

THÈSE

En vue de l'obtention du

DOCTORAT DE L'UNIVERSITÉ DE TOULOUSE

Délivré par l'Institut National des Sciences Appliquées de Toulouse

Présentée et soutenue par

NAN ZHANG

Le 10 décembre 2020

Propriétés électroniques de MoS2 / MoSe2van der Waals heterostructures

Ecole doctorale : **SDM - SCIENCES DE LA MATIERE - Toulouse**

Spécialité : **Nanophysique**

Unité de recherche :
LNCMI - Laboratoire National des Champs Magnétiques Intenses

Thèse dirigée par
Duncan MAUDE et Paulina PLOCHOCKA

Jury

M. Mark GOERBIG, Rapporteur
M. Grzegorz SEK, Rapporteur
M. Adnen Mlayah, Examinateur
M. Wilfried Desrat, Examinateur
M. Duncan MAUDE, Directeur de thèse
Mme Paulina PLOCHOCKA, Co-directrice de thèse

THÈSE

En vue de l'obtention du

DOCTORAT DE L'UNIVERSITÉ DE TOULOUSE

délivré par Institut national des sciences appliquées de Toulouse
Spécialité : Nano physique

Présentée et soutenue par

Nan ZHANG

Electronic properties of $MoS_2/MoSe_2$ van der Waals heterostructures

---

Ecole doctorale : Science de la Matière
Unité de recherche : Laboratoire National des Champs Magnétiques Intenses
Directeurs de Thèse : Paulina PLOCHOCKA et Duncan MAUDE

Electronic properties of $MoS_2/MoSe_2$ van der Waals heterostructures

Abstract: The thesis starts with the general overview of the properties of transition metal dichalcogenides monolayers and their heterostructures. This is followed by the detailed description experimental techniques which were used to characterize photo-response of heterostructures and their preparation.

In chapter 3 the impact of photodoping on the interlayer exciton emission properties is presented. The photodoping is identified by the increasing (upon illumination) trion dissociation energy, accompanied by a characteristic change of the exciton/trion photoluminescence intensity ratio in $MoSe_2$. At the same time, the photoluminescence intensity of the interlayer exciton decreases. This is accompanied by an enhancement of the combined PL intensity of the exciton and the trion in $MoSe_2$, showing that the interlayer charge transfer can be controlled by the doping level. This effect is persistent on a timescale of several hours, as long as the sample is maintained under vacuum. This indicates a mechanism involving laser induced desorption of molecules physisorbed on the surface of the heterostructure. This hypothesis is supported by the observed sensitivity of the photodoping rate on the excitation wavelength. The process of photodoping is much faster for higher energy photons.

Chapter 4 presents the impact of the moiré pattern on the intralayer exciton spectrum in $MoS_2/MoSe_2$ heterostructure. A moiré pattern forms in van der Waals stacks due to the weak interlayer interaction which allows the layers preserve their own lattice parameters. A small twist angle, or lattice mismatch between the layers, induces a periodic spatially varying potential. The relative orientation of the flakes in the investigated heterostructure has been determined using second harmonic generation spectroscopy. Experimental evidence is presented for the impact of the moiré pattern on the intralayer emission in a $MoSe_2/MoS_2$ heterobilayer encapsulated in hexagonal boron nitride. The periodic in-plane potential results in a splitting of the $MoSe_2$ exciton and trion in emission and which seen also in the absorption spectra of the exciton. The observed energy difference between the split peaks is fully consistent with theoretical predictions.

Chapter 5 reports the impact of sample quality, and the possibility to generate valley polarization using magnetic field. Three types of structures are compared, namely, CVD grown and h-BN encapsulated $MoSe_2$, together with $MoSe_2/MoS_2$ heterostructure. The magneto-optical data suggest that the formation of moire pattern has negligible impact on the Landé g-factor of the intralayer excitonic transition.

Keywords: Emerging Nano-materials, monolayer transition metal-dichalcogenides (MoS_2; WS_2; $MoSe_2$; WSe_2), magnetophotoluminescence

Resumé: La thèse commence par un aperçu général des propriétés des monocouches de dichalcogénures de métaux de transition et de leurs hétérostructures. Ceci est suivi par la description détaillée des techniques expérimentales qui ont été utilisées pour caractériser la photo-réponse des hétérostructures et leur préparation.

Dans le chapitre 3, l'impact de la photo-génération sur les propriétés d'émission des excitons intercouches est présenté. La photo-génération est identifiée par l'augmentation de l'énergie de dissociation du trion (lors de l'illumination), accompagnée d'un changement caractéristique du rapport d'intensité de photoluminescence exciton/trion dans $MoSe_2$. Dans le même temps, l'intensité de photoluminescence de l'exciton intercouche diminue. Ceci s'accompagne d'une augmentation de l'intensité PL combinée de l'exciton et du trion dans MoSe2, montrant que le transfert de charge intercouche peut être contrôlé par le niveau de dopage. Cet effet est persistant sur une échelle de temps de plusieurs heures, tant que l'échantillon est maintenu sous vide. Ceci indique un mécanisme impliquant une désorption induite par laser des molécules physisorbées à la surface de l'hétérostructure. Cette hypothèse est étayée par la sensibilité observée du taux de photo-génération sur la longueur d'onde d'excitation. Le processus de photo-génération est beaucoup plus rapide pour les photons d'énergie plus élevée.

Le chapitre 4 présente l'impact du motif moiré sur le spectre d'exciton intracouche dans l'hétérostructure $MoS_2/MoSe_2$. Un motif moiré se forme dans les empilements de van der Waals en raison de la faible interaction entre les couches qui permet aux couches de conserver leurs propres paramètres de réseau. Un petit angle de torsion, ou une discordance de réseau entre les couches, induit un potentiel périodique variable dans l'espace. L'orientation relative des flocons dans l'hétérostructure étudiée a été déterminée en utilisant la spectroscopie de deuxième génération d'harmoniques. Des preuves expérimentales sont présentées pour l'impact du modèle de moiré sur l'émission intralayer dans une couche $MoSe_2/MoS_2$ hétérobilayer encapsulée dans du nitrure de bore hexagonal. Le potentiel périodique dans le plan se traduit par un clivage du $MoSe_2$ exciton et du trion en émission et qui se voit également dans les spectres d'absorption de l'exciton. La différence d'énergie observée entre les pics divisés est tout à fait conforme aux prévisions théoriques.

Le chapitre 5 rend compte de l'impact de la qualité des échantillons et de la possibilité de générer une polarisation de vallée à l'aide d'un champ magnétique. Trois types de structures sont comparés, à savoir, le $MoSe_2$ (croissance CVD) et le $MoSe_2$ encapsulé par h-BN, ainsi que l'hétérostructure $MoSe_2/MoS_2$. Les données magnéto-optiques suggèrent que la formation du motif moiré a un impact négligeable sur le facteur g de Landé de la transition excitonique intracouche.

Mots-clés: Emerging nanomatériaux, transition monocouche métal-dichalcogénures (MoS_2; WS_2; $MoSe_2$; WSe_2), magnétophotoluminescence

Acknowledgements

I am profoundly grateful to my supervisors Paulina Plochocka and Duncan Maude, whose illuminating instruction and expert advice have guided me through every step of my PhD thesis. They gave me lots of inspiration and encouragement. They provided me an excellent experiment platform which supported my PhD study. Furthermore, their sense of humor makes a relaxed working environment.

I would like to thank the members of the jury for their valuable comments on this research.

I would like to acknowledge all my collaborators, Andras Kis, Dumitru Dumcenco Rebecca and Yen-Cheng Kung (École Polytechnique Fédérale de Lausanne), Andres Castellanos-Gomez and Patricia Gant (ICMM, Madrid), P.C.M.Christianen, Anatolie Mitioglu, Marion Severijnen (HMFL, Nijmegen), Lukasz Klopotowski (Polish Academy of Sciences), for their excellent experimental work and enjoyable discussion.

I would also like to thank my colleagues in the Laboratoire National des Champs Magnétiques Intenses (LNCMI-Toulouse), who were always very kind and helpful. The formor Postdocs, Alessandro Surrente, Michal Baranowski and the current Postdoc, Mateusz Dyksik helped me a lot with solving the problems in experiments, data analysis and paper writing. Thanks to Krzysztof Galkowski, Zhuo Yang, Joanna Urban, Miriam Karpinska and Shuli Wang for all the help during my stay in Toulouse. Thanks to all the engineers in LNCMI-Toulouse for helping to solve the technical problems during measurements. Thanks to the secretaries in the lab for helping me solve the administration issues. I would also like to acknowledge, the director and deputy director of the LNCMI, Geert Rikken and Oliver Portugall.

Finally, a great thanks to China Scholarship Council for awarding the scholarship, which supported my study in France as a PhD student.

Nan Zhang
Toulouse, December 2020

Resumé de la thèse en francais

Introduction

Aujourd'hui, l'humanité dépend "d'outils" pour traiter et stocker des informations telles que les ordinateurs, les smartphones et de nombreux autres appareils électroniques. Tous ces appareils utilisent des composants semi-conducteurs tels que des transistors, des diodes, des lasers pour leur fonctionnement. Par conséquent, les technologies des semi-conducteurs sont l'un des piliers du développement de la civilisation moderne. De nos jours, l'électronique est dominée par les technologies silicium, III-V et II-VI, qui approchent de leurs limites de performances liées aux propriétés fondamentales de ces matériaux. Pour cette raison, les scientifiques font encore des efforts pour développer davantage la technologie des semi-conducteurs. En particulier, ils recherchent de nouveaux matériaux semi-conducteurs dont les propriétés permettront de traiter de manière plus efficace.

L'une des directions les plus explorées est liée aux cristaux de van der Waals, des matériaux qui sont des sortes de puits quantiques "naturels" de l'épaisseur des atomes simples. Par conséquent, ils représentent la limite ultime de quantification dans une direction. Les dichalcogénures de métaux de transition appartiennent au groupe des matériaux bidimensionnels qui font l'objet d'un intérêt particulier en raison de la structure de bande unique qui offre un potentiel unique pour coder huit bits d'information, (au lieu de deux) par un seul porteur de charge. Ceci est dû au degré de liberté supplémentaire donné par l'indice de spin et de vallée qui peut être relativement facilement contrôlé dans ces matériaux sous leur forme monocouche. Nous espérons que tout cela nous permettra de traiter plus d'informations en moins de temps et avec moins de consommation d'énergie. L'utilisation de degrés de liberté électroniques supplémentaires peut aider à développer l'électronique au-delà des limites fixées par la loi de Moore.

Diachalcogénures de métaux de transition semi-conducteurs

Les dichalcogénures de métaux de transition semi-conducteurs (TMDC) sont une famille représentative de matériaux atomiquement minces. Ils sont caractérisés par la formule générale MX_2, où M désigne un atome de métal de transition du groupe VI, et X correspond à un atome de chalcogène (M = Mo, W; X = S, Se). Une monocouche de MX_2 a l'arrangement X-M-X. L'atome de métal est situé au centre de la cellule unitaire prismatique trigonale liée à six atomes de chalcogène via de fortes liaisons covalentes. Les monocouches sont empilées ensemble via de faibles forces de van der Waals. La symétrie d'inversion est rompue pour les monocouches, mais est restaurée dans des matériaux massifs [Zeng 2015].

Les calculs de structure de bande pour le MoS_2 massif et quelques couches de MoS_2 montrent que le minimum de la bande de conduction (CBM) est situé en un

point entre les points K et Γ dans la zone de Brillouin, et le maximum de la bande de valence (VBM) est situé au point Γ [Kobayashi 1995]. Ainsi, les TMDC massifs et multicouches ont une bande interdite indirecte, comme le montre la figure 1(a-c). Dans le cas d'une monocouche, la bande interdite est directe et située aux points K correspondant aux coins de la zone hexagonale de Brillouin, comme le montre la figure 1(d) [Splendiani 2010].

De plus, les calculs de la théorie fonctionnelle de la densité (DFT) révèlent que la bande interdite directe au point K de la zone de Brillouin change à peine en fonction du nombre de couches, alors que la bande interdite indirecte augmente de manière monotone à mesure que le nombre de couches diminue, comme le montre la figure 1. La nature directe de la bande interdite dans les monocouches a d'abord été suggérée pour expliquer l'émergence observée d'une forte émission de photoluminescence dans la monocouche MoS_2 [Mak 2010, Splendiani 2010]. Le croisement d'un semi-conducteur à bande interdite indirecte à un matériau à gap direct avec diminution du nombre de couches (N) a été démontré expérimentalement [Mak 2010]. Les résultats préliminaires obtenus pour MoS2 ont été très rapidement généralisés à d'autres membres de la famille des TMDC, comme $MoSe_2$, WS2 ou WSe2 [Zhao 2013, Tonndorf 2013].

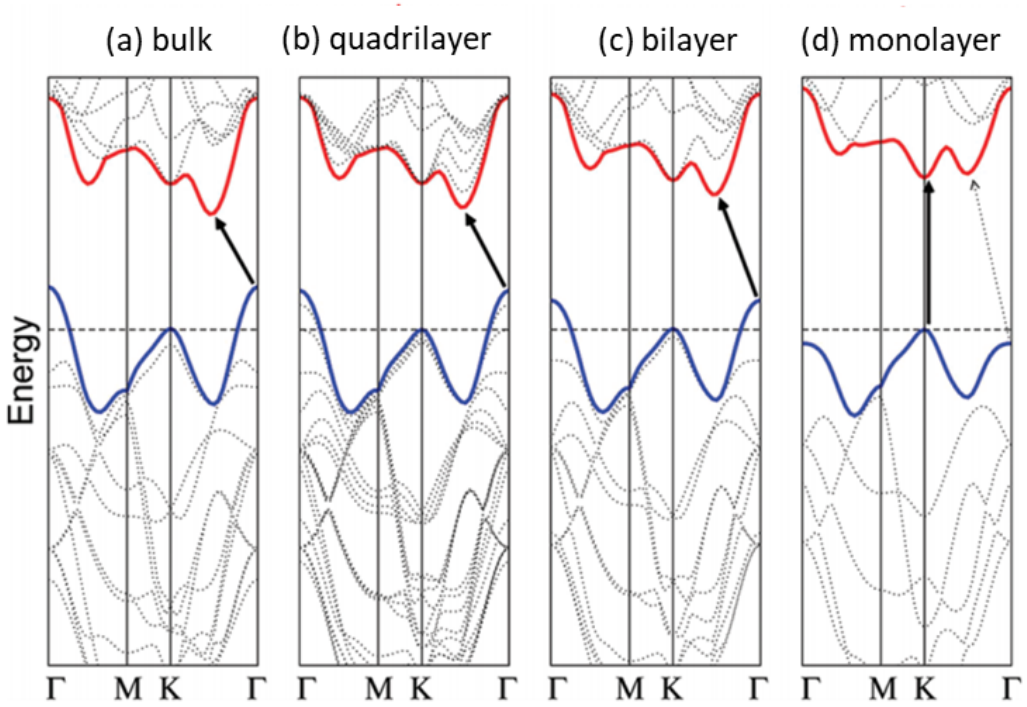

Figure 1: Structures de bande calculées de (a) massif, (b) quadricouche, (c) bicouche et (d) monocouche MoS_2. [Splendiani 2010].

Une autre particularité des TMDC monocouches est la symétrie d'inversion brisée; les deux vallées ne sont pas équivalentes aux points K et $-K$ de la zone de

Brillouin hexagonale 2D, comme le montre la figure 2(a). La symétrie d'inversion brisée combinée à un couplage spin-orbite (SOC) fort et la présence d'une inversion temporelle, corrèle l'indice de vallée avec l'indice de spin, une propriété communément appelée "verrouillage de vallée et de spin" [Xiao 2012]. Le "verrouillage de vallée et de spin" conduit à des règles de sélection optique dépendant de la vallée, qui sont présentées sur la figure 2(b). Les transitions interbandes aux points K (-K) sont couplées à des photons d'hélicité optique $\sigma+$ ($\sigma-$). Cela offre la possibilité de manipuler le spin du porteur dans une certaine vallée en utilisant une lumière polarisée de manière circulaire. Ainsi, les TMDC atomiquement minces fournissent une plate-forme pour valleytronics et spintronics [Xiao 2012]. Il est possible de pomper optiquement la polarisation de vallée. En effet, les premiers résultats expérimentaux ont été démontrés pour MoS_2 par Mak et ses co-auteurs [Mak 2012] et Kioseoglu et collaborateurs [Kioseoglou 2012]. Cependant, l'efficacité du pompage de la polarisation de vallée dépend fortement de la longueur d'onde d'excitation et d'autres paramètres, tels que le choix du matériau monocouche.

Hétérostructure van der Waals (vdW)

L'un des plus grands avantages des monocouche TMDC est probablement la possibilité de les empiler dans n'importe qu'elle combinaison souhaitée avec d'autres semi-conducteurs sans limitations liées à la caractéristique de mésappariement de réseau pour les cristaux covalents. Par conséquent, l'empilement vertical des monocouches fournit un nouveau terrain de jeu riche qui peut être utilisé pour personnaliser les propriétés donnant lieu à de nouvelles fonctionnalités attrayantes. Dans le cas des hétérostructures semi-conductrices classiques III-V ou II-VI ou groupe IV, les couches constitutives doivent avoir la même constante de réseau (au moins très similaire) pour éviter les contraintes qui détériorent souvent la qualité de telles structures. De plus, les combinaisons de matériaux qui peuvent être empilées tout en conservant une bonne qualité sont très limitées. En revanche, la pléthore de différents matériaux TMDC et autres permet d'adapter ou d'améliorer efficacement les caractéristiques souhaitées des hétérostructures de van der Waals. Par exemple, la prise en sandwich de monocouches de TMDC entre des couches de nitrure de bore hexagonal (hBN) améliore considérablement leurs propriétés optiques et électriques.

Enfin, un phénomène très particulier observé dans les hétérostructures de van der Waals est la formation d'un potentiel de moiré de longue période. En général, un motif moiré est une interférence produite par une superposition de deux grilles, treillis ou gabarits périodiques légèrement différents. La différence de période, d'orientation et/ou de décalage relatif entre les deux gabarits conduit à la formation d'un nouveau motif variant lentement qui est communément appelé franges de moiré. Un exemple très simple est la superposition de deux grilles tournées comme le montre la figure 3.

L'interaction faible de van der Waals fait que, dans les hétérostructures TMDC, chacune des couches conserve sa propre constante de réseau, en d'autres termes les monocouches ne se conforment pas les unes aux autres, ce qui conduit à une nouvelle

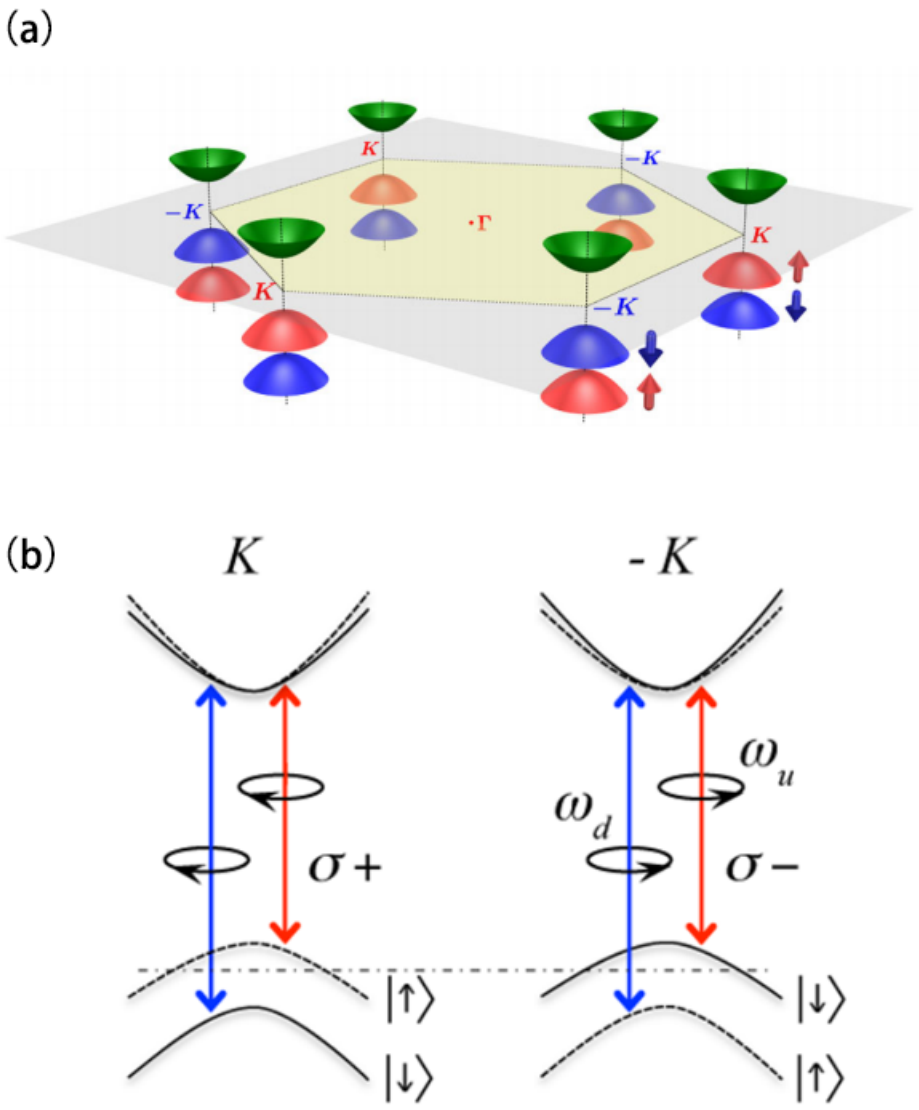

Figure 2: (a) Schéma montrant la structure de la bande situés aux points K. (b) Règles de sélection de transition optique de vallée et de spin. Les courbes pleines (en pointillés) désignent des bandes avec un spin vers le bas (-haute) quantifiée selon la direction hors plan. Le clivage dans la bande de conduction est exagérée. ω_u et ω_d sont, respectivement, les fréquences de transition des deux sommets de bande de valence séparer vers le bas de la bande de conduction [Xiao 2012].

physique extrêmement intéressante. Puisque les deux couches sont des cristaux avec une distribution atomique périodique, toute différence dans les paramètres du réseau

ou l'angle de torsion entre eux entraînera la formation d'un motif moiré [Park 2008].

Ces dernières années, les structures moirées ont suscité un intérêt considérable au sein de la communauté de la physique du solide avec la prise de conscience que les propriétés physiques d'un système peuvent être contrôlées par la torsion des couches. Selon les prévisions théoriques, le modèle de moiré devrait résulter en un potentiel périodiquement modulé. De plus, la variation du potentiel de confinement pour différents registres atomiques devrait conduire à un fractionnement des transitions intra et inter-couches avec la formation d'une matrice efficace de points quantiques en raison du potentiel de moiré périodiquement modulé.

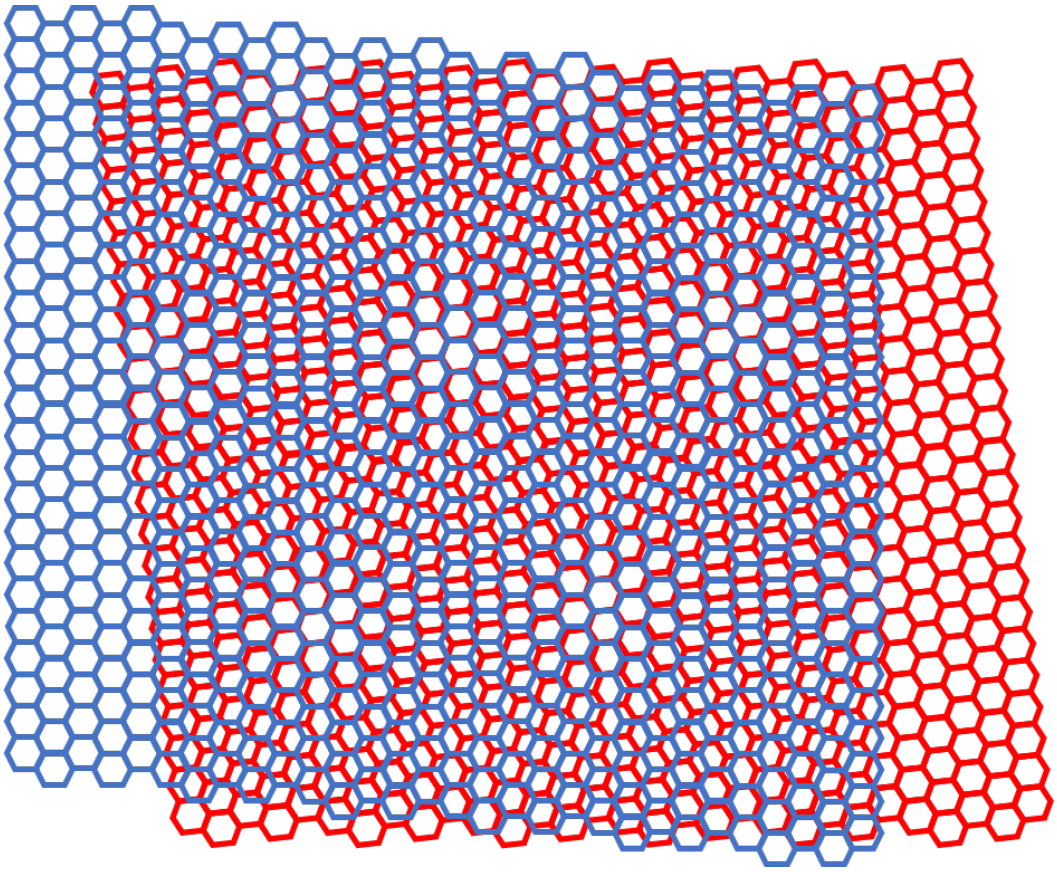

Figure 3: Schéma de la formation du motif moiré pour deux réseaux hexagonaux.

L'effet de photo-génération dans l'hétérostructure $MoSe_2/MoS_2$

Dans les dichalcogénures de métaux de transition monocouches, il a été rapporté que la transition excitonique peut être manipulée optiquement. Dans les monocouches $MoSe_2$ et MoS_2, qui sont intrinsèquement dopées n, un électron en excès peut être lié à un exciton neutre pour former un complexe à trois particules communément

appelé exciton chargé ou trion. L'émission du trion se produit du côté basse énergie de l'émission d'exciton avec une différence d'énergie typique de plusieurs dizaines de meV. La différence d'énergie entre l'exciton et l'émission du trion correspond à l'énergie de liaison du trion. Il a été démontré que la densité de porteurs d'une monocouche de TMDC peut s'accorder dans des conditions ambiantes (c'est-à-dire dans l'air à température ambiante) via la physisorption des molécules H_2O et O_2. Les molécules physisorbées H_2O et O_2 induisent un transfert de charge avec les monocouches TMDC, les électrons sont transférés des monocouches TMDC aux molécules H_2O et O_2 en surface. [Tongay 2013a] a utilisé la physisorption moléculaire comme une grille pour manipuler l'intensité d'émission des excitons. L'intensité photoluminescence des excitons neutres dans MoS_2 peut être augmentée et diminuée par purge et pompage avec H_2O et / ou O_2, respectivement. Cependant, WSe_2, qui est intrinsèquement de type p, montre l'effet inverse. La purge avec H_2O et / ou O_2 entraîne une diminution de l'intensité de l'exciton. Le phénomène inverse observé dans WSe_2 confirme en outre que la physisorption de H_2O et / ou O_2 épuise les électrons.

Photo-génération sur exciton intra-couche de $MoSe_2$

Nous avons commencé par étudier l'influence d'un éclairage laser CW prolongé (puissance de 50μW). Les spectres photoluminescence typiques mesurés en fonction du temps d'exposition au laser sont présentés sur la figure 4(a). Trois pics principaux peuvent être résolus dans les spectres photoluminescence, qui sont attribués à l'émission du trion (T), de l'exciton neutre (X) de $MoSe_2$ et de l'exciton inter-couche (IX) formé à travers l'hétérostructure $MoSe_2$ / MoS_2. Les pics aigus observés du côté basse énergie du trion $MoSe_2$ sont probablement liés aux excitons liés aux défauts [Srivastava 2015a].

Les détails quantifiés sont résumés dans la figure 4. Sur vingt minutes d'éclairage laser, la différence d'énergie entre l'émission d'excitons neutre et chargée augmente linéairement. L'empreinte du changement induit par la lumière dans la densité des porteurs est l'évolution temporelle de l'énergie de dissociation du trion, définie comme la différence d'énergie entre l'exciton et l'émission du trion. Cette grandeur est la somme de l'énergie de liaison du trion E_{TB} (en l'absence d'autres électrons) et de l'énergie de Fermi EF mesurée à partir du bas de la bande de conduction [Huard 2000],

$$E_X - E_T = E_{TB} + E_F.$$

L'augmentation linéaire de l'énergie de dissociation des trions avec le temps, représentée sur la figure 4(b), reflète le déplacement vers le haut du niveau de Fermi, à mesure que la densité des porteurs augmente avec le temps.

Avec l'augmentation du temps d'exposition au laser, l'intensité de l'émission de trion augmente d'environ 50%, tandis que l'intensité de l'émission d'exciton neutre reste plus ou moins inchangée, comme illustré sur la figure 4(c). En revanche, l'intensité de l'émission d'exciton inter-couche diminue d'un facteur quatre.

L'augmentation graduelle de l'intensité relative du trion par rapport à l'exciton, affichée sur la figure 4(d), indique une amélioration progressive de la concentration de porteurs libres, due au photo-dopage, qui augmente la probabilité de former des trions. Comme $MoSe_2$ et MoS_2 sont intrinsèquement dopés n [Lu 2014], l'augmentation monotone observée de l'intensité du trion au fil du temps suggère que les porteurs libres photo-créés sont des électrons. Dans une hétérostructure avec un alignement de bande de type II, l'observation de l'émission d'excitons chargés négativement à partir de $MoSe_2$ peut être contre-intuitive car, en régime permanent, tous les électrons devraient se détendre vers la couche de MoS_2. Nos observations suggèrent que les porteurs libres et les excitons sont photoexcités simultanément. La courte durée de vie radiative des excitons intra-couches dans TMDC [Lagarde 2014b], ainsi que la formation rapide de trions [Singh 2016], permettent à une proportion significative des trions de se recombiner avant le transfert de charge. La présence d'électrons libres dans $MoSe_2$ est liée à la photoionisation des donneurs présents dans ce matériau, de manière similaire à WS_2.

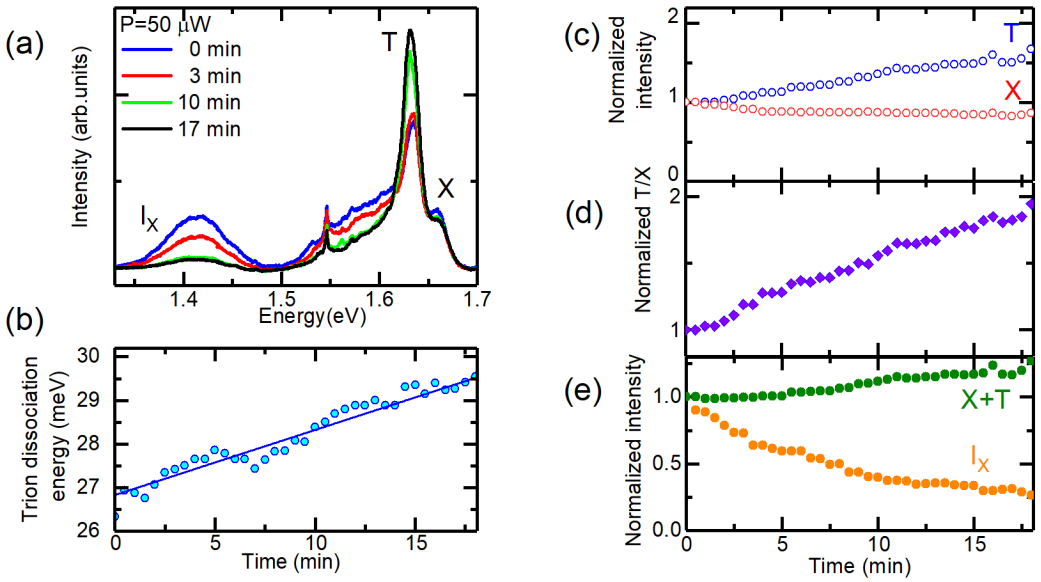

Figure 4: (a) Spectres photoluminescence à basse température acquis après les temps d'exposition laser indiqués montrant les émissions d'excitons chargées (T) et neutres (X) de $MoSe_2$, ainsi que l'émission de l'exciton inter-couche (IX). (b) Évolution temporelle de l'énergie de dissociation du trion (la ligne continue est un ajustement linéaire). (c) Evolution temporelle de l'intensité photoluminescence intégrée des excitons chargés et neutres. (d) Evolution temporelle du rapport d'intensité des excitons neutres et chargés. (e) Évolution temporelle de l'intensité intégrée combinée de l'exciton (X + T) et de l'intensité intégrée de l'exciton inter-couche.

Photo-génération sur exciton inter-couche

L'intensité de l'exciton inter-couche diminue d'un facteur quatre pendant le processus de photo-génération. Nous représentons l'intensité intégrée combinée des excitons chargés et neutres (X + T) en fonction du temps sur la figure 4(e). Contrairement aux monocouches isolées [Currie 2015], l'intensité d'émission des espèces excitoniques intra-couche augmente avec l'augmentation du photo-génération. Ceci est cohérent avec un taux de transfert de charge réduit avec un niveau de photo-génération croissant, ce qui explique également la diminution de l'intensité d'émission d'excitons inter-couche avec l'augmentation du photo-génération. Cet effet pourrait être exploité pour contrôler optiquement l'efficacité du transfert de charge entre les couches en réglant le niveau de photo-génération dans les hétérostructures de van der Waals à base de TMDC. Le poids relatif de l'intensité d'émission intra-couche à inter-couche peut également être contrôlé électrostatiquement, comme précédemment démontré dans une jonction p-n constituée d'une hétérobilayer TMDC [Ross 2017].

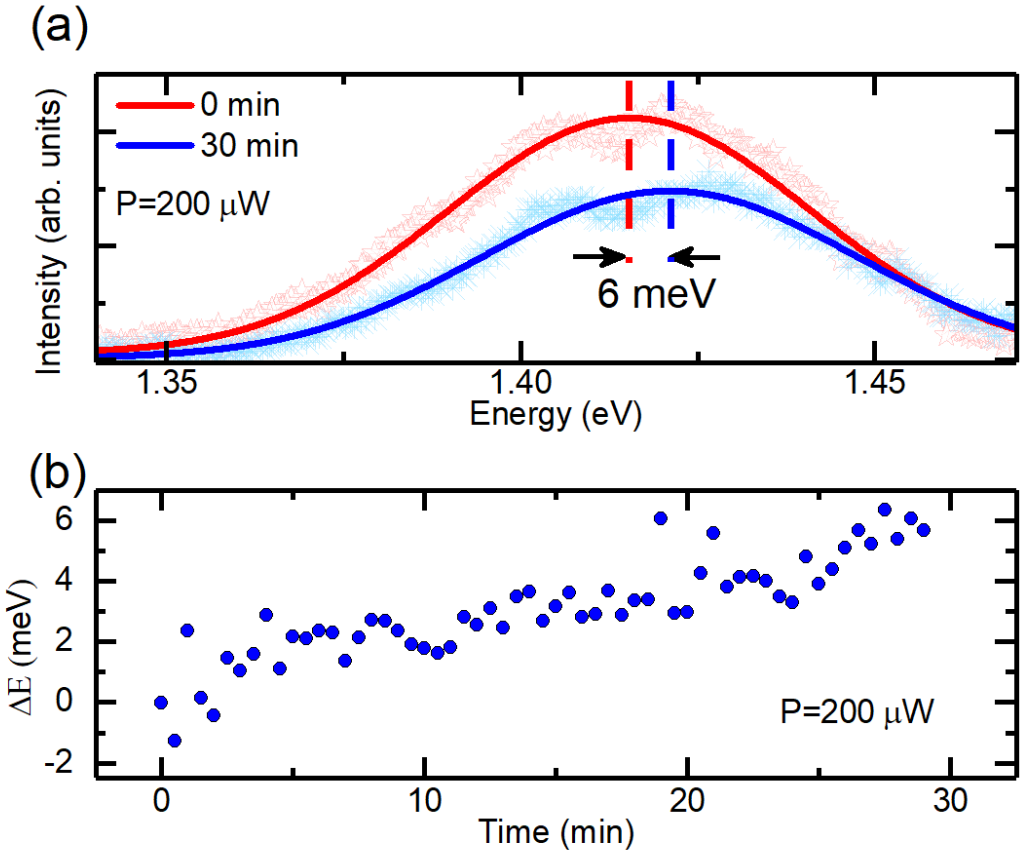

Figure 5: (a) Spectres photoluminescence de l'exciton inter-couche au début et à la fin de l'exposition à un laser haute puissance. (b) Evolution temporelle de l'énergie de l'exciton inter-couche photoluminescence à haute puissance d'excitation.

Nous attribuons provisoirement la diminution de l'efficacité du transfert de charge à la création d'un champ électrique intégré. Ce scénario est également cohérent avec le décalage vers le bleu observé de l'énergie du pic de photoluminescence de l'exciton inter-couche mesurée à une puissance d'excitation élevée ($P = 200\mu$W). Une comparaison du spectre photoluminescence de l'exciton inter-couche au début et à la fin de l'exposition à la lumière laser est représentée sur la figure 5(a), où un décalage bleu de 6 meV est mis en évidence. La dépendance temporelle globale de l'énergie de la transition d'exciton inter-couche est illustrée sur la figure 5(b). Cette tendance est similaire au décalage vers le bleu observé de la transition exciton indirecte dans les puits quantiques de type II avec une puissance d'excitation croissante [Zaitsev 2007], qui résulte des grands champs électriques générés à des concentrations élevées de porteurs. Elle est également en accord avec la baisse récemment observée de l'intensité d'émission des excitons inter-couches dans les hétérostructures avec une grille à la fois pour le dopage de type n et p [Ciarrocchi 2019].

Mécanisme microscopique de photo-génération

Plusieurs mécanismes, tels que la création de lacunes induites par la lumière, l'ionisation des donneurs intrinsèques ou les charges piégées par le substrat, sont considérés comme responsables de la photo-génération dans TMDC. En outre, les TMDC cultivés par CVD sont connus pour héberger une grande concentration de chalcogènes vacants, qui agissent en tant que donneurs. Dans nos hétérostructures, les lacunes Se dans $MoSe_2$ sont partiellement comblées par un transfert de guérison des défauts des atomes S de MoS_2 [Surrente 2017]. Cependant, les postes vacants insaturés pourraient fournir des électrons lors de l'illumination, ce qui conduit à la photo-génération observée. Il est important de noter que les changements observés dans l'échantillon sont persistants, ce qui suggère qu'une exposition prolongée à la lumière laser augmente le nombre de centres de photoionisation. L'intensité relative entre les excitons neutres et chargés ne change pas même après des heures dans l'obscurité, à condition que l'échantillon soit maintenu sous vide. Cependant, le rapport d'intensité trion-exciton observé avant l'exposition à la lumière laser est récupéré après que l'échantillon est exposé à l'air à température ambiante. Cela peut s'expliquer en considérant la physisorption des molécules H_2O et O_2 vers TMDC. Ces deux espèces se lient aux lacunes chalcogènes avec une énergie de liaison de $\simeq 100$ meV et appauvrissent le TMDC naturellement dopé n des électrons [Tongay 2013b]. Lors de l'illumination laser, les trous photogénérés neutralisent les espèces adsorbées, conduisant à leur photodésorption [Zhang 2013]. Ceci explique l'augmentation progressive de la concentration de porteurs libres, ce qui conduit au comportement résumé ci-dessus.

Conclusion

En conclusion, nous avons étudié les effets de la photo-génération persistant sur l'émission d'excitons dans une hétérostructure $MoS_2/MoSe_2/MoS_2$. Une exposition prolongée à la lumière laser augmente le nombre de centres de photoionisation présents, augmentant constamment l'effet de photo-génération (nombre d'électrons photoionisés dynamiquement dans la bande de conduction), à condition que l'échantillon soit maintenu sous vide. Cela suggère que l'effet est lié à la désorption induite par laser des molécules d'eau ou d'oxygène de la surface. L'impact de la concentration de porteurs libres sur l'émission inter-couche pourrait représenter une étape possible vers le contrôle du taux de transfert de charge dans les hétérostructures de van der Waals. Si un environnement électrostatique plus stable est souhaité, le dopage suivant l'éclairage laser peut être évité en encapsulant l'hétérostructure de van der Waals dans hBN [Courtade 2018].

Excitons de moiré dans $MoSe_2$

Les données typiques obtenues sur l'hétérostructure MoS_2 / $MoSe_2$ avec un angle d'empilement nominal nul sont présentées sur la figure 6(a) où nous montrons une image au microscope optique de l'hétérostructure fabriquée. Il se compose d'un flocon de $MoSe_2$ monocouche, indiqué par la ligne pointillée bleue, partiellement recouvert par une monocouche MoS_2 (lignes pointillées blanches). Un spectre photoluminescence représentatif de notre hétérostructure prise sur une large gamme d'énergie à $T = 5\,\mathrm{K}$ est présenté sur la figure 6(b). Les pics à 1,615 eV et 1,644 eV proviennent de la recombinaison radiative du trion intra-couche et de l'exciton de $MoSe_2$, respectivement. Les pics photoluminescence plus faibles centrés à 1,94 eV et 1,87 eV sont affectés à la recombinaison des excitons neutres et aux complexes excitoniques liés à des défauts dans MoS_2 [Surrente 2017, Cadiz 2017], respectivement. Le pic de faible énergie à 1,37 eV provient de l'émission d'exciton inter-couche, qui provient du transfert de charge dû à l'alignement de bande de type II, comme illustré schématiquement dans l'encart de la figure 6(b) [Baranowski 2017b, Surrente 2018].

Ici, nous nous concentrons sur les propriétés des excitons intra-couche. Les cartes d'intensité photoluminescence de MoS_2 et $MoSe_2$ intra-couche sont présentées sur la figure 6(c-d). L'intensité $MoSe_2$ photoluminescence de la figure 6(d) est supprimée dans la région de l'hétérostructure, en raison du transfert de charge inter-couche [Ceballos 2014, Chen 2016]. Les propriétés optiques fortement modifiées dans la région de l'hétérostructure sont une indication du bon couplage entre les couches, caractéristique pour un angle d'empilement d'environ 0 degré [Wang 2016b].

Nous nous concentrons sur les spectres d'émission et de réflectivité dans la gamme d'énergie correspondant aux excitons intra-couche dans $MoSe_2$. Sur une monocouche de $MoSe_2$ entièrement encapsulée par hBN, le spectre photoluminescence se compose de deux pics, attribués à l'exciton chargé et neutre (voir la figure 7(a)). En revanche, l'exciton $MoSe_2$ et le trion photoluminescence de la ré-

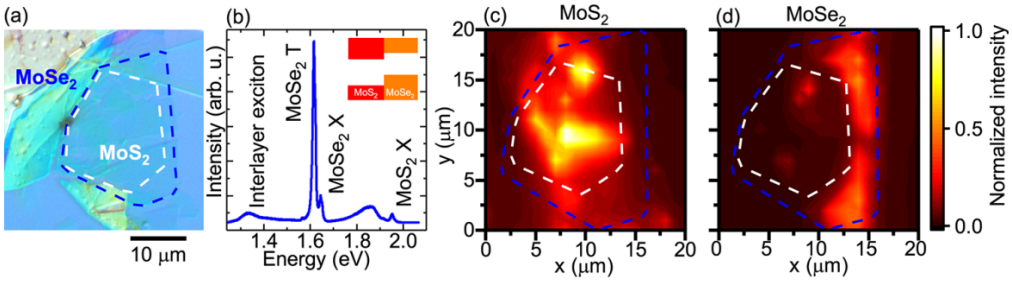

Figure 6: (a) Image au microscope optique de l'hétérostructure MoS_2 / $MoSe_2$ encapsulée dans hBN. Les lignes pointillées bleues et blanches indiquent les contours des flocons $MoSe_2$ et MoS_2. (b) Spectre photoluminescence de l'hétérostructure pris à T = 5 K. L'encart montre l'alignement de bande schématique d'une hétérostructure $MoSe_2$ / MoS_2. Cartes d'intensité photoluminescence normalisées de (c) MoS_2 et (d) $MoSe_2$.

gion d'hétérostructure révèlent une structure à double pic, comme le montre la figure 7(b). Nous étiquetons ces caractéristiques XL (TL) et XH (TH), pour désigner la transition énergétique supérieure et inférieure de l'exciton (trion). De manière importante, le clivage de l'émission d'exciton est également visible dans le spectre de réflectivité de la figure 7(b), démontrant sans équivoque qu'elle est liée à une transition d'exciton libre plutôt qu'à une émission à l'état lié.

La présence d'un double pic photoluminescence dans la région de l'hétérostructure est cohérente avec l'effet attendu du motif moiré sur les complexes excitoniques intra-couches. Selon les prédictions théoriques, l'empilement de deux monocouches TMDC mésappariées induit une fluctuation spatialement périodique du potentiel ressenti par les excitons [Yu 2017, Zhang 2017, Wu 2018, Wu 2017a] avec deux minima locaux liés à différents registres atomiques [Yu 2017]. La période du motif moiré est de l'ordre de quelques dizaines de nanomètres. Par conséquent, la résolution spatiale de nos mesures optiques en champ lointain est insuffisante pour résoudre la variation spatiale de l'énergie d'émission des excitons situés dans différents minima de potentiel. Néanmoins, l'émission de différents minima optiquement actifs du motif de moiré peut être résolue spectralement dans notre échantillon de haute qualité. La double structure des pics d'exciton et de trion est constamment observée dans la région d'hétérostructure, alors qu'elle est complètement absente dans les régions monocouches. Ceci est résumé sur la figure 7(c), où la carte spatiale met en évidence les zones où le clivage est observée. Pour vérifier que le découpage observé est une conséquence directe du motif moiré, nous avons effectué les mêmes mesures sur l'hétérostructure MoS_2 / $MoSe_2$ avec un angle d'empilement de *simeq*20 degrés. Dans cette hétérostructure, la période du motif moiré est significativement plus petite que l'extension spatiale de la fonction d'onde d'exciton intra-couche et, comme prévu, nous n'observons pas de clivage dans les spectres photoluminescence de l'exciton ou trion $MoSe_2$.

Sur la figure 7(d), nous montrons la variation spatiale de l'énergie de l'exciton et

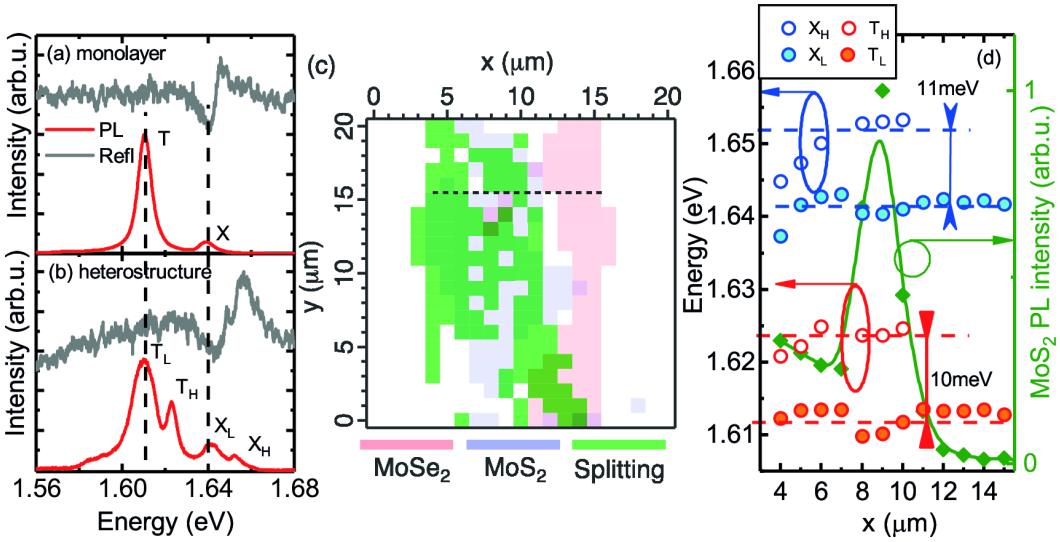

Figure 7: Figure 7. Spectres photoluminescence et de réflectivité de $MoSe_2$ mesurés dans les régions (a) monocouche et (b) d'hétérostructure. (c) Carte spatiale montrant la présence d'un clivage de l'émission de $MoSe_2$, superposée aux zones de photoluminescence les plus intenses de MoS_2 et $MoSe_2$. (d) Énergie des transitions $MoSe_2$ observées (points bleus et rouges) extraite le long de la ligne pointillée horizontale du panneau (c). Les cercles ouverts correspondent aux pics de haute énergie observés uniquement dans l'hétérostructure, les cercles fermés représentent les transitions de basse énergie observées dans toutes les régions du flocon de $MoSe_2$. Les diamants verts indiquent l'intensité du MoS_2 photoluminescence.

du trion photoluminescence le long de la ligne pointillée traversant l'hétérostructure de la figure 7(c). La tranche commence et se termine aux positions sur l'échantillon où photoluminescence est observé. Une comparaison directe du spectre mesuré dans la région de l'hétérostructure avec celui mesuré à l'extérieur (voir figure 7(a-b)) révèle que la double structure résulte de l'apparition d'un nouveau pic d'émision du côté haute énergie de l'exciton principal et émission de trion. Les énergies des raies d'émission observées dans les monocouches isolées sont presque identiques aux raies XL et TL observées dans l'hétérostructure, comme le soulignent les lignes verticales sur la figure 7(a-b). Ceci est en accord avec la prédiction selon laquelle les états d'excitons liés au modèle de moiré devraient apparaître comme des pics du côté haute énergie des principaux pics photoluminescence [Yu 2017, Wu 2017a]. Cette observation, associée au fait que la structure à double pic apparaît sur une vaste zone de l'hétérostructure et pas seulement à ses bords [Raja 2017], permet d'écarter la variation du écrantage diélectrique liée à la présence de la monocouche MoS_2 comme origine de la structure de doublet observée. Le constant diélectrique de MoS_2 étant supérieure à celle de hBN [Laturia 2018], un effet de blindage diélectrique conduirait à l'apparition de pics d'énergie plus faibles lorsque l'excitation est effectuée sur la région de l'hétérostructure [Raja 2017].

Conclusions

En conclusion, nous avons démontré l'impact du motif de moiré formé dans une hétérostructure $MoS_2/MoSe_2$ sur les spectres optiques des espèces d'excitons intra-couche. Les fluctuations de potentiel résultant de registres atomiques localement différents, provoquent le clivage des transitions trion et exciton de $MoSe_2$ et MoS_2 en deux pics liés aux minima locaux optiquement actifs du potentiel moiré. La nature des doublets observés a été confirmée par une cartographie spatiale détaillée du photoluminescence et par sa dépendance à la température. Les mesures résolues par polarisation révèlent que les règles de sélection des transitions ne changent pas par rapport au cas des monocouches isolées. La dynamique photoluminescence montre que le potentiel induit par le moiré ne change pas de manière significative la force de l'oscillateur des transitions. Cependant, le potentiel de moiré peut être responsable de la suppression du transfert inter-couche des excitons thermalisés. Tous les résultats présentés sont en accord avec l'influence théoriquement prédite du motif de moiré sur les excitons intra-couche dans les dichalcogénures de métaux de transition.

Excitons $MoSe_2$ neutres et chargés dans un champ magnétique

Nous avons effectué des mesures des excitons neutres et chargés dans les monocouches $MoSe_2$ et des excitons intra-couche moiré dans $MoS_2/MoSe_2$ en champ magnétique élevé dans le "High Field Magnet Laboratory" (HFML) à Nimègue.

Nous avons travaillé avec deux échantillons: un film $MoSe_2$ monocouche CVD pris en sandwich entre deux films monocouche MoS_2 CVD et une hétérocouche $MoS_2/MoSe_2$ hautement alignée fabriquée par exfoliation mécanique [Castellanos-Gomez 2014a] et entièrement encapsulée dans hBN. Surtout, sur le dernier échantillon, une partie du flocon de $MoSe_2$ ne chevauche pas la monocouche de MoS_2, nous avons donc pu examiner les propriétés du $MoSe_2$ pur. Sur la zone d'hétérostructure de cet échantillon, la présence de deux monocouches hautement alignées avec un treillis proportionné conduit à la formation d'un motif moiré. Cette partie de l'échantillon affiche un photoluminescence et des spectres d'absorption significativement différents [Zhang 2017], et est appelée moiré dans la suite.

Nous présentons les spectres magnéto-photoluminescence des trois échantillons étudiés mesurés jusqu'à 9 T sur la figure 8. Les spectres de la tricouche et des échantillons monocouches, représentés sur la figure 8(a-b), consistent en deux raies d'émission. Le pic d'énergie le plus faible et le plus élevé est attribué à la recombinaison de l'exciton neutre. Le pic le plus fort, décalé vers le rouge d'environ 30 meV par rapport à l'exciton neutre, provient de la recombinaison du trion, en accord avec les rapports précédents [Ross 2013]. L'exciton et le trion ont des formes de lignes gaussiennes, avec une largeur totale à mi-hauteur (FWHM) d'environ 10 meV. L'encapsulation de $MoSe_2$ exfolié mécaniquement dans hBN conduit à un changement de la forme de la ligne en Lorentzienne et à une réduction de la largeur de la ligne à moins de 5 meV, comme visible sur la figure 8(b). Cet élargissement ré-

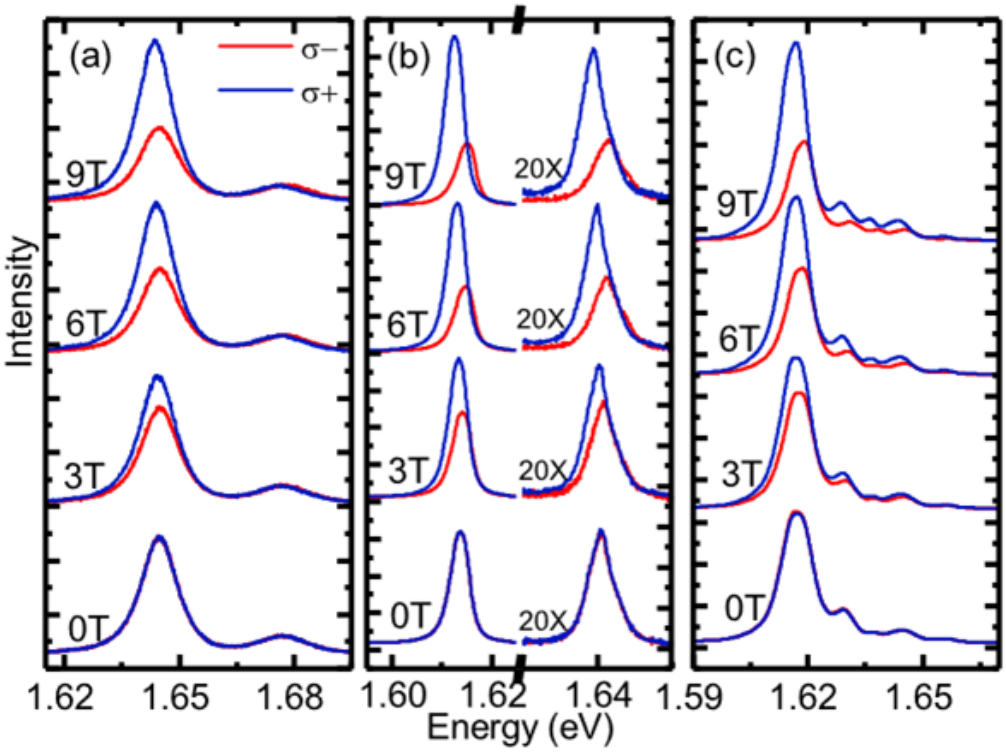

Figure 8: Spectres Magneto-photoluminescence jusqu'à 9T de (a) trois couches, (b) une monocouche encapsulée au hBN et (c) un échantillon de moiré. Le pic de haute énergie (exciton) dans le panneau (b) a été renormalisé pour plus de clarté. Les lignes bleues et rouges indiquent les signaux photoluminescence en polarisations circulaires $\sigma+$ et $\sigma-$ respectivement. Le faisceau d'excitation est polarisé circulairement en (a) et linéairement polarisé en (b) et (c).

duit indique une diffusion des excitons plus faible sur les défauts et atteste de leur densité plus faible dans l'échantillon monocouche. La figure 8(c) montre le spectre magnéto-photoluminescence des excitons de moiré intra-couche hébergés dans un $MoSe_2$ encapsulé dans hBN qui chevauche une monocouche de MoS_2. La présence d'un motif moiré induit un clivage des transitions excitoniques comme décrit en détail dans le chapitre précédent. Le clivage est bien illustrée par les multiples résonances excitoniques visibles dans le spectre photoluminescence de la figure 8(c).

Pour les trois échantillons, à champ magnétique nul, l'intensité photoluminescence résolue dans les deux polarisations circulaires est la même, ce qui donne un DCP négligeable. Cela résulte de l'utilisation d'un faisceau d'excitation polarisé linéairement dans le cas de la figure 8(b), qui injecte des excitons dans les vallées $K+$ et $K-$. Les spectres représentés sur la figure 8 (a) ont été excités avec un laser à polarisation circulaire. Cependant, l'excitation sélective de la vallée dans ce cas est neutralisée par la diffusion inter-vallée très efficace dans $MoSe_2$, en raison d'un

excès d'énergie important des excitons photo-créés [Baranowski 2017a, Tornatzky 2018]. Cela égalise effectivement les populations d'excitons dans les deux vallées de la même manière qu'une excitation polarisée linéairement le ferait.

L'application d'un champ magnétique entraîne deux effets qui peuvent être notés sur la figure 8, à savoir un clivage des pics photoluminescence et un changement des intensités relatives des deux composantes de polarisation circulaire du photoluminescence. Comme le montre la figure 9, le clivage observée expérimentalement est linéaire pour toutes les espèces excitoniques étudiées, ce qui nous a permis d'évaluer les facteurs g. En effet, comme on le voit sur la figure 9, la séparation observée des raies photoluminescence d'excitons neutres correspond à des facteurs g compris entre -3,8 et -4,4, en accord avec une multitude de rapports antérieurs [Li 2014a, MacNeill 2015, Srivastava 2015b, Aivazian 2015a, Wang 2015a, Plechinger 2016a, Stier 2016a, Mitioglu 2016, Koperski 2018, Zipfel 2018, Li 2019, Arora 2016, Mitioglu 2018]. Les petits écarts du facteur g observé expérimentalement par rapport à la valeur de -4 sont généralement attribués à la contribution du moment magnétique intercellulaire [Mitioglu 2016] et à une contribution des orbitales p aux états de bord de bande [Liu 2015].

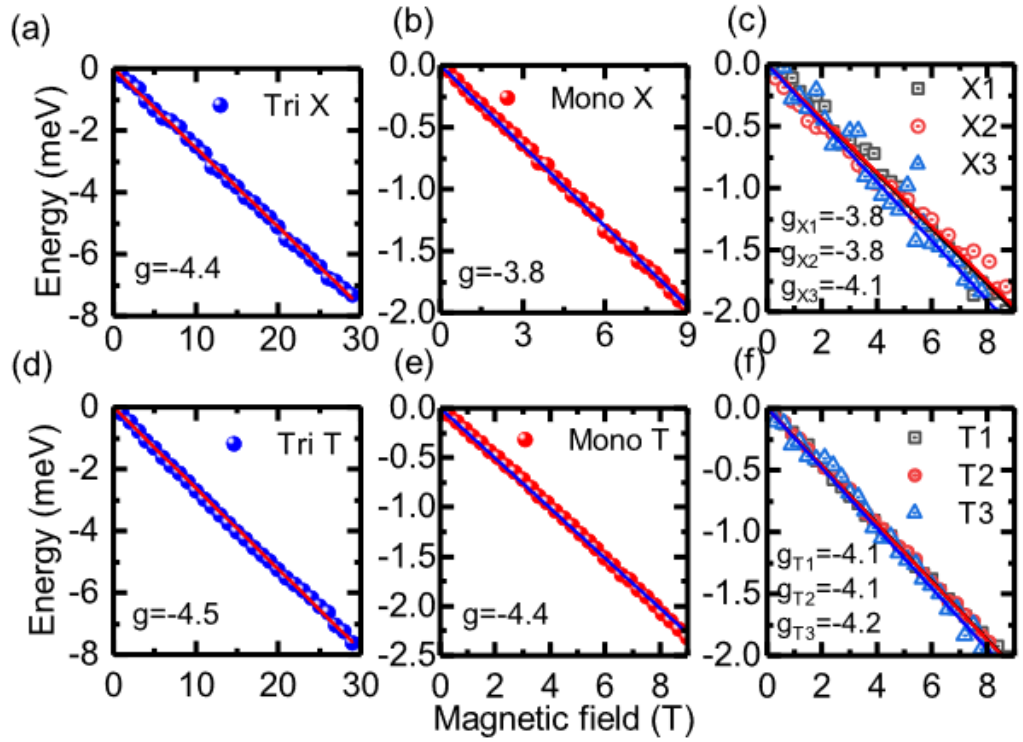

Figure 9: Clivage de Zeeman de l'exciton neutre et chargé mesuré sur les échantillons à trois couches (a, d, respectivement), monocouche (b, e, respectivement) et moiré (c, f, respectivement).

Nous rapportons pour la première fois sur la figure 9(c) le clivage induite par le

champ magnétique des excitons intra-couches de moiré. Leur facteur g est le même dans l'erreur expérimentale que celui de l'exciton neutre mesuré sur des zones monocouches du même échantillon. Cette observation peut être comprise sur la base du fait que les états de points K dans l'hétérobilayer TMDC sont connus pour ne pas s'hybrider, conservant ainsi leur caractère monocouche d'origine [Gao 2017, Hanbicki 2018]. De plus, le motif moiré induit une modulation spatiale de la bande interdite [Wu 2017b], qui n'introduit pas de variation dans la nature des états de bord de bande. On s'attend à ce que les éléments de la matrice de moment angulaire orbital des excitons de moiré intra-couche soient les mêmes que ceux des excitons libres dans des monocouches isolées. Par conséquent, l'écart du facteur g des excitons de moiré par rapport à celui des excitons neutres devrait être négligeable, comme cela a été observé expérimentalement. Quant à l'exciton chargé, la charge négative capturée fournit un moment magnétique supplémentaire au complexe, qui contribue de la même manière à l'énergie initiale et finale de l'exciton chargé. Ainsi, le facteur g de l'exciton chargé est approximativement le même que celui de l'exciton neutre, comme le montre la figure 9(c, d) [Li 2014a, MacNeill 2015, Srivastava 2015b, Aivazian 2015a, Wang 2015a, Li 2019].

Conclusions

Nous avons effectué des mesures des excitons neutres et chargés dans les monocouches de $MoSe_2$ et des excitons intra-couche de moiré dans MoS_2 / $MoSe_2$ dans un champ magnétique élevé. Le comportement des excitons moirés dans un champ magnétique est essentiellement le même que celui des excitons normaux. Notamment, les facteurs $g \simeq -4$ sont identiques dans les limites de l'erreur expérimentale. En utilisant un champ magnétique élevé, il est possible de contrôler le degré de polarisation de vallée. La différence dans l'amélioration de la polarisation de la vallée par champ magnétique fait l'objet d'études et de modélisations complémentaires.

Conclusion générale

Nous avons utilisé la spectroscopie optique, en particulier la photoluminescence, la réflectivité, la diffusion Raman et la photoluminescence résolue en temps pour étudier les hétérostructures TMDC. Des expériences magnéto-optiques ont été réalisées dans l'installation à champ élevé EMFL à Nimègue.

Nous avons observé un effet photo-génération persistant sur l'émission d'excitons dans une hétérostructure MoS_2 / $MoSe_2$ / MoS_2. L'intensité de l'émission d'exciton photoluminescence inter-couche est diminuée sous illumination laser. Le changement simultané de l'émission d'exciton neutre et chargé indique l'augmentation du niveau de photo-génération. L'intensité accrue de l'émission d'exciton intra-couche et l'intensité diminuée de l'exciton inter-couche suggèrent que la photo-génération réduit l'efficacité de transfert de charge inter-couche. Ce phénomène persiste à basse température et sous vide à moins que l'échantillon ne soit exposé à l'air, ce qui indique que cette photo-génération est liée aux molécules d'eau et d'oxygène

physiquement absorbées en surface. Les résultats fournissent une méthode concise pour moduler l'efficacité du transfert de charge entre les couches.

Nous avons étudié les hétérostructures $MoSe_2/MoS_2$ avec différents angles de torsion. L'angle de torsion a été prédéterminé pendant la procédure d'empilement et confirmé par la suite en utilisant des mesures résolues par polarisation de la deuxième génération d'harmoniques. Nous avons observé que pour les hétérostructures avec un angle de torsion presque nul, l'émission et l'absorption excitoniques du $MoSe_2$ s'accompagnent de pics latéraux du côté haute énergie du spectre. Il s'agit de la première observation expérimentale d'excitons intra-couche de moiré dans un TMDC atomiquement mince. La dynamique photoluminescence montre que le potentiel induit par le moiré ne change pas de manière significative la force de l'oscillateur des transitions. Cependant, le potentiel de moiré peut être responsable de la suppression du transfert inter-couche des excitons thermalisés. Tous les résultats présentés sont en accord avec l'influence théoriquement prédite du motif de moiré sur les excitons intra-couche dans les dichalcogénures de métaux de transition.

Enfin, nous avons étudié les propriétés optiques des excitons et des excitons chargés en champ magnétique élevé. Nous comparons les propriétés magnéto-optiques des excitons dans des monocouches isolées de MoS_2 et $MoSe_2$ avec les excitons intra-couche de moiré dans MoS_2 / $MoSe_2$. Le comportement des excitons moirés dans un champ magnétique est essentiellement le même que celui des excitons normaux. Notamment, les facteurs $g \simeq -4$ sont identiques dans les limites de l'erreur expérimentale. Nous comparons également la polarisation de vallée pour les excitons dans la monocouche $MoSe_2$ cultivée par CVD et dans la monocouche exfoliée $MoSe_2$ de haute qualité encapsulée dans du BN hexagonal. En utilisant l'optique résolue par polarisation pour mesurer le degré de polarisation circulaire (DCP) de l'émission photoluminescence, nous avons démontré qu'un champ magnétique élevé peut être utilisé pour contrôler le degré de polarisation de vallée. La différence dans l'amélioration de la polarisation de la vallée par champ magnétique fait l'objet d'études et de modélisations complémentaires.

Contents

1 Introduction **1**
- 1.1 Layered materials . . . 2
- 1.2 Semiconducting transition metal diachalcogenides . . . 3
- 1.3 Exciton in 2D transition metal diachalcogenides . . . 6
  - 1.3.1 Excitons in bulk semiconductors; hydrogen-like model . . . 6
  - 1.3.2 Excitons in 2D transition metal dichalcogenides; role of the dielectric screening . . . 8
  - 1.3.3 Excitons in 2D transition metal diachalcogenides; the role of SOC . . . 11
  - 1.3.4 Charged excitons in 2D transition metal dichalcogenides . . . 12
- 1.4 Van der Waals (vdW) heterostructure . . . 15

2 Experimental techniques and sample characterization **19**
- 2.1 Optical spectroscopy . . . 19
  - 2.1.1 Steady-state micro- spectroscopy . . . 21
  - 2.1.2 Time-resolved Photoluminescence . . . 21
  - 2.1.3 Polarization optics . . . 22
- 2.2 Micro-PL in dc magnetic field . . . 23
- 2.3 Sample characterization . . . 24
  - 2.3.1 Chemical vapor deposition grown monolayer and van der Waals heterostructures . . . 24
  - 2.3.2 Exfoliated monolayer and hexagonal boron nitride encapsulation . . . 26

3 Photodoping effect in $MoSe_2/MoS_2$ heterostructure **29**
- 3.1 Introduction . . . 29
- 3.2 Micro-PL properties of $MoSe_2/MoS_2/MoSe_2$ heterostructure . . . 30
- 3.3 Photodoping on intra-layer exciton of $MoSe_2$ . . . 30
- 3.4 Photodoping on interlayer exciton . . . 32
- 3.5 Photodoping microscopic mechanism . . . 34
- 3.6 Conclusion . . . 36

4 Moiré excitons **37**
- 4.1 Introduction: intra- and inter-layer moiré excitons . . . 37
- 4.2 Determination of the stacking angle in MoS_2/MoS_2 heterostructures 40
- 4.3 Fingerprints of intra-layer moiré Excitons . . . 44
  - 4.3.1 Moiré Excitons in $MoSe_2$ . . . 44
  - 4.3.2 Moiré Excitons in MoS_2 . . . 47
- 4.4 Properties of moiré excitons . . . 47
  - 4.4.1 Temperature dependence of the moiré exciton PL . . . 48

4.4.2 PL dynamics of moiré excitons 49
4.4.3 Valley polarization of moiré excitons 51
4.5 Conclusions 52

5 Magneto optics of the $MoS_2/MoSe_2$ heterostructures 53
5.1 Magneto optics of TMDC 53
5.2 $MoSe_2$ neutral and charged excitons in magnetic field 55
5.3 Valley polarization of the neutral and charged excitons in magnetic field 58
5.4 Conclusions 59

6 Conclusions 61

A Publications 63

Bibliography 65

Chapter 1

Introduction

Contents

1.1 Layered materials 2
1.2 Semiconducting transition metal diachalcogenides 3
1.3 Exciton in 2D transition metal diachalcogenides 6
1.3.1 Excitons in bulk semiconductors; hydrogen-like model 6
1.3.2 Excitons in 2D transition metal dichalcogenides; role of the dielectric screening 8
1.3.3 Excitons in 2D transition metal diachalcogenides; the role of SOC 11
1.3.4 Charged excitons in 2D transition metal dichalcogenides 12
1.4 Van der Waals (vdW) heterostructure 15

Today, mankind depends on "tools" to process and store information such as computers, smartphones and many other electronic devices. All those devices use semiconductor components such as transistors, diodes, lasers for their operation. Therefore, semiconductor technologies are one of the pillars of modern civilization development.

Nowadays electronics is dominated by silicon, III-V and II-VI technology, which are approaching their performance limits related to the fundamental properties of these materials. Because of that scientists are still making efforts to further develop the technology of semiconductor. In particular, they are looking for new semiconductor materials which properties will let as process with in a more efficient way. One of the most intensively explored direction is related to van der Waals crystals, materials which are kind of "natural" quantum wells of the thickens of singles atoms. Therefore they represent ultimate limit of quantization in one direction.
Transition metal dichalcogenides belongs to the group of two dimensional materials which are the subject of particular interest due to unique band structure that provide unique potential to encode eight bits of information, (instead of two) by single charge carrier. This is thanks to extra degree of freedom given by the spin and valley index which can be relatively easy controlled in this materials in their monolayer form. All of this This will hopefully allow to to process more information in less time and energy consumption. The use of additional electron degrees of freedom can help to development electronics beyond the limits set by Moore's law.
This chapter provides a brief overview of the optical and electronic properties

of layered semiconducting, focusing especially on transition metal dichalcogenides (TMDCs) and van der Waals heterostructures and features which makes them so unique.

1.1 Layered materials

The discovery of graphene by Andre Geim and Konstantin Novoselov in 2004 [Novoselov 2004] opened the new research field of atomically thin two dimensional materials. These materials with single or a few atoms thickness can be easily obtained by micromechanical exfoliation of bulk crystals. They are characterized by strong in-plane covalent bonds and weak van der Waals interactions between the layers. The family of van der Waals layered materials turned out to be very rich, including monoelemental materials such as graphene, phosphorene, silicene, germanene, stanene, borophene, antimonene or black arsenic [Pumera 2017, Chen 2018c], binary compounds such as boron nitride, metal oxide and transition metal mono-(SnS, SnSe, GeS, GeSe) [Gomes 2015], di-(MoS2, MoSe2, WSe2 WS2) and trichalcogenides (TiS3, ZrS3, HfS3, NiS3) [Silva-Guillén 2017, Island 2017]. Group IV-V compounds such as GeP or SiP[Li 2018] as well as certain hybrid perovskites [Lédée 2017] can also be found in thin layered form. Layered compounds include metals, semimetals, insulators and semiconductors and their characteristics are modified depending on the number of layers[Duong 2017]. It turns out that due to interlayer coupling and quantum confinement effects the size and nature of the band gap can be easily tuned by changing the number of layers. For example, while the band gap of a black phosporus remains direct, it changes from mid infrared for the bulk crystal [Keyes 1953, Asahina 1983, Island 2017] to the visible range for a few layers [Tran 2014, Castellanos-Gomez 2014b, Liu 2014]. The band gap of semiconducting transition metal dichalcogenides has an indirect gap in the near infrared spectral range in bulk, while a single layer transition metal dichalcogenides exhibits *a direct gap in the visible spectral range*[Mak 2010, Splendiani 2010, Wang 2012, Gutiérrez 2013, Eda 2011]. Moreover, due to their flexibility, the band gap of layered materials can by tuned by external strain over much larger range than for classic semiconductors [Roldán 2015]. Such a variety of layered materials combined with wide tunability makes these materials very attractive for opto-electronic applications, including light emitting devices, photo detectors, solar cells[Butler 2013, Huo 2017, Das 2019], transistors[Kelly 2017, Radisavljevic 2011] and energy storage[Zhu 2018]. Another advantage of layered semiconductors is possibility to stack them in any desired combination with other layered semiconductors without limitations related to lattice mismatch characteristic of covalent crystals. Therefore, the vertical stacking of monolayer solids provides a rich playground that can be used to tailor properties, giving rise to new and attractive features [Geim 2013, Novoselov 2016].

1.2 Semiconducting transition metal diachalcogenides

Semiconducting transition metal diachalcogenides (TMDCs) are a representative family of atomically thin materials. They are characterized by the general formula MX_2, where M denotes a transition metal atom from group VI, and X correspond to a chalcogen atom (M=Mo, W; X=S, Se). The crystal structure of monolayer and bulk TMDC and possible stacking sequences corresponding to different polymorphs is schematically presented in Fig. 1.1. A monolayer of MX_2 has the arrangement X-M-X. The metal atom is located in the center of the trigonal prismatic unit cell being bound to six chalcogen atoms via strong covalent bonds. The monolayers are stacked together via weak van der Waals forces. The inversion symmetry is broken for monolayer, but is restored in bulk[Zeng 2015]. Bulk TMDCs exist in three different polymorphs, namely 1T, 2H or 3R where the letters correspond to trigonal, hexagonal and rhombohedral with the number indicating the number of layers in the unit cell. Monolayers exist only in 1T or 2H forms. The 2H polymorth exhibits a trigonal prismatic geometry with symmetry corresponding to D3h group while the 1T form adopts an octahedral or trigonal antiprismatic geometry with corresponding D3d group. The 1T form exhibits metallic behaviour, while both 2H and 3R forms shows semiconducting behaviour[Kuc 2015, Toh 2017]. The 1T phase is metastable and easily converted to the stable 2H, however, it can be stabilized by intercalation with ions such as H, Li, Na and K [Acerce 2015]. In the rest of the thesis I will be considering only the 2H form of TMDCs.

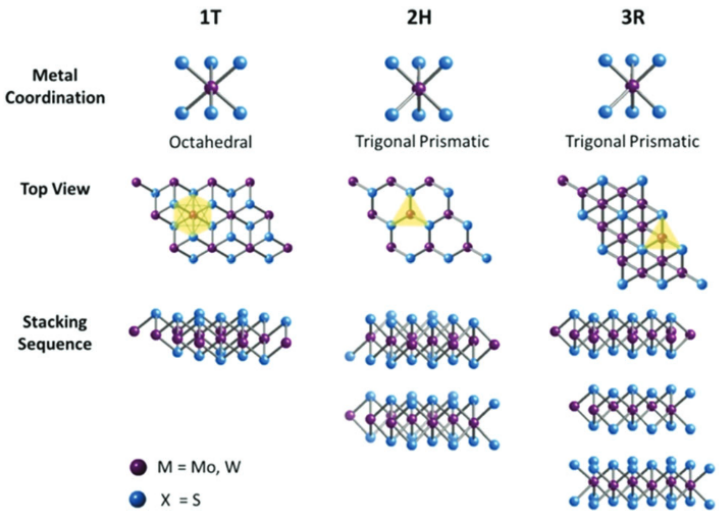

Figure 1.1: Metal coordinations and stacking sequences of TMDC unit cells for all three 1T, 2H and 3R polymorphs after [Toh 2017]

First-principles band structure calculations for bulk and a few layer MoS_2 show that the minimum of the conduction band (CBM) is located at a point between the K and Γ points in the Brillouin zone, and the maximum of the valence band

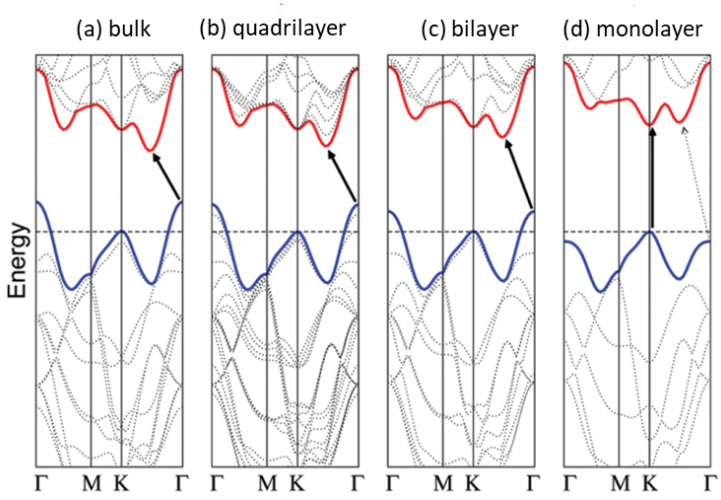

Figure 1.2: Calculated band structures of (a) bulk, (b) quadrilayer, (c) bilayer and (d) monolayer MoS_2. [Splendiani 2010]

(VBM) is located at the Γ point [Kobayashi 1995]. Thus, bulk and multilayer TMDC have an indirect band gap, as shown in Fig. 1.2(a-c). In the case of a monolyaer, the band gap is direct and located at the K points corresponding to the corners of the hexagonal Brillouin zone, as shown in Fig. 1.2(d)[Splendiani 2010]. In addition, density functional theory (DFT) calculations reveal that the direct band gap at the K point of the Brillouin zone barely changes as a function of the number of layers, whereas, the indirect band gap increases monotonically as the number of layers decreases, as shown in Fig. 1.2. The direct nature of the band gap in monolayers was first suggested to explain the observed emergence of strong photoluminescence emission in monolayer MoS_2[Mak 2010, Splendiani 2010]. The crossover from an indirect band gap semiconductor to a direct gap material with decreasing the number of layers (N) was further demonstrated experimentally [Mak 2010]. The preliminary results obtained for MoS_2 have been very quickly generalized to other members of the TMDCs family, such as $MoSe_2$, WS_2 or WSe_2 [Zhao 2013, Tonndorf 2013].

A tight binding model, which correctly describes low energy physics of TMDCs reveals that the Bloch states near the band edge for the valence and conduction bands mainly originate from the metal orbitals d_{Z^2}, d_{xy} and $d_{x^2-y^2}$, as shown in Fig. 1.3 (a)[Liu 2013a]. The contribution of the s and p orbitals is negligible. d orbitals are a source of strong spin-orbit coupling. The conduction band, which in a first approximation is composed mainly from d_{Z^2} orbitals, remains almost spin degenerate, while the SOC splitting in the valence band is much larger. Band structure calculations which includes spin orbit coupling for the TMDCs are presented in Fig. 1.3 (b)[Liu 2013a, Ramasubramaniam 2012]. The values of the splitting in the valence band are summarized in the table in Fig. 1.3. Typical values for the spin splitting in the valence band are of the order of a few hundred meV, being almost

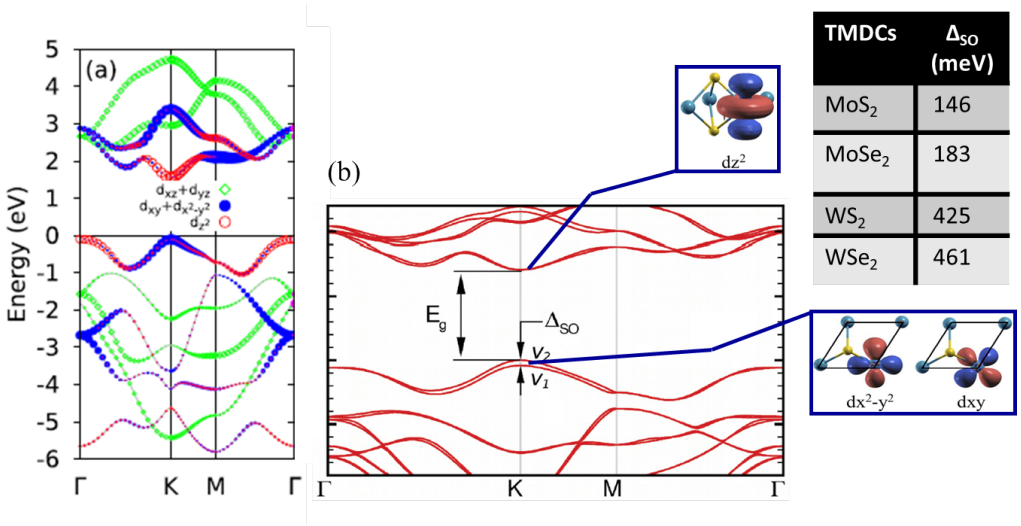

TMDCs	Δ_{SO} (meV)
MoS_2	146
$MoSe_2$	183
WS_2	425
WSe_2	461

Figure 1.3: (a) Orbital projected band structures for monolayer MoS_2. Contributions from Mo d-orbitals: blue dots for d_{xy} and $d_{x^2-y^2}$, red open circles for d_{Z^2}, and green open diamonds for d_{xz} and d_{yz}. The size of the symbols reflects the orbital population in the corresponding state. After[Liu 2013a] (b) Typical band structure for TMDCs with spin-orbit coupling (SOC) taken into account in the DFT calculations, after [Ramasubramaniam 2012]. The values of the SOC induced splitting in the valence band are summarized in the table.

twice larger for tungsten based TMDCs [Liu 2013a, Ramasubramaniam 2012].

Another particularity of monolayer TMDCs is the broken inversion symmetry; the two valleys are not equivalent at K and -K points of the 2D hexagonal Brillouin zone, as shown in Figure. 1.4 (a). The broken inversion symmetry combined with strong SOC and time-reversal correlates the valley index with the spin index, a property which is commonly referred to as spin-valley locking [Xiao 2012]. The spin-valley locking leads to valley dependent optical selection rules, which are presented in Fig. 1.4(b). The interband transitions at the K (-K) points are coupled with photons with optical helicity σ^+ (σ^-). This provides the possibility to manipulate the carrier spin in a certain valley using circularly polarized light. Thus, atomically thin TMDCs provide a platform for valleytronics and spintronics [Xiao 2012]. It is possible to optically pump the valley polarization. Indeed, the first experimental results have been demonstrated for MoS_2 by Mak and co-authors[Mak 2012] and Kioseoglu and co-workers [Kioseoglou 2012], as presented in Fig 1.4 (c). However, as presented in Fig 1.4 (c), the effectiveness of pumping the valley polarization strongly depends on the excitation wavelength and other parameters, such as the choice of the monolayer material.

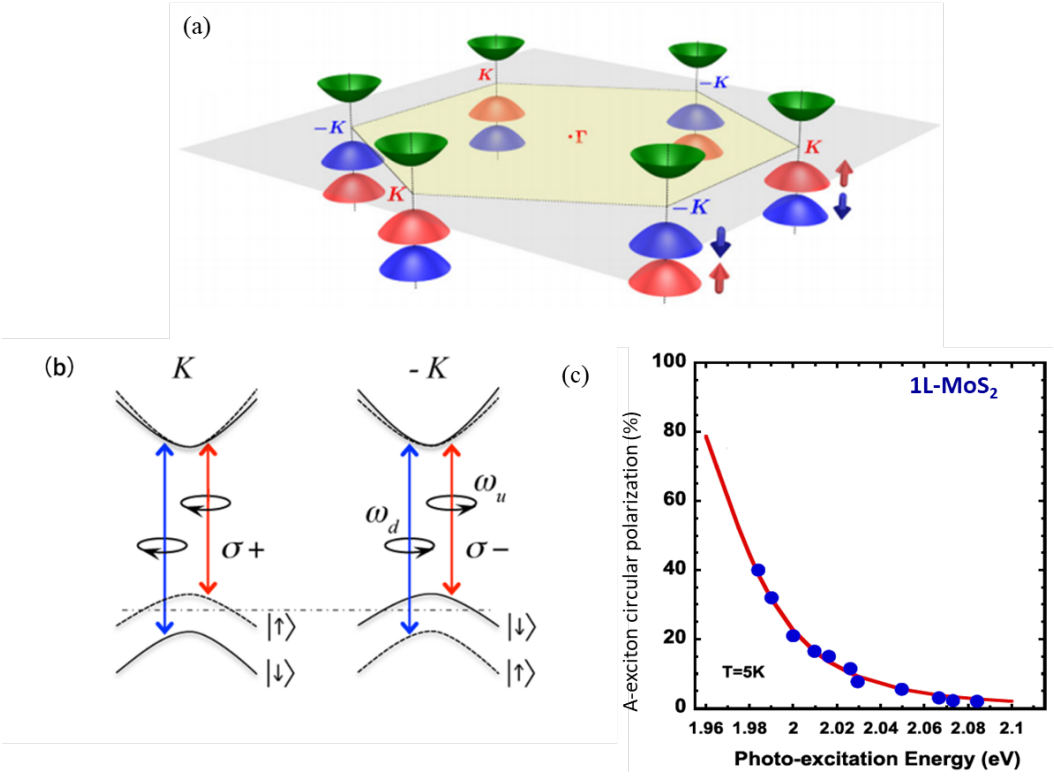

Figure 1.4: (a) Schematic showing the band structure at the band edges located at the K points. (b) Valley and spin optical transition selection rules. Solid (dashed) curves denote bands with spin-down (-up) quantized along the out-of-plane direction. The splitting in the conduction band is exaggerated. ω_u and ω_d are, respectively, the transition frequencies from the two split valence-band tops to the conduction band bottom[Xiao 2012]. (c) A-exciton valley polarization for MoS_2 measured as a function of the excitation wavelength, after [Mak 2012, Kioseoglou 2012]

1.3 Exciton in 2D transition metal diachalcogenides

In this part we describe the general excitonic properties of semiconductors, which is then followed by a more detailed description of excitons and charged excitons in monolayer TMDCs.

1.3.1 Excitons in bulk semiconductors; hydrogen-like model

In semiconductors, the absorption of a photon with energy equal to or higher than the band gap leads to the excitation of an electron from the valence band to the conduction band, leaving behind a hole in the valence band. The negatively charged electron in the conduction band is bound to the positive charged hole via the attractive Coulomb potential [Pelant 2012]

$$U(r) = -\frac{e^2}{4\pi\epsilon_0\epsilon r}, \tag{1.1}$$

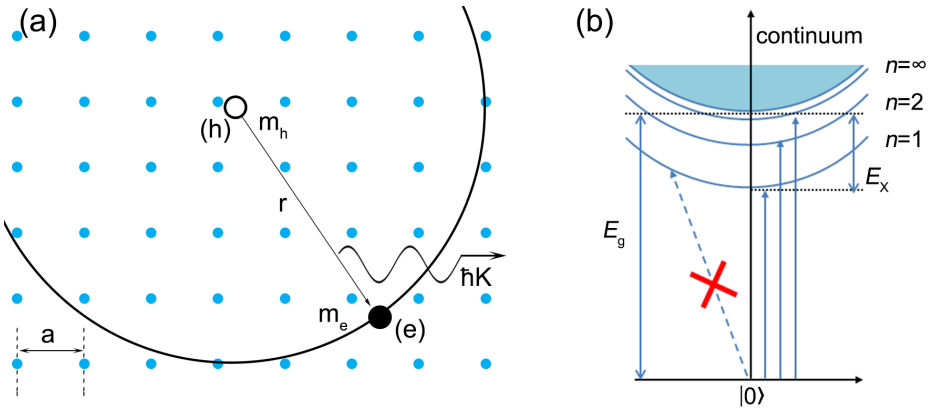

Figure 1.5: (a) Schematic showing a Wannier exciton in a crystal with lattice constant a. (b) The exciton dispersion relations $E = E(K)$ for the ground and excited excitonic states.[Pelant 2012]

where r is the electron-hole distance and ϵ is the dielectric constant of the material, e is the elementary charge, and ϵ_0 is the vacuum permittivity. The bound electron and hole form a quasi-particle commonly referred to as an exciton (X). Depending on the wave-function and binding energy, an exciton can be classified into two limiting cases; excitons with a strong electron-hole interaction which are tightly bound to a unit cell are named Frenkel excitons. However, in the most classic semiconductors the exciton are delocalized over many unit cells and are referred to as Wannier-Mott excitons. A Wannier exciton extends over many unit cells, *i.e.* the electron and hole are separated by many unit cells [Pelant 2012]. A schematic of a Wannier exciton is presented in Figure 1.5(a). In this case, the electrons and holes are weakly bound, and the exciton can move freely through the crystal. The effective masses of the electron (e) and hole (h) are denoted m_e and m_h, and $\hbar K$ is the quasi-momentum belonging to the translational movement of the exciton centre of mass. The exciton dispersion relations $E = E(K)$ is presented in Figure 1.5(b). The energy states of a weakly bound Wannier excitons in 3D materials are described by a hydrogen-like Bohr model,

$$E_n^{3D} = \frac{m_r/m_0}{\epsilon^2}\frac{1}{n^2}R_y = \frac{R_y^*}{n^2}, \tag{1.2}$$

Where, $n = 1, 2, 3...$ is the orbital quantum number, $R_y = -13.6\,\mathrm{eV}$ is the Rydberg constant, m_0 is the free electron mass, m_r is the exciton reduced mass related to the electron and hole effective masses by $\frac{1}{m_r} = \frac{1}{m_e} + \frac{1}{m_h}$ and ϵ is the dielectric constant. Excitonic states are expressed in the same way as for the hydrogen atom, where the Rydberg constant is replaced by an effective Rydberg constant $R_y^* = R_y m_r/m_0\epsilon^2$. With such a notation, R_y^* takes into account that the exciton is immersed in a real crystal with a dielectric constant different than the dielectric constant in vacuum, and that the masses of the carriers are renormalized compared to the free electron mass. In comparison to a hydrogen atom, the dielectric constant

ϵ reduces the attractive Coulomb force and the effective masses of the electron and hole forming excitons are much smaller than the free electron mass. This leads to a strong reduction of the effective Rydberg for excitons in semiconductors, with typical values of a few to a few tens of meV. The exciton binding energy (E_B) is the separation of lowest exciton state ($n = 1$) from the continuum ($n = \infty$) is equal to R_y^*. Typical binding energies in bulk semiconductors are for example 23 meV in GaN, 4.2 meV in GaAs, 12 meV in CdTe and 2 meV in GaSb[Fox 2001].

The radius of the electron-hole orbit is given by

$$r_n = \frac{\epsilon}{m_r/m_0} a_{B_n} = \frac{\epsilon}{m_r/m_0} n^2 a_B, \tag{1.3}$$

where a_B is the Bohr radius of the hydrogen atom corresponding to the ground state. Considering the low effective masses of the carriers and dielectric constant of the crystal, the excitons in bulk semiconductors are larger than in a hydrogen atom, for example 2.8 nm for GaN and 10 nm in CdTe [Fox 2001].

The absorption of the Wannier exciton is presented in in Figure. 1.5 (b). The absorption of the Wannier excition arise from the transition from the $|0>$ state to the $n = 1$ state or to higher energies excited states ($n = 2, 3...$). In the absorption, we typically observe a series of the excitonic lines at energies

$$h\upsilon = E_g - \frac{E_B}{n^2}. \tag{1.4}$$

Due to the relatively small exciton binding energy in bulk semiconductors (compared to the thermal energy $K_B T \simeq 25$ meV at $T = 300$ K) the observation of an exciton is usually possible only at very low temperatures.

1.3.2 Excitons in 2D transition metal dichalcogenides; role of the dielectric screening

In the systems with reduced dimensionality, the exciton binding energy increases due to the in-plane spatial confinement which gives rise to a stronger spatial overlap of the electron and hole wave functions. The exciton energy levels in 2D can be described as [Zaslow 1967]

$$E_n^{2D} = E_B^{3D} \cdot \frac{1}{(n - \frac{1}{2})^2}. \tag{1.5}$$

For the ground state $n = 1$, the binding energy is four times larger than for the 3D case, meaning that excitonic effects are more pronounced in low dimensional systems. A further enhancement of the exciton binding energy occurs due to a reduction of the dielectric screening. In atomically thin 2D systems the exciton wave function expands outside the material, where the dielectric constant is different, as shown in Figure1.5(a). In two dimensional TMDCs, the dielectric screening is weak due to the electric field joining electron and hole extending outside of the material, which leads to an dramatically enhanced Coulomb interactions

[Chernikov 2014]. Both the reduced dimensionality as well as the screening effects described above contribute to the much larger exciton binding energies observed in 2D materials. Typical exciton binding energies observed in these materials are $\simeq 0.1 - 1\,\mathrm{eV}$ [Duong 2017, Thygesen 2017]. Therefore, excitonic effects dominate even at room temperature since the exciton binding energy is larger than $K_B T$ even at $T = 300\,\mathrm{K}$ [Xiao 2017].

In atomically thin layered materials also the quasi-particle band gap is modified with respect to bulk. The band gap strongly changes following the evolution of the electronic structure with the changing number of layers. In addition, the band gap can also be modified by a change of the dielectric environment. Figure 1.6 (a) shows a schematic of excitons in a thin layered material partly covered by a dielectric layer together with the change of the band gap [Raja 2017].

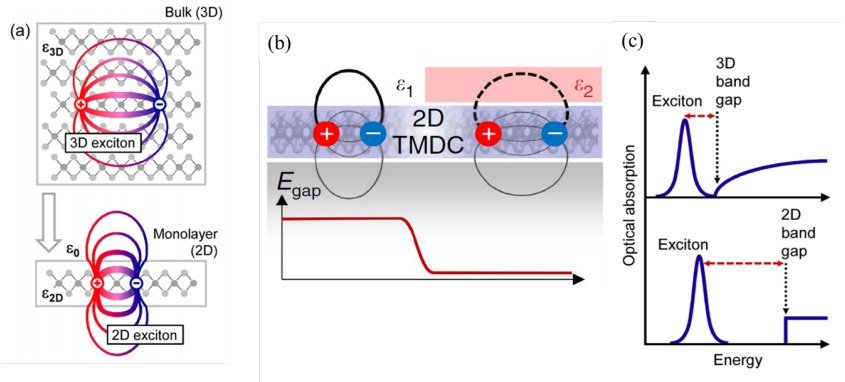

Figure 1.6: (a) Real-space representation of electrons and holes bound into excitons for the three-dimensional bulk and a quasi-two-dimensional monolayer. The changes in the dielectric environment are indicated schematically by different dielectric constants ϵ_{3D} and ϵ_{2D} and by the vacuum permittivity ϵ_0. (b) Influence of the dielectric environment on the quasi-particle band gap and the electron-hole interaction. After[Raja 2017](c) Impact of the dimensionality on the electronic and excitonic properties on the optical absorption.[Chernikov 2014].

However, equation 1.5, which is derived from the hydrogen model is not suitable to describe the exciton energies for an inhomogeneous dielectric environment. The divergence from the 2D hydrogen model was experimentally shown for monolayer WS_2 by Chernikov and co workers (see Fig. 1.7 (a)) [Chernikov 2014]. The disagreement is largest for the ground (1s) state, and is still significant for 2S, while the higher excited states continue to follow rather well the 2D hydrogen model. The reason for this is related to the size of the exciton wave-function of the 1s, 2s and higher states, as presented in Fig. 1.7 (b). The more tightly the exciton state is bound, the more of it's wave function leaks outside the monolayer, where the screening is strongly reduced leading to a strong enhancement of the exciton binding energy[Chernikov 2014].

Alternative models, which takes into account inhomogeneous dielectric screening

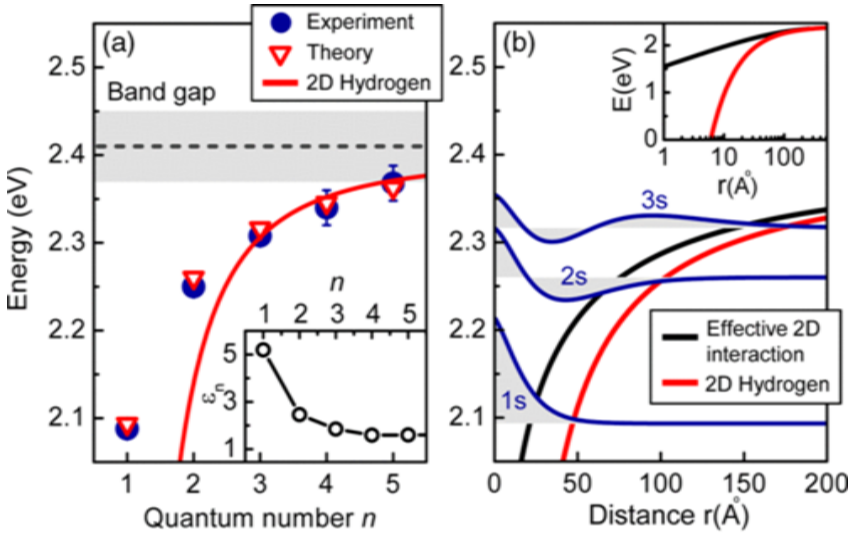

Figure 1.7: (a) Energies of the ground and excited exciton states in ML WS_2 determined experimentally and calculated theoretically, together with a fit of the 2D hydrogen model to the three highest states. (b) Comparison of the nonlocal screening model interaction potential and the 2D hydrogen model and the radial wave-functions for the lowest exitonic states. After[Chernikov 2014].

have been used to describe the deviation from the hydrogenic model in layered materials. The equation derived by Rytova [Rytova 1967] and Keldysh [Keldysh 1979] are employed to describe this modified Coulomb potential energy for point charges in thin layers [Prada 2015]

$$V_{2D}(r) = -\frac{e^2}{8\epsilon_0 \bar{\epsilon} r_0} \frac{\pi}{2} \Big[H_0\Big(\frac{r}{r_0}\Big) - Y_0\Big(\frac{r}{r_0}\Big) \Big], \tag{1.6}$$

where $\bar{\epsilon} = (\epsilon_1 + \epsilon_2)/2$, $r_0 = d\epsilon/(\epsilon_1 + \epsilon_2)$, ϵ_1 and ϵ_2 are the dielectric constants of the surrounding media, d is the thickness of the 2D material and ϵ is its bulk dielectric constant. H_0 and Y_0 are the Neumann and Struve Bessel functions. In this model, the Coulomb interaction increases strongly with decreasing film thickness for $\epsilon_{2D} > \epsilon_0$, which is clearly see in the inset of the Fig. 1.7 (a). This model very well describe the experimental results for the energies of the excitonic series, as shown in Fig. 1.7(a). Figure 1.7 (b) shows a comparison of the Rytova-Keldysh potential, the 3D $1/r$ Coulomb potential, the logarithmic approximation of equation 1.6 valid for $r << r_0$, and the potential suggested as an approximation of the Rytova Keldysh potential by Cudazzo and co-authors as a function of r/r_0. The difference between the 3D Coulomb and other potentials becomes significant for r smaller than the screening length r_0 [Cudazzo 2011] .

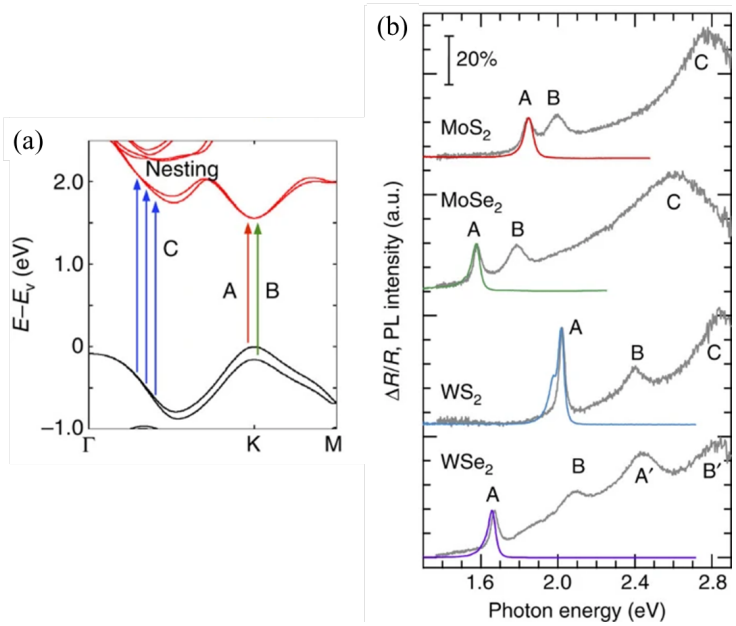

Figure 1.8: (a) The band structure of monolayer MoS_2 calculated using DFT. The arrows indicate the transitions of excitons A and B. (b) PL spectra (red, green, blue and purple curves) and differential reflectance spectra (grey curves) of monolayer MX_2 flakes on quartz substrates. After[Kozawa 2014]

1.3.3 Excitons in 2D transition metal diachalcogenides; the role of SOC

As mentioned before, the top and the bottom of the conduction bands are mainly composed of d-orbitals, which is a source of a strong split orbit coupling. The splitting of the bands induced by SOC is very large in the valence band (of the order of a few hundred meV), being much smaller in the conduction band [Liu 2013a]. Therefore, in the absorption spectra of monolayer TMDCs, in addition to the lowest excitonic transition (exciton A), an additional excitonic transition (exciton B) is observed at higher enrgies. This transition originates from the SOC splitting of the valence band, as schematically shown in Fig. 1.8. The energetic separation of the A and B excitonic transitions corresponds well to the value of the SOC induced splitting in the valence band. At even higher energies, an additional transition (exciton C) is observed which is related to band nesting[Kozawa 2014].

The spin orbit coupling is around an order of magnitude weaker in the conduction band than in the valence band [Liu 2014]. Nevertheless, the SOC splitting of the conduction band has a dramatic impact on the excitonic properties and valley polarization. The schematic of the spin splitting in the valence and the conduction band for MoX_2 and WX_2 monolayers is shown in Fig. 1.9 (a). In both Mo- and W-based materials the spin orbit splitting results in two different excitonic transitions, namely bright and dark. The bright exciton transitions are optically allowed and involves the electron and hole with the same spin, while the spin-forbidden,

dark exciton transition involves electrons and holes with opposite spin. Typical, literature values of the bright-dark exciton splitting (ΔE) for different TMDCs are indicated in Fig. 1.9 (b). The main and most importance difference between Mo- and W-based materials is the sign of ΔE, which is negative for Mo - based monolayers and positive for W - based monolayers. Therefore, the ground state is bright for MoX_2 and dark for WX_2, as indicated by the arrows in the Fig. 1.9 (a). The first experimental confirmation of the dark/bright character of the excitonic ground state in MoX_2 and WX_2 monolayers was presented by Zhang and co workers using temperature dependent PL measurements [Zhang 2015]. The results of this experiment are presented in Fig. 1.9(c), where the integrated photoluminescence intensity of the exciton emission is plotted as a function of the temperature. Note that the emission at low temperatures is quenched for WSe_2, which is explained by the relaxation of the carriers to a ground state which is non emissive (dark state). Moreover, the intensity of the exciton emission in WSe_2 increases with temperature, consistent with a thermal activation of carriers from a dark ground state to an optically bright, emissive state. In contrast, in MoX_2, where the ground state in optically bright, the intensity of the emission decreases with increasing temperature due to the enhanced exciton-phonon coupling [Zhang 2015].

The sign of the spin splitting in the conduction band has a critical impact on the valley polarization. Baranowski and co-authors demonstrated using a simple rate equation model, that the inter-valley scattering, which is mediated by the electron–hole exchange interaction, is effective only for bright exciton states. A dark exciton ground state provides a robust reservoir for valley polarization, which tries to maintain a Boltzmann distribution of the bright exciton states in the same valley via intra-valley bright dark exciton scattering mechanism leading to a significant valley polarization only in W based monolayers, were the ground state in dark [Baranowski 2017a].

1.3.4 Charged excitons in 2D transition metal dichalcogenides

Charged excitons (trions) in doped semiconductors, which result from binding an extra electron or a hole to a neutral exciton, were first predicted in 1958 [Lampert 1958]. Typically the binding energy of a charged exciton is very small, making them difficult to observe in 3D semiconductors, requiring low temperatures and very high quality crystals [Thomas 1977]. In low dimensional systems the observation of the charged excitons is simpler due to the increased binding energy. The first observation of a charged exciton was demonstrated in a CdTe quantum well by Kheng and co-authors [Kheng 1993]. As a neutral exciton can be treated as an analogy to a hydrogen atom, negatively charged exciton can be treated as hydrogen atom with with extra electron (H^-) while positively charged exciton as ionized hydrogen molecule (H^{2+}). The energy of the charged exciton is lower than the neutral exciton, therefore, in the absorption and photoluminescence spectrum they are observed at energies below neutral excitons. The binding energy of charged excitons is around 10-20% of the neutral exciton binding energy, limiting the observation of

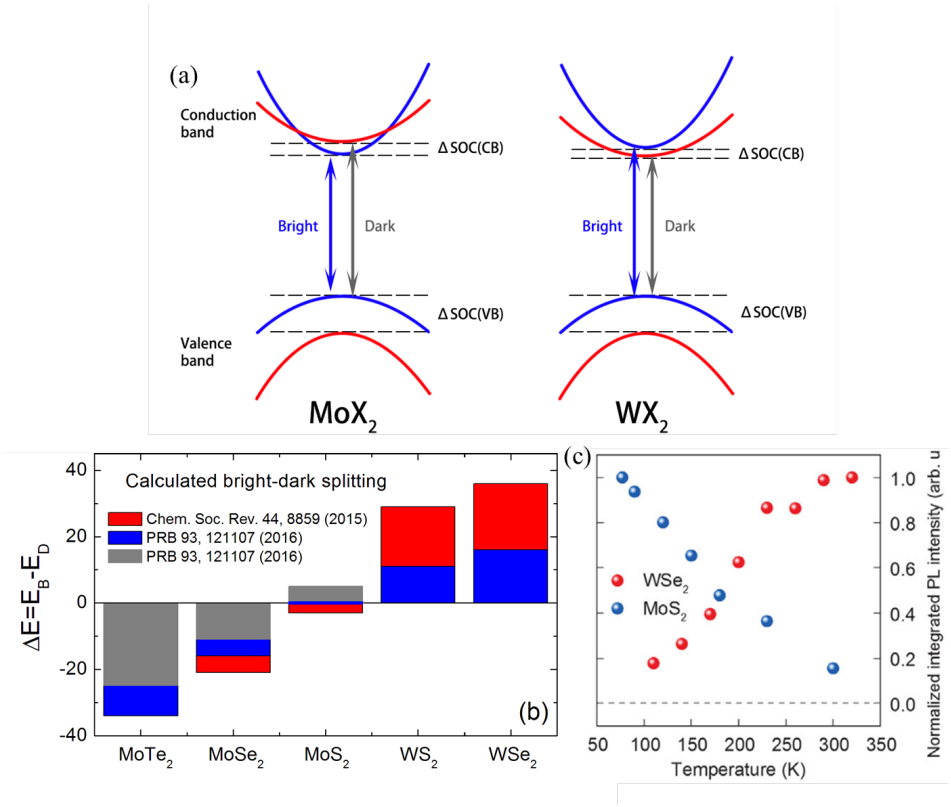

Figure 1.9: (a) Schematic of the conduction and valence band spin splitting. The arrows mark the bright and dark exciton transitions for MoX_2 and WX_2 monolayers, respectively. (b) Literature data for the calculated difference between bright and dark excitons. (c) Comparison of temperature dependence of the time-integrated PL intensity of WSe_2 and MoS_2, after[Zhang 2015].

charged excitons in the classic quantum wells such as GaAs or CdTe to very low temperatures [Kheng 1993, Finkelstein 1995, Shields 1995]. However, the charged exciton binding energy in monolayer TMDC is almost one order of magnitude larger (a few tens meV) than that in classic 2D systems due to the enhanced Coulomb interactions [Mak 2013]. This makes the observation of the charged exciton possible even at room temperature in TMDC [Cadiz 2016b].

The combination of the spin and valley degrees of freedom leads to multiple charged excitonic states in monolayer TMDC, with 12 negatively charged and 4 positively charged excitons, as presented in Fig. 1.10. These states are at least doubly degenerate due to time reversal symmetry. Negatively charged excitons can have intra-valley or inter-valley character. The intra-valley negatively charged exciton is a hole and two electrons in the same valley. For intra-valley trion, according to the Pauli exclusion principle, the two electrons have to reside in different spin states (in upper and lower spin split conduction band) . Thus, the intra-valley trion is a spin-singlet. The inter-valley negatively charged exciton is composed of two

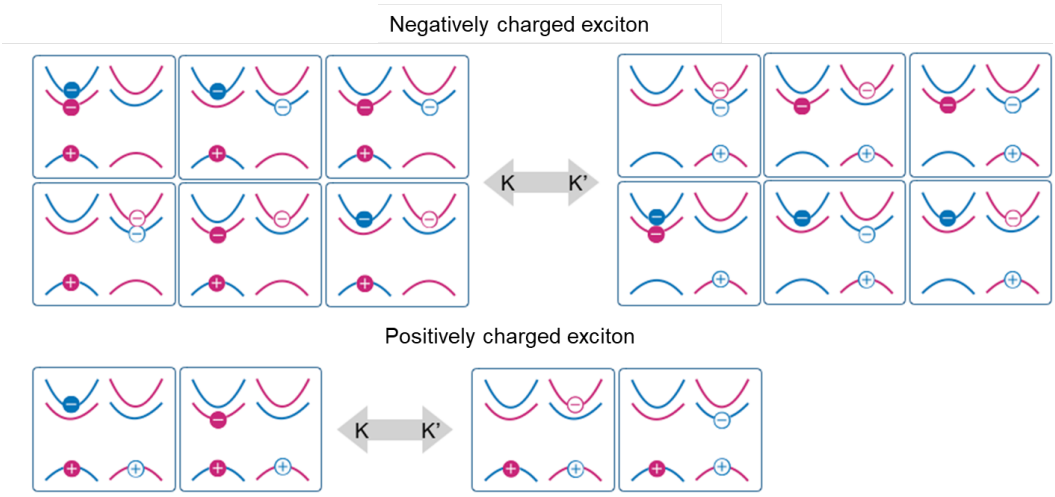

Figure 1.10: Schematics showing the possible spin and valley configurations of the negatively and positively charged excitons. After[Chen 2018a]

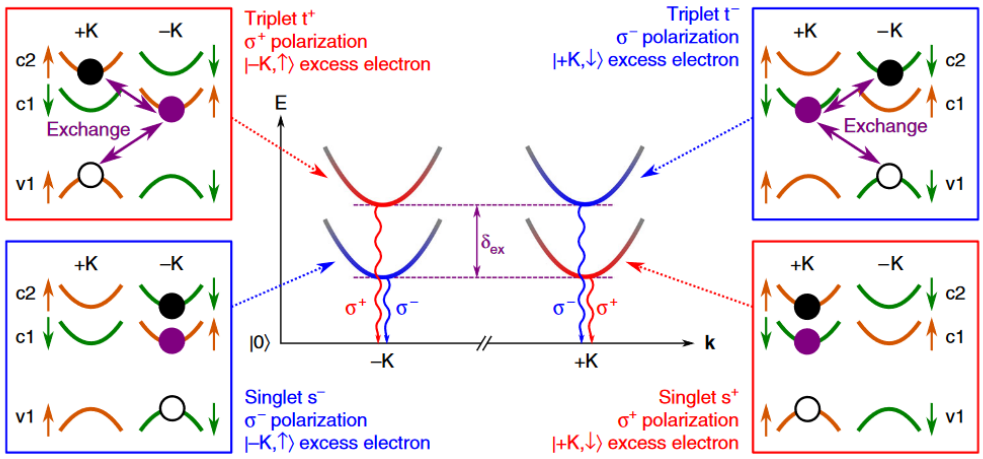

Figure 1.11: Schematics showing the possible spin and valley configurations of negatively and positively charged exciton. After[Lyons 2019]

electrons located in different valleys and can form a spin singlet or triplet.

Inter-valley Coulomb exchange interaction lifts the degeneracy between the states of the singlet and triplet charged excitons, as shown in Fig. 1.11. Singlet states have lower energy than triplet one, with the splitting calculated to be around 6 meV [Yu 2014] and confirmed experimentally to be of the order of few meV [Plechinger 2016b, Lyons 2019]. The charged excitons follow the circular polarization of the excitons as shown in Fig. 1.11.

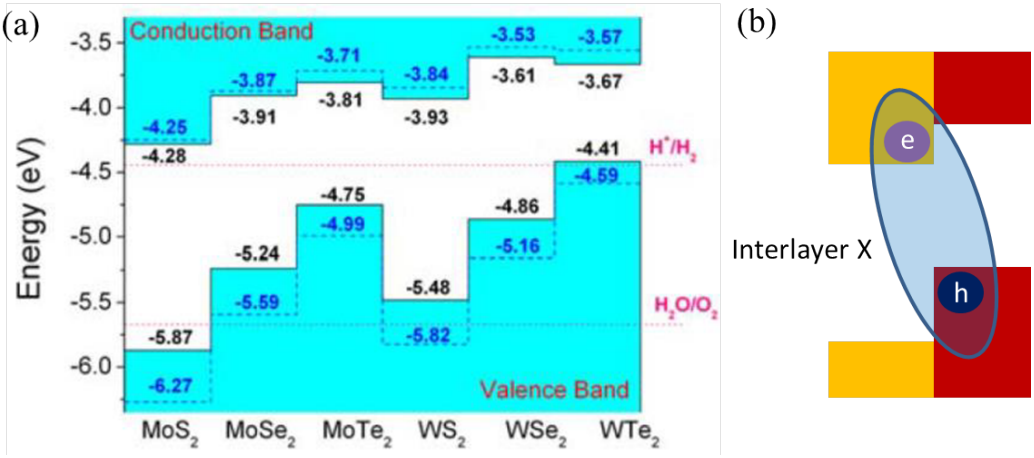

Figure 1.12: (a) Calculated band alignment for MX_2 monolayer. After [Kang 2013]. (b) Schematic representation of the charge transfer and inter-layer exciton formation after photo-excitation.

1.4 Van der Waals (vdW) heterostructure

Probably one of the biggest advantages of layered semiconductors is the possibility to stack them in any desired combination with other layered semiconductors without limitations related to lattice mismatch characteristic for covalent crystals. Therefore, the vertical stacking of monolayer solids provides a new rich playground that can be used to tailor properties giving rise to new and attractive features [Geim 2013, Novoselov 2016]. In case of classic III-V or II-VI or group IV semiconductor heterostructures the constituting layers must have the same (similar) lattice constant to avoid strain which often deteriorates the quality of such structures. Moreover, the combinations of materials which can stacked while preserving good quality is very limited. In contrast, the plethora of different layered materials allows to efficiently tailor or improve desired features of van der Waals heterostructures. For example, sandwiching TMDC monolayers between layers of hexagonal boron nitride (hBN) improves significantly their optical and electrical properties [Cadiz 2017, Fallahazad 2016], providing access to their rich excitonic and transport physics [Cadiz 2017, Fallahazad 2016, Robert 2018, Manca 2017, Stier 2018, Chen 2018b, Xu 2017, Movva 2017, Bandurin 2017, Wu 2016]. Stacks with graphene allows to locally control the dielectric environment [Raja 2017] and in this way the band gap of the TMDC layer.

Another very interesting property of TMDC van der Waals heterostructures is the relative band alignment. The theoretical calculated band alignment of TMDC heterostructures performed by Keng and co authors [Kheng 1993], are summarized in Fig. 1.12 (a). Almost all TMDC heterostructures have a type II band alignment with the lowest energy bands for electrons and holes located in different layers. The type II band alignment leads to a rapid charge transfer of optically

excited carriers in TMDC vdW heterostructures. The electrons and holes, which accumulate in different layers after the charge transfer, are bound together via Coulomb interaction to form a inter-layer excitons as shown in Fig. 1.12(b). In TMDC, the inter-layer exciton was first reported in a $MoSe_2/WSe_2$ heterostructure [Rivera 2015]. The inter-layer exciton consists of spatially separated charge carriers. The spatial overlap of the electron and hole wavefunctions is reduced, which results in a dramatically enhanced lifetime of inter-layer excitons. First-principles calculations estimate that the oscillator strength of inter-layer excitons is much smaller than that of intra-layer exctions, while photo-current spectroscopy measurements of $MoSe_2/WSe_2$ heterostructure show that the photo-current of inter-layer excitons is 200 times smaller than for intra-layer excitons, suggesting that the oscillator strength is two order of magnitude smaller than that of intra-layer excitons [Ross 2017]. The small oscillator strength suggests a much longer radiative lifetime of inter-layer exciton together with a longer valley depolarization lifetime. This is very beneficial from the point of view of developing valleytronic applications.[Xiao 2012, Xu 2014, Wang 2012, Mak 2012, Zeng 2012]. The extremely short lived excitations in TMDC layers[Lagarde 2014a, Wang 2014, Robert 2016, Wang 2015b, Zhu 2014] can be substituted by inter-layer exciton in TMDC heterostuctures, with a lifetime which is few orders of magnitude longer[Baranowski 2017b, Rivera 2016]. Type II band alignment is common for most combination of TMDC layers [Kang 2013, Dong 2017, Zhou 2018], providing large variety of heterostuctures with long exciton lifetime while at the same time maintaining most of the crucial feature of monolayer *i.e.* the possibility to selectively excite different valleys.

To determine the band structure, different experiments have been performed including for example sub-micrometer angle-resolved photo-emission spectroscopy (μ-ARPES)[Wilson 2017], microbeam X-ray photoelectron spectroscopy (μ-XPS) [Chiu 2015]. The experimental results confirmed the type II band alignment of TMDC heterostructures. According to theory, the inter-layer hopping strength is much smaller than the corresponding band offset at the K(-K) points [Wang 2017], so the layer hybridization is negligible. However, the inter-layer hopping strength in the Γ and Λ points are comparable to the band offset, thus, the layer hybridizations and the energy shifts are strong. The hopping strength decays exponentially with inter-layer distance d and the energy at Γ and Λ points also depend on d [Komsa 2013, Heo 2015]. The inter-layer excitons are not optically bright in all heterostructures. They only exist in heterostructures with finite inter-layer coupling and close rotational alignment of monolayer TMDC [Nayak 2017]. The PL intensity depends strongly on the stacking angle between monolayer TMDC. The PL signal is strongest near 0° and 60°. Due to the large band offsets and exciton binding energy, the dissociation of intra-layer exciton is rapid, so that the charge transfer is not stacking angle dependent [Zhu 2015].

Finally, a very particular phenomena observed in van der Waals heterostructures is the formation of a long-period moiré potential. In general a moiré pattern is an interference produced by a superposition of two slightly different periodic grids,

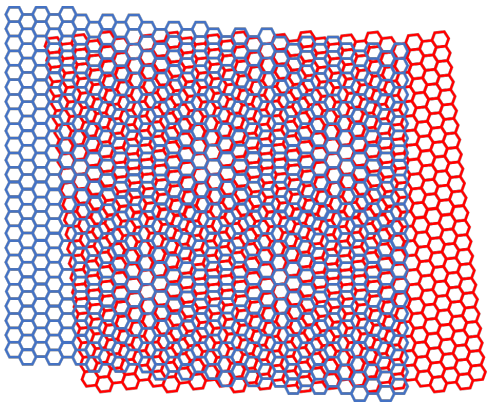

Figure 1.13: Scheme of the formation of the moiré pattern for two hexagonal lattices.

lattices or templates. The difference in period, orientation and/or relative shift between the two templates leads to the formation of new, slowly varying pattern which is commonly referred to as moiré fringes. A very simple example is the superposition of two rotated grids as shown in figure 1.13.

The weak van der Waals interaction causes that in TMDC heterostructures each of the layer preserve it's own lattice constant, in other words monolayers do not conform to each other which leads to extremely interesting new physics. Since both layers are crystals with a periodic atom distribution, any difference in the lattice parameters or twist angle between them will result in the formation of a moiré pattern [Park 2008, Xue 2011, Yankowitz 2012, Ponomarenko 2013, Yu 2017, Zhang 2017].

In the last few years moiré structures have gained considerable interest within the solid state physics community with the realisation that the physical properties of a system can be controlled by the twist of layers. The first studies of physics related to the moiré pattern has been shown for hBN/graphene heterostructures, where the induced periodic potential leads to the formation of new Dirac cones, opening of a band gap, and the appearance of Hofstadter butterfly states [Hunt 2013, Wang 2016a, Yankowitz 2012, Ponomarenko 2013, Dean 2013]. More recently, an even more spectacular example of *twisted* physics was show for two rotated layers of graphene. Rotating them by 1.1 degrees with respect to each other induces superconductivity in normally insulating bilayer of graphene[Cao 2018]. It is expected that the moiré pattern formed in TMDC heterostructures should also have a large influence on their properties [Yu 2017, Zhang 2017, Wu 2018, Wu 2017a]. According to theoretical predictions, the moiré pattern should result in a periodically modulated potential with minima for both intra- [Wu 2017a, Yu 2017] and inter-layer [Yu 2017, Wu 2018] excitons, spatially varying selection rules of interlayer transitions [Yu 2017, Wu 2018]. Moreover, the variation of the confinement potential for different atomic registries should lead to a splitting of both the intra- [Wu 2017a] and inter-layer transitions [Yu 2017, Wu 2018] with the formation of an effective matrix of quantum dots due to the periodically modulated moiré potential.

Chapter 2

Experimental techniques and sample characterization

Contents

2.1 Optical spectroscopy 19
2.1.1 Steady-state micro- spectroscopy 21
2.1.2 Time-resolved Photoluminescence 21
2.1.3 Polarization optics 22
2.2 Micro-PL in dc magnetic field 23
2.3 Sample characterization 24
2.3.1 Chemical vapor deposition grown monolayer and van der Waals heterostructures 24
2.3.2 Exfoliated monolayer and hexagonal boron nitride encapsulation 26

The experimental techniques used in this thesis are introduced in this chapter. All the measurements performed are based on spectroscopic methods, namely photoluminescence (PL), reflectivity, non resonant Raman scattering and second harmonic generation. We then briefly outline the high dc magnetic field measurements performed during visits to the EMFL High Magnetic Field Facility in Nijmegen. Finally, for completeness, we provide a brief description of how the samples investigated in this thesis were prepared.

2.1 Optical spectroscopy

In this thesis, we utilize different spectroscopy techniques to investigate the optical properties of transition metal dichalcogenides (TMDC). In particular, we use micro-photoluminescence (μPL) to characterize the emission properties, micro-reflectivity to characterize the inter-band absorption, micro-Raman scattering spectroscopy is used to distinguish the thickness of the materials, and second harmonic generation is used to measure precisely the stacking angle of the TMDC heterostructures. To investigate the exciton dynamics we have used time-resolved micro-photoluminescence (μPL).

All of the above experiments are carried out in our combined free beam micro-optical setup in LNCMI-Toulouse, which is presented schematically in Fig. 2.1. The setup is divided conceptually into two parts labelled as excitation and detection. In

the excitation part enclosed by the purple dashed line in Fig. 2.1, we have the light sources including continuous wave lasers, a pulsed laser and a white light lamp. In the detection part enclosed by the green dashed line, there are a combination of different detectors. The samples are mounted in a helium flow cryostat with optical access. The temperature is controlled using a MercuryITC temperature controller, which allows us to measure in the temperature range 2.7K to 500K. The cryostat is mounted on an $x-y$ translation stage driven by two stepper motors, which allows spatial resolved mapping with high resolution. The incident beam is reflected by a non-polarizing cubic beam splitter (or a dichroic mirror for Raman measurement) and focused onto the sample by a $50\times$ magnification objective with a numerical aperture NA $= 0.66$. The typical size of the spot focused on the sample is $1\,\mu\text{m}^2$, which determines the highest resolution of the spatial mapping. To observe the sample mounted in the cryostat *in situ*, we use a white lamp to illuminate the sample and collect the reflected light with a small CCD camera, which provides a real time image of the sample.

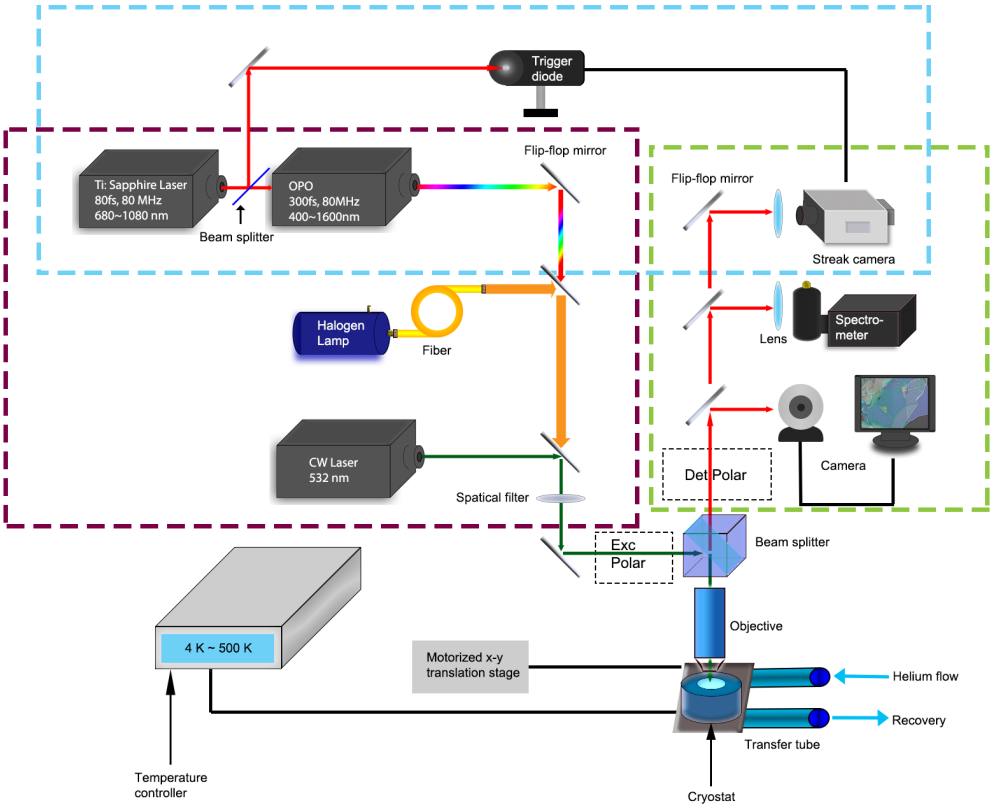

Figure 2.1: Schematic showing the general layout of the micro-spectroscopy setup in LNCMI-Toulouse. Equipment related to the excitation (purple dashed line), detection (green dashed line) and time resolved (blue dashed line) setups are enclosed by the dashed rectangles.

2.1.1 Steady-state micro- spectroscopy

We use a solid-state laser emitting at 532 nm to measure the steady-state μ-PL and μ-Raman. For the measurement of Raman scattering, we use a dichroic mirror to replace the cubic beam splitter. The dichroic mirror reflects the laser while transmitting the Raman signal at longer wavelength than the excitation laser. The silicon phonon mode at 520 cm^{-1} from the substrate or spectral lines from a Neon lamp can be used to accurately calibrate the spectrometer. To measure PL and reflectivity, we usually use a non-polarizing 50/50 cubic beam splitter. The key point of micro-spectroscopy is that the excitation beam passes through a double lens system with a spatial filter (pinhole of diameter of 20 μm) mounted at the common foci of the two lenses. For μ-reflectivity, we couple the white light from a halogen lamp to a fiber and pass through the same spatial filter. Passing all the light source through the spatial filter allows us to obtain a spot size on the sample close to diffraction limit (1 μm^2) optimizing the spatial resolution of the system.

2.1.2 Time-resolved Photoluminescence

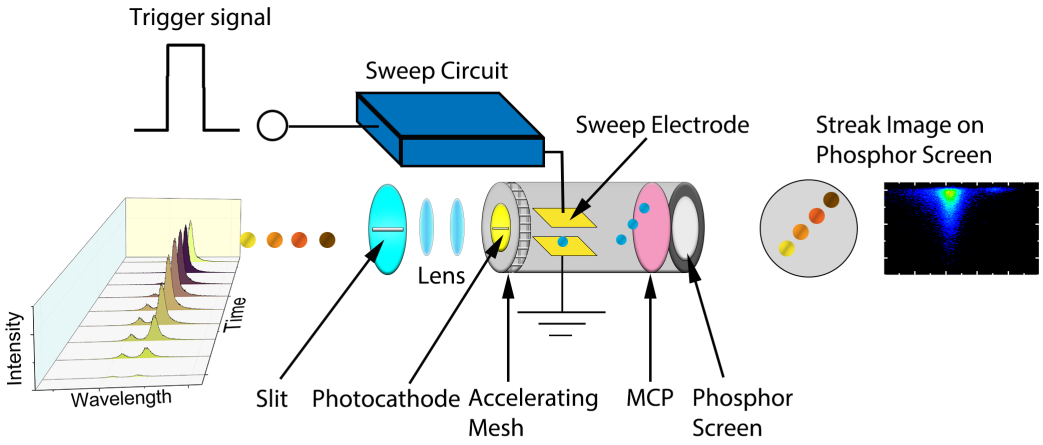

Figure 2.2: Operating principle of the streak tube used for time resolved photoluminescence.

To characterize the exciton dynamics, we perform time-resolved PL (TRPL) measurements. The setup for TRPL is enclosed by the blue dashed line in Fig. 2.1. To measure time-resolved photoluminescence, we excite the sample with a pulsed laser. In our experiment, we use femtosecond pulses generated by a tunable frequency-doubled optical parametric oscillator (OPO), which is synchronously pumped by a mode locked Ti:Sapphire laser. The pulse duration and spectral width of the OPO are 300 fs and 3 meV, respectively with a the repetition rate of 80 MHz. The wavelength of the OPO can be tuned from 400 to 1600 nm. The Ti:Sapphire laser used for pumping the OPO has a typical pulse width of 80 fs and a range

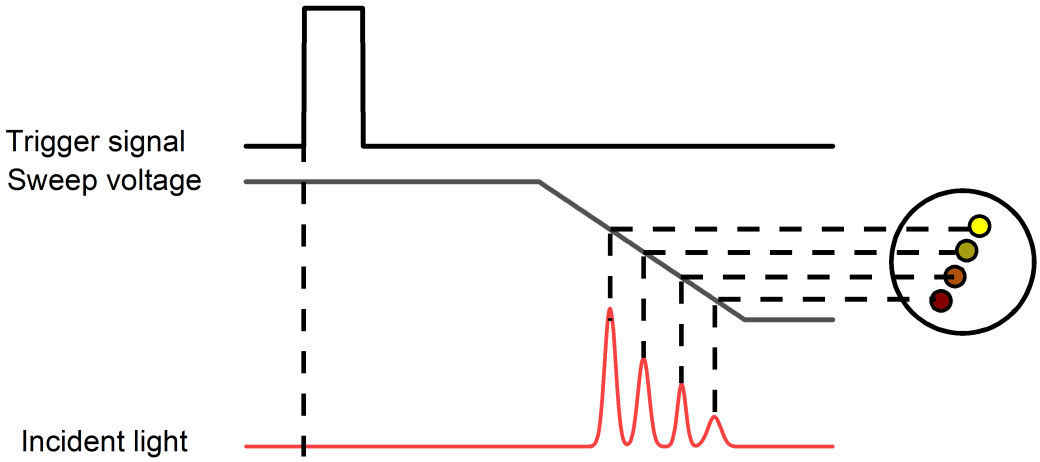

Figure 2.3: Schematic showing the operation of a streak camera during the voltage sweep.

of tunable wavelength between 680 and 1060 nm. For detection, we use a Hamamatsu Streak Camera equipped with a synchro-scan unit. The operating principle of the streak camera is shown in Fig. 2.2. The streak image provides 3 dimensional information, representing the distribution of the photon intensity as a function of wavelength and time. In a streak image, one axis is spectrally-resolved and the one axis is time-resolved. There is a monochrometor at the entrance of the streak camera CCD which disperses the light signal as a function of wavelength. To analyse the photons as a function of emission time, we use a photocathode to convert the photons to electrons, and then the converted electrons are accelerated along the evacuated tube and pass between a pair of sweep electrodes, where a time-varying voltage is applied to the electrodes, resulting in a high-speed sweep, as shown in Fig. 2.3. The sweep electrodes is synchronized to the Ti:Sapphire laser via a trigger diode as shown in Fig. 2.1. In this way, the electrons which arrive later are deflected less than the electrons which arrive early. The number of electrons is amplified by the micro channel plate (MCP) many thousands of times. The phosphor screen behind MCP is hit by the electrons converting them to spatially separated photons again. A CCD camera is used to read the images from the phosphor screen.

2.1.3 Polarization optics

We can introduce polarization optics into the optical path to measure polarization resolved-PL, Raman, and second harmonic generation, both in the excitation and detection path. In the excitation beam, we place a Glan-Taylor polarizer to define the linear polarization of the laser. The polarization direction can be rotated by a half wave-plate, which is placed after the polarizer. To obtain circular polarized excitation, we use a quarter wave plate to replace the half wave plate. In this case

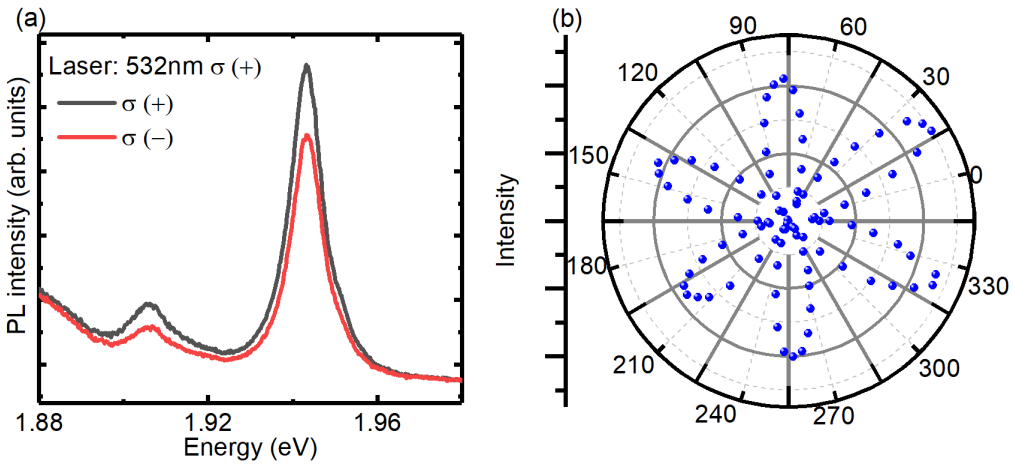

Figure 2.4: (a) The typical circular polarization resolved PL measured on MoS_2 monolayer. The PL intensity is analyzed in σ^+ and σ^- circular polarization, respectively. (b) Linear polarization resolved second harmonic generation measured on $MoSe_2$ monolayer.

we set the relative angle between the polarizer and the fast axis of the quarter wave plate to 45 degrees. For the detection, we place a second Glan-Taylor polarizer either perpendicular or parallel to the polarization direction of the excitation beam and employ a half wave-plate or quarter wave-plate prior to the polarizer to analyse the linear or circular polarization, respectively. Typical circular polarization resolved PL is presented in Fig. 2.4(a). The MoS_2 monolayer is excited by σ^+ laser and detected in both co-polarized (σ^+) and counter-polarized (σ^-), respectively. In Fig. 2.4(b), we show a typical result of linear polarization resolved second harmonic generation. In the excitation path, we use a motorized half wave-plate behind the excitation polarizer to change the azimuthal angle θ between the excitation laser polarization direction and the armchair direction of the sample. In the detection path, the second motorized half wave-plate prior to detection polarizer is rotated in the opposite direction - θ to the excitation half wave-plate synchronously in order to keep the polarization direction of second harmonic response to be parallel to the excitation polarizer. Since monolayer $MoSe_2$ has a three-fold rotational symmetry, the second harmonic generation from the monolayers with the polarization parallel or perpendicular to the incident laser polarization exhibits a six-fold symmetry with the intensity proportional to $cos^2 3\theta$ or $sin^2 3\theta$, respectively. We can choose to detect the component which is parallel (perpendicular) to the incident laser by setting the detection polarizer parallel (perpendicular) to excitation polarizer.

2.2 Micro-PL in dc magnetic field

To perform magneto-optical measurement of TMDC vdW heterostructures, we travelled to the high field magnet laboratory (HFML) in Nijmegen. The HFML is an

international facility, which is specialized in direct current (dc) high magnetc fields. The magnetic fields at HFML are available up to 37.5 Tesla using their 20 MW installation. The measurement was performed in the Faraday configuration ((light wavevector parallel to B)) in a 32 mm bore, 33 T Florida-Bitter magnet. The optical the probe is a carbon tube that is rigid, non-reflecting and non-magnetic. The sample is mounted on $x-y-z$ piezo positioners at the head of the probe. The piezo positioners from the Attocube company are designed to work under extreme environmental conditions (low temperature and high magnetic field) permitting a nanoscale shift of the sample. A long working distance (12 mm) objective is mounted above the positioners. The $x-y$ positioners are used to change the in plane relative position between sample and objective to achieve microscale spatial resolution, while the z positioner is used to change the relative distance between the sample and the objective *i.e.* to focus. An optical window mounted on the top of the probe provides the free beam optical access. The optical configuration here is quite similar to the micro spectroscopy setup in LNCMI Toulouse. A non-polarizing cube beam splitter is used to reflect the laser into the probe and transmit the signal emitted from the sample. A liquid nitrogen cooled CCD is used to detect the PL signal. Polarization optics can be introduced to the excitation and detection paths. For example, we introduced circular polarization optics to measure valley Zeeman splitting of TMDC. The probe is pumped to evacuate the air first and then back-filled with helium exchange gas and placed in a liquid helium cryostat.

2.3 Sample characterization

2.3.1 Chemical vapor deposition grown monolayer and van der Waals heterostructures

Chemical vapor deposition (CVD) provide a very promising tool to produce large-scale TMDC monolayers and van der Waals (vdW) heterostructures with systematic control of the thickness, size, and uniformity of two dimensional materials. Our CVD-grown $MoSe_2/MoS_2/MoSe_2$ vdW heterostructure was prepared by the research group of Professor Andras Kis in EPFL, Lausanne. To prepare CVD-grown MoS_2, c-plane sapphire substrates are used to achieve the control of crystallographic orientation. Before the CVD growth process, the substrate is cleaned using acetone/2-propanol/deionized-water and the substrates are annealed in air for one hour at 1000°C to obtain atomically smooth sapphire terraces on the surface. The substrates are placed face-down on a crucible with $\simeq 5$ mg of MoO_3 and loaded into a split-tube three-zone CVD furnace with a 32 mm outer diameter quartz tube. The second crucible with 350 mg of sulfur is located upstream from the growth substrates. Argon gas is used to carry MoO_3 and sulfur which is evaporated from solid sources for the reactions. The CVD-grown monolayer $MoSe_2$ is prepared in a similar way.

After CVD-grown monolayer MoS_2 and $MoSe_2$ is prepared, the $MoSe_2/MoS_2/MoSe_2$ vdW heterostructure are fabricated by two sequential

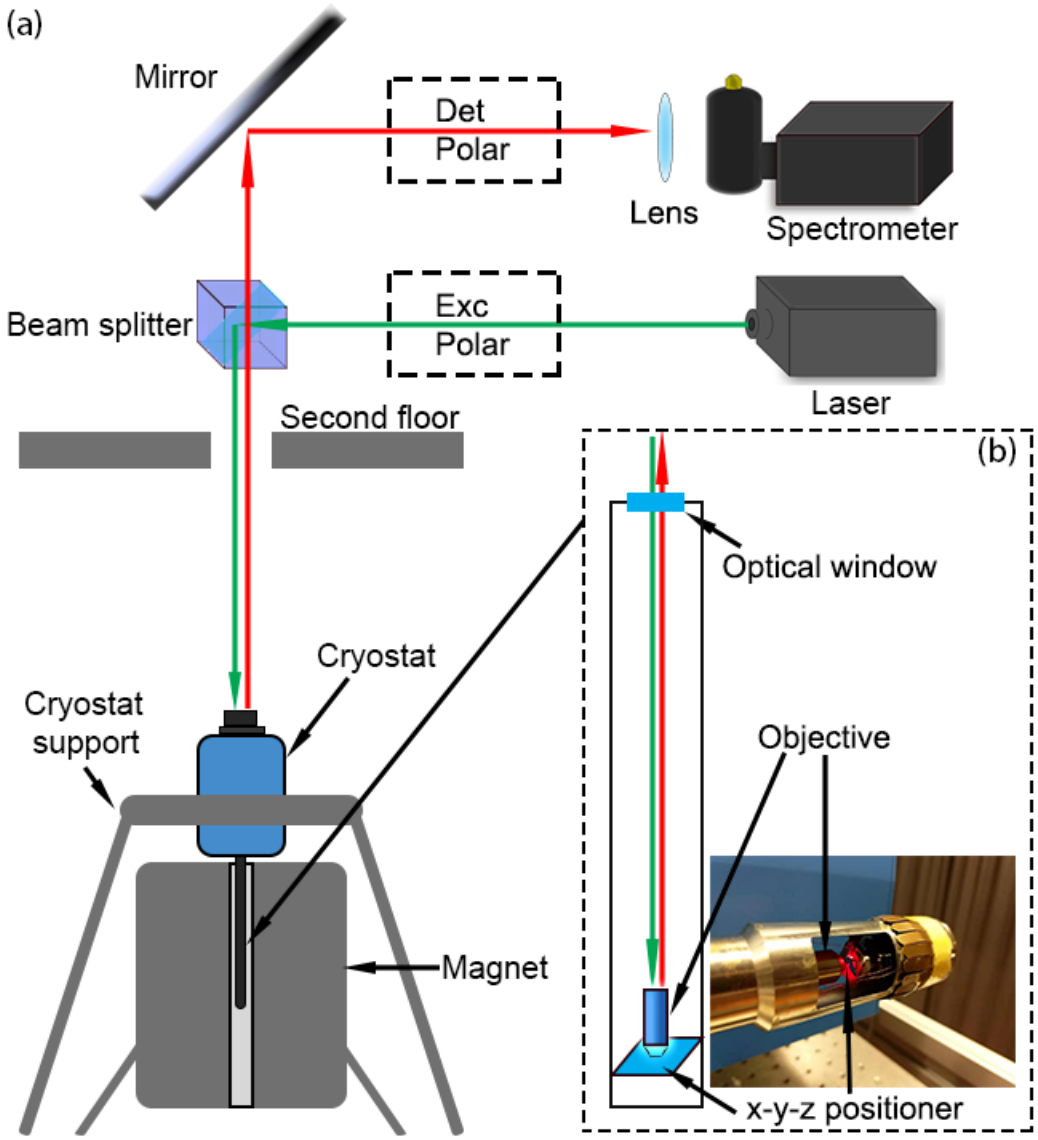

Figure 2.5: (a)Schematic showing the general layout of the micro-spectroscopy setup in dc magnetic field in HFML-Nijmegen. (b) Schematic of the optical insert.

transfer steps using a wet transfer KOH method. The sapphire substrate is spin coated with PMMA at 1500 rpm for 60 s and annealed at 180°C for 5 minutes. Then, the films are detached in KOH (30%) at moderate temperatures (70°C), washed three times in deionized water and transferred onto the sapphire with the stacking layer. The PMMA can be removed by dipping the sample in acetone for 12 hours, followed by rinsing with isopropanol and drying in a N_2 flow. With this transfer method, the upper-layer MoS_2 is first transferred to as-grown $MoSe_2$ on substrate and the subsequently $MoS_2/MoSe_2$ stack is transferred to the as-grown bottom MoS_2 monolayer.

2.3.2 Exfoliated monolayer and hexagonal boron nitride encapsulation

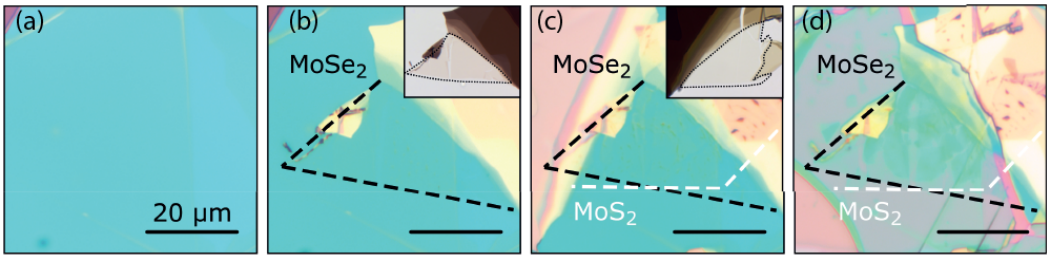

Figure 2.6: Optical microscope images of (a) the hBN flake used as the substrate, (b) the MoS_2 and (c) $MoSe_2$ flakes and (d) the hBN flake used as the capping layer. The insets in panels (b) and (c) show the corresponding flakes as exfoliated, before the transfer on the hBN substrate. The scale bar is 20 μm for all the panels.

Even though CVD growth provides a scalable fabrication platform for vdW heterostructures, it is still hampered by poor sample quality. The CVD grown MoS_2 and $MoSe_2$ always exhibit broad emission from defect bound excitons in the low-temperature PL. This emission from bound states, which is related to chalcogen vacancies generates during the CVD process, is usually more intense than the free exciton peak. The monolayer flakes exfoliated from a bulk crystal generally have better optical quality than CVD-grown samples. Fortunately, the encapsulation of monolayer TMDC in hexagonal boron nitride (hBH) suppresses the inhomogeneous broadening of the exciton linewidth and improves the optical quality significantly. Therefore, encapsulating vdW heterostructure in hBN has become a necessary step in TMDC vdW heterostructure fabrication.

In our study, Professor Andres Castellanos-Gomez's group from ICMM (Madrid) prepared us $MoS_2/MoSe_2$ encapsulated in hBN. An all-dry deterministic transfer of mechanically exfoliated flakes was used. The hBN flakes are exfoliated from a commercially available hBN powder (Momentive, Polartherm grade PT110) using Nitto tape (Nitto Denko corp. SPV 224). The MoS_2 and $MoSe_2$ monolayers are also exfoliated from bulk crystal by Nitto tape and the bulk MoS_2 and $MoSe_2$ were synthesized by chemical vapor transport. The exfoliated flakes are transferred to a Gelfilm (WF $\times$4 6.0 mil by Gelpak), which is used as a viscoelastic stamp to perform the deterministic transfer. The transmittance and reflection spectra prior to transfer are used to choose monolayer flakes of MoS_2 and $MoSe_2$. The MoS_2 and $MoSe_2$ monolayers that have large faceted edges are used to align the heterostructures. The process of vdW heterostructure assembly is shown in FIG. 2.6, the monolayer $MoSe_2$ was transferred to a thick hBN flakes used as the substrate and the monolayer MoS_2 are transferred on the top of $MoSe_2$ to fabricate heterostructure. Finally, a thin hBN flake was used to cover the entire heterostructure.

2.3.2.1 Raman spectroscopy on encapsulated $MoS_2/MoSe_2$ HS

We have performed Raman spectroscopy characterization to verify the possible presence of strain in the encapsulated $MoS_2/MoSe_2$ HS. This was particularly important, for the data presented in Chapter 4 in order to rule out strain as the source of the presence of a doublet structure in the photoluminescence of intra-layer excitons of $MoSe_2$. In Fig. 2.7(a), we show representative Raman spectra measured on the isolated $MoSe_2$ monolayer and on the $MoS_2/MoSe_2$ heterobilayer. Since in the sample the MoS_2 is completely covered by $MoSe_2$, we focus on the A_{1g} mode of the latter material. Uniaxial or biaxial tensile strain is known to induce a red shift the A_{1g} mode. This is also accompanied by a red shift of the PL spectrum [Conley 2013, Lloyd 2016, Castellanos-Gomez 2013]. By performing a detailed analysis of the measured Raman map, we note that the average energy of the A_{1g} mode in the heterostructure region is slightly red shifted by $\sim 0.7\text{cm}^{-1}$ with respect to the same mode measured outside of the heterostructure area (see Fig. 2.7). If this shift were to be attributed to strain, it would be tensile strain. However, this is not consistent with the appearance of a new peak, blue shifted with respect to the main peak, in the PL spectrum of $MoSe_2$. If this peak were to be attributed to strain, it would result from compressive strain, which is not consistent with a red shifted Raman peak in the heterostructure region. This, along with the absence of an additional peak in the PL spectrum of a $MoSe_2$ with 20° tilting angle suggests that the local variation of the strain and, more generally, our fabrication approach, are not the reason for the double peak structure of $MoSe_2$ in the heterostructure.

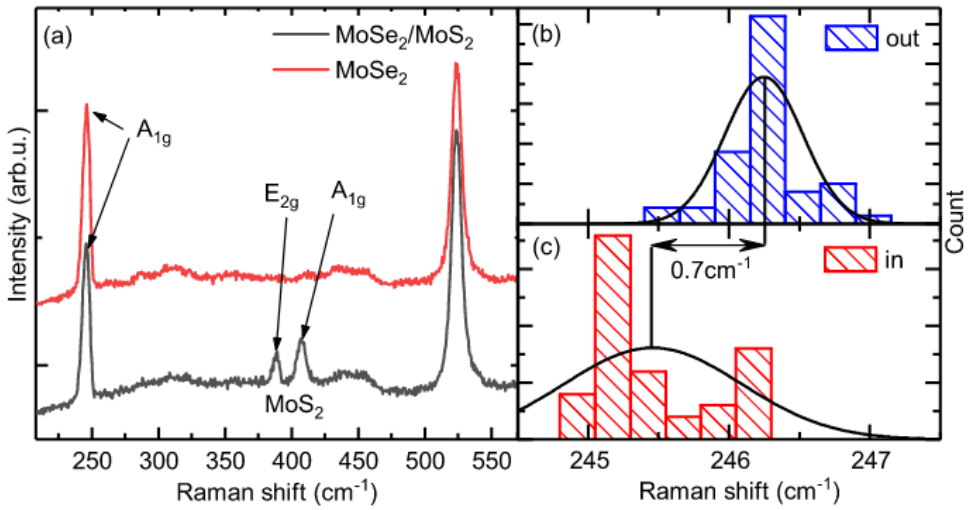

Figure 2.7: (a) Raman spectrum of isolated $MoSe_2$ monolayer (red curve) and $MoS_2/MoSe_2$ heterobilayer (gray curve). Histogram of the Raman peak position extracted after fitting with Lorentzians outside (b) and inside (c) of heterostructure region. The black Gaussian curves represent the position of the mean value and standard deviation of peak positions $A_{1g} = 245.46(246.25)\,\text{cm}^{-1}$ and $\sigma_{A_{1g}} = 0.43(0.28)\,\text{cm}^{-1}$ inside (outside) of the heterostructure region.

Chapter 3

Photodoping effect in $MoSe_2/MoS_2$ heterostructure

Contents

3.1 Introduction 29
3.2 Micro-PL properties of $MoSe_2/MoS_2/MoSe_2$ heterostructure 30
3.3 Photodoping on intra-layer exciton of $MoSe_2$ 30
3.4 Photodoping on interlayer exciton 32
3.5 Photodoping microscopic mechanism 34
3.6 Conclusion 36

The photodoping effect on intra- and inter-layer exciton emission in $MoSe_2/MoS_2$ heterostructure is presented in this chapter. We demonstrate that the intensity of the inter-layer exciton PL emission is decreased under laser illumination. The simultaneous change of the neutral and charged exciton emission indicates the increased doping level. The increased intensity of intra-layer exciton emission and decreased intensity of inter-layer exciton suggests that the photodoping reduces the inter-layer charge transfer efficiency. This phenomenon is persistent at low temperature and under vacuum unless the sample is exposed to air, which indicates this photodoping is related to the physically absorbed water and oxygen molecules on the surface. The results provide a concise method to modulate the inter-layer charge transfer efficiency. The content of this chapter has been partially published in Nan Zhang et al. *Appl. Phys.* ***113****, 062107 (2018).*

3.1 Introduction

In monolayer transition metal dichalcogenides, it has been reported that the excitonic transition can be manipulated optically. In $MoSe_2$ and MoS_2 monolayers, which are intrinsically n-doped, an excess electron can be bound to a neutral exciton to form a three-particle complex commonly referred to as a charged exciton or trion. The emission of the trion occurs on the low energy side of the exciton emission with a typical energy difference of tens of meV. The energy difference between the exciton and trion emission corresponds to the binding energy of the trion. It has been demonstrated that the carrier density of a TMDC monolayer can be

tuned under ambient conditions (*i.e* in air at room temperature) via the physisorption of H_2O and O_2 molecules. The physisorbed H_2O and O_2 molecules induce a charge transfer with TMDC monolayers, the electrons are transferred from TMDC monolayers to the H_2O and O_2 molecules on the surface. [Tongay 2013a] utilized molecular physisorption as a gate to manipulate the exciton emission intensity. The PL intensity of neutral excitons in MoS_2 can be increased and decreased by purging and pumping with H_2O and/or O_2, respectively. However, WSe_2 which is intrinsically p type, shows the opposite effect. Purging with H_2O and/or O_2 leads to a decrease of exciton intensity. The inverse phenomenon observed in WSe_2 further confirms that the physisorption of H_2O and/or O_2 depletes the electrons.

On the other hand, laser illumination has been shown to change the carrier density, and therefore the optical properties, in monolayer TMDC. It has been reported that the trion to neutral exciton PL intensity ratio can be persistently tuned by laser illumination power or time on different kinds of monolayers. There are different microscopic processes to explain the reason why the laser illumination changes the carrier density. [Cadiz 2016a] show this effect depends on the kind of substrates, so the origin of this effect probably resides in the optical ionization of impurities in the substrate. [Currie 2015] show that laser illumination can increase the PL intensity of the trion in WS_2 and this process is reversible under ambient conditions. However, the effect is persistent if the sample is under vacuum or in an inert atmosphere *e.g.* nitrogen or helium. The reason is that the laser illumination removes the physisorbed H_2O and/or O_2 molecules and increases the electron density.

3.2 Micro-PL properties of $MoSe_2/MoS_2/MoSe_2$ heterostructure

We have investigated this laser illumination induced doping effect in a $MoSe_2/MoS_2/MoSe_2$ heterostructure prepared by a wet transfer method from chemical vapor deposition (CVD)-grown monolayers, which is presented in Fig. 3.1(a). The PL spectrum shown in in Fig. 3.1(c) consists of well-resolved peaks at 1.67 eV and 1.64 eV, identified with the neutral and charged exciton of MoSe2, respectively. The peak at 1.95 eV is assigned to the recombination of the A-exciton of MoS_2. As shown in Fig. 3.1(c), the charge transfer is efficient in $MoSe_2/MoS_2$ heterostructure due to the type II band alignment, which favours the formation of inter-layer excitons [Baranowski 2017b]. The prominent low energy peak at 1.4 eV is attributed to the inter-layer exciton. The assignment of the excitonic transitions is confirmed by the reflectivity contrast spectrum in Fig. 3.1(c), which exhibits the characteristic absorption of the A and B excitons of MoS_2 and $MoSe_2$, respectively.

3.3 Photodoping on intra-layer exciton of $MoSe_2$

For this investigation the sample was mounted in a He-flow cryostat and all the measurements were performed at $T = 5$ K under vacuum. We started by investigat-

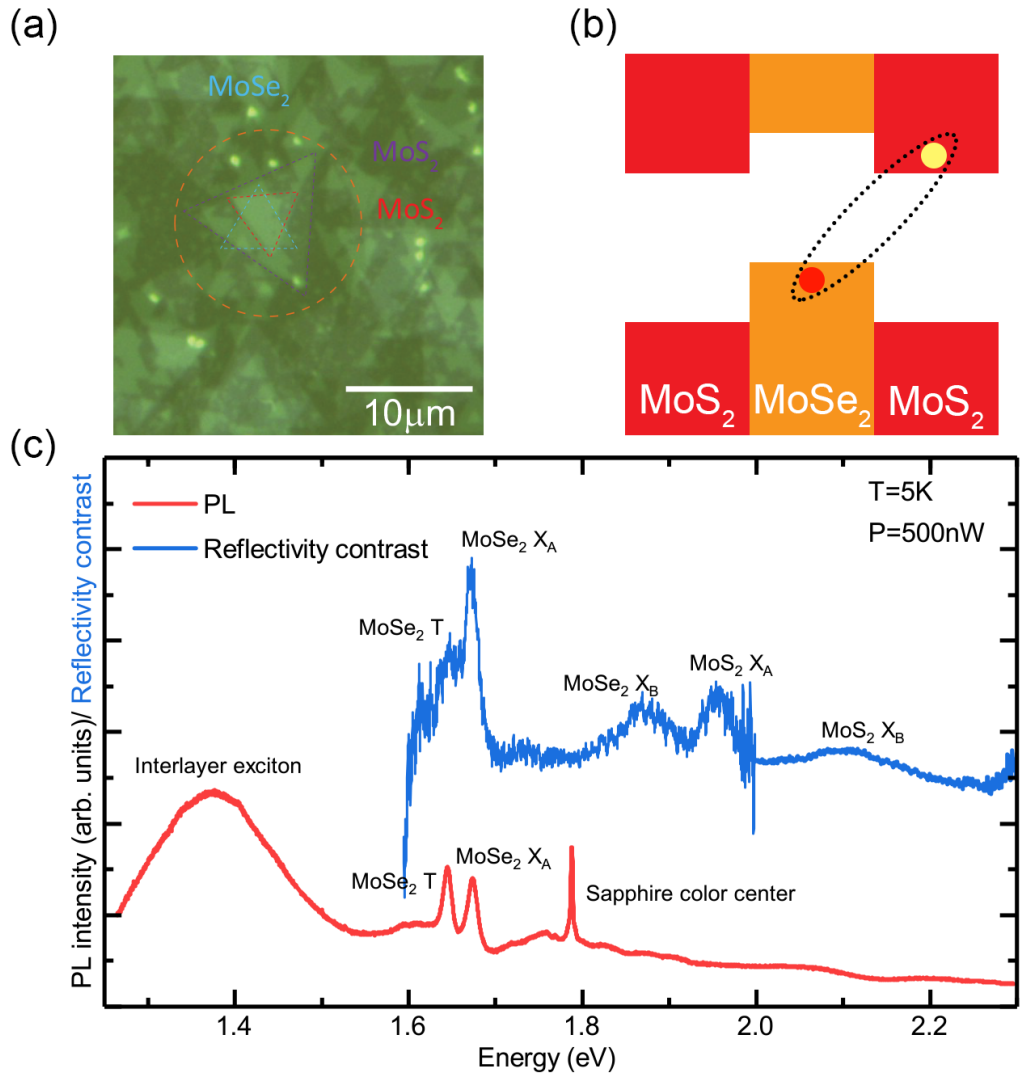

Figure 3.1: (a) Micrograph of one of the investigated $MoSe_2/MoS_2/MoSe_2$ heterostructure. (b) Schematic illustration of the band-alignment, charge transfer and inter-layer exciton in $MoSe_2/MoS_2/MoSe_2$ heterostructure. (c) Micro-PL spectrum (red) and reflectivity contrast spectrum (blue) of $MoSe_2/MoS_2/MoSe_2$ heterostructure measured at low excitation power and low temperature.

ing the influence of prolonged CW laser illumination (50 μW power). We acquired PL spectra from the sample at regular time intervals, the first spectrum was taken immediately after the sample was exposed to the laser. Typical PL spectra measured at a function of laser exposure time are presented in Fig. 3.2(a). Three main peaks can be resolved in the PL spectra, which are attributed to the emission of the trion (T), the neutral exciton (X) of $MoSe_2$, and the inter-layer exciton (I_X) formed across the $MoSe_2/MoS_2$ heterostructure. The sharp peaks observed on the low energy side of the $MoSe_2$ trion are probably related to the defect bound excitons

[Srivastava 2015a]. We have extracted the intensity and energy of the neutral and trion peaks over time by fitting with two Gaussian functions as shown in Fig. 3.3. The quantified details are summarized in Fig. 3.2. Over twenty minutes of laser illumination, the energy difference between neutral and charged exciton emission increases linearly. The fingerprint of the light induced change in the carrier density is the temporal evolution of the trion dissociation energy, defined as the energy difference between the exciton and trion emission. This quantity is the sum of the trion binding energy E_B^T (in the absence of other electrons) and the Fermi energy E_F measured from the bottom of the conduction band, $E_X - E_T = E_B^T + E_F$ [Huard 2000]. The linear increase of the trion dissociation energy with time, shown in Fig. 3.2(b), reflects the upwards shift of the Fermi level, as the carrier density increases with time.

With increasing laser exposure time, the intensity of the trion emission increases by around 50%, while the intensity of the neutral exciton emission remains more or less unchanged, as illustrated in Fig. 3.2(c). In contrast, the intensity of the inter-layer exciton emission drops by a factor of four, as shown in Fig. 3.4(a). The gradual increase in the relative intensity of the trion with respect to the exciton, displayed in Fig. 3.4(d), points to the gradual enhancement of the free carrier concentration, due to photo-doping, which increases the probability to form trions. As $MoSe_2$ and MoS_2 are intrinsically n-doped [Lu 2014], the observed monotonous increase in the trion intensity over time suggests that the photo-created free carriers are electrons.

In a heterostructure with a type II band alignment, the observation of negatively charged exciton emission from $MoSe_2$ can be counter-intuitive because, in the steady state, all electrons are expected to relax to the MoS_2 layer. Our observations suggest that the free carriers and excitons are photoexcited simultaneously. The short radiative lifetime of intra-layer excitons in TMDC [Lagarde 2014b], together with rapid trion formation [Singh 2016], allow a significant proportion of the trions to recombine before the charge transfer. The presence of free electrons in $MoSe_2$ is related to the photoionization of donors present in this material, similarly to WS_2 [Mitioglu 2013].

3.4 Photodoping on interlayer exciton

In Fig. 3.1(a), one can see that the intensity of inter-layer exciton drops by a factor of four during the photodoping process. We plot the combined integrated intensity of the charged and neutral excitons (X+T) as a function of the time in Fig. 3.1(e). In contrast to isolated monolayers [Currie 2015], the emission intensity of intra-layer excitonic species increases with increasing doping. This is consistent with a reduced charge transfer rate with increasing doping level, which also accounts for the decrease of the inter-layer exciton emission intensity with increasing doping. This effect might be exploited to optically control the efficiency of the inter-layer charge transfer by tuning the doping level in TMDC-based van der Waals heterostructures. The relative weight of the intra-layer to inter-layer emission intensity can also be

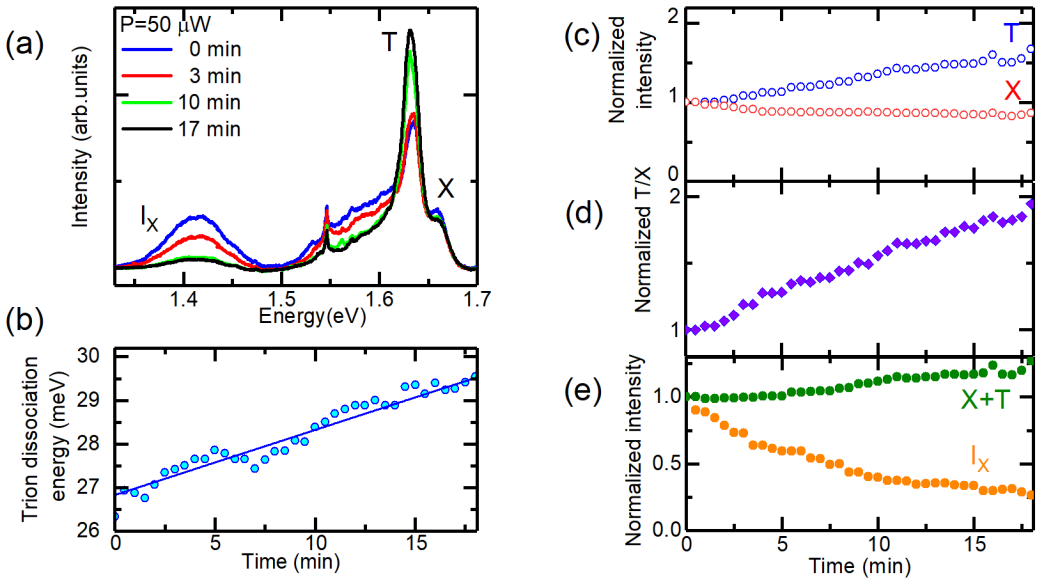

Figure 3.2: (a) Low temperature PL spectra acquired after the indicated laser exposure times showing charged (T) and neutral (X) exciton emissions from $MoSe_2$, together with emission of the inter-layer exciton (I_X). (b) Temporal evolution of the trion dissociation energy (the continuous line is a linear fit). (c) Temporal evolution of the integrated PL intensity of the charged and neutral excitons. (d) Temporal evolution of the intensity ratio of the neutral and charged excitons. (e) Temporal evolution of the combined integrated intensity of exciton (X + T) and integrated intensity of the inter-layer exciton.

controlled electrostatically, as previously demonstrated in a p-n junction consisting of a TMDC heterobilayer [Ross 2017].

We tentatively ascribe the decreasing charge transfer efficiency to the creation of a built-in electric field. This scenario is also consistent with the observed blue shift of the PL peak energy of the inter-layer exciton measured at high excitation power ($P = 200\,\mu$W). A comparison of the PL spectrum of the inter-layer exciton at the beginning and at the end of the exposure to the laser light is shown in Fig. 3.4(a), where a 6 meV blue shift is highlighted. The global temporal dependence of the energy of the inter-layer exciton transition, determined using the center of mass approach [Aivazian 2015a], which yields results equivalent to Gaussian fitting, is illustrated in Fig. 3.4(b). This trend is similar to the observed blue shift of the indirect exciton transition in type II quantum wells with increasing excitation power [Zaitsev 2007], which results from the large electric fields generated at high carrier concentrations. It is also in agreement with the recently observed drop of the emission intensity of the inter-layer excitons in gated heterostructures both for n- and p-type doping [Ciarrocchi 2019].

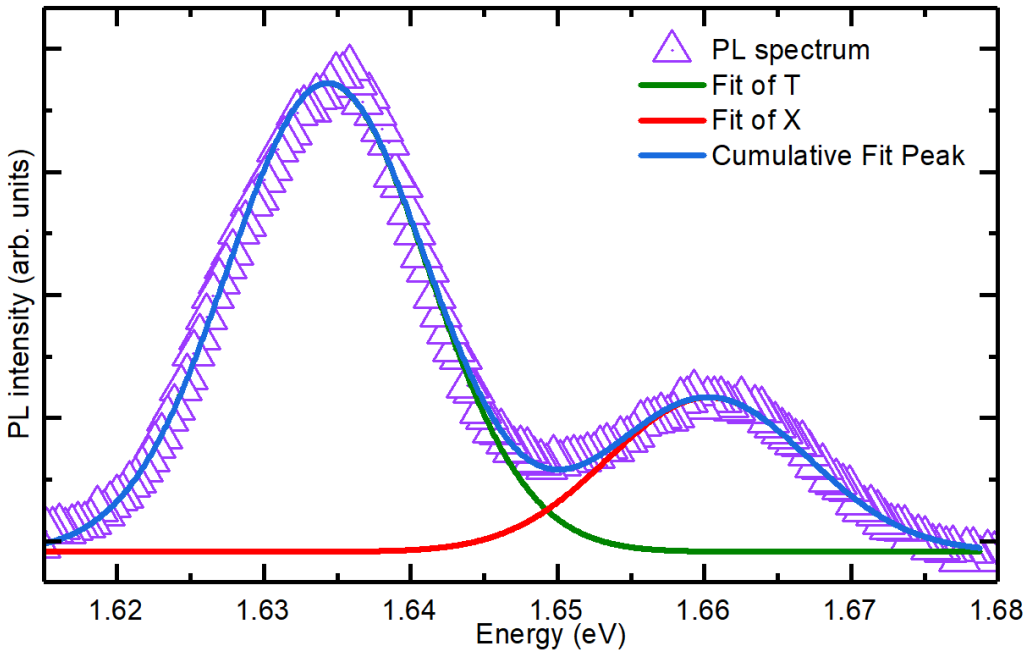

Figure 3.3: A representative example of fitting the exciton and trion PL emission of $MoSe_2$ using two Gaussian functions.

3.5 Photodoping microscopic mechanism

Several mechanisms, such as light induced vacancy creation, ionization of intrinsic donors, or charges trapped by the substrate, are considered to be responsible for photodoping in TMDC. Moverover, CVD grown TMDC are known to host a large concentration of chalcogen vacancies, which act as donors. In our heterostructures, the Se vacancies in $MoSe_2$ are partially filled by a defect-healing transfer of S atoms from MoS_2 [Surrente 2017]. However, the unsaturated vacancies might supply free electrons upon illumination, which leads to the observed photodoping. It is important to note that the observed changes in the sample are persistent, suggesting that prolonged exposure to laser light increases the number of photoionization centers.

The relative intensity between the neutral and charged excitons does not change even after hours in dark, provided that the sample is kept under vacuum. However, the trion-to- exciton intensity ratio observed before exposure to laser light is recovered after the sample is exposed to air at room temperature. This can be explained considering the physisorption of H_2O and O_2 molecules to TMDC. These two species bind to the chalcogen vacancies with a binding energy of $\simeq 100\,\text{meV}$ and deplete the naturally n-doped TMDC of electrons [Tongay 2013b]. Upon laser illumination, photogenerated holes neutralize the adsorbed species, leading to their photodesorption [Zhang 2013]. This explains the gradual increase in the free carrier concentration, which leads to the behavior summarized above.

Pulsed excitation has been reported to have a dramatic impact on the PL of

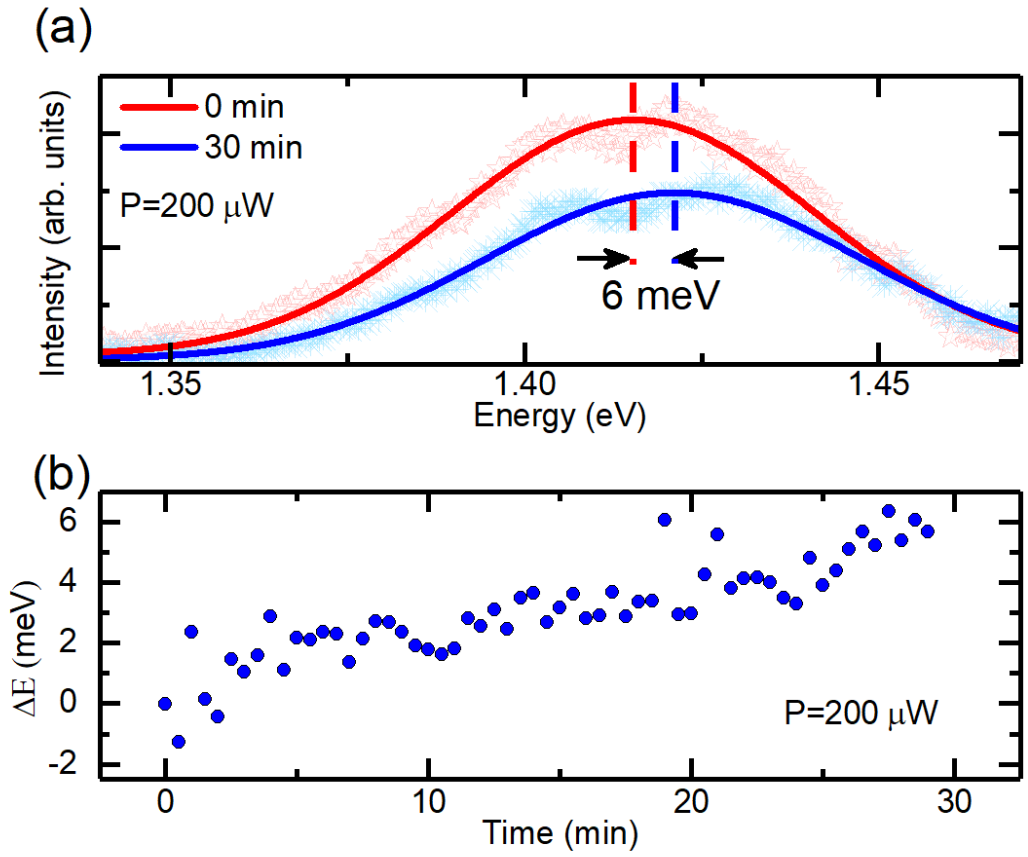

Figure 3.4: (a) PL spectra of the inter-layer exciton at the beginning and end of the exposure to a high power laser. (b) Temporal evolution of the energy of the inter-layer exciton PL at high excitation power.

intra-layer excitons, with a rapid and complete suppression of the intra-layer exciton emission accompanied by a radical modification of the line shape. To investigate the effects of different excitation conditions on the intensity of the inter-layer exciton emission, we monitored the temporal evolution of the PL exciting at 25 and 200 μW average power, using both CW and pulsed lasers. In Fig. 3.5, we show the temporal evolution of the PL intensity of the inter-layer exciton. While its intensity drops only marginally when we excite with a CW laser at 25 μW, the effects of a high excitation power are more prominent with an observed decrease of roughly 50% after $\simeq$ 30 minutes. In contrast, pulsed excitation suppresses the PL of the inter-layer exciton much more efficiently. For pulsed excitation an average power of 200 μW quenches almost completely the inter-layer exciton emission after an exposure of $\simeq$ 30 minutes. The peak power of the pulsed laser ($\simeq$ 830 W for 200 μW average power) creates a large density of carriers, which leads to a more efficient photodesorption [Lee 2016] of the physisorbed gas molecules.

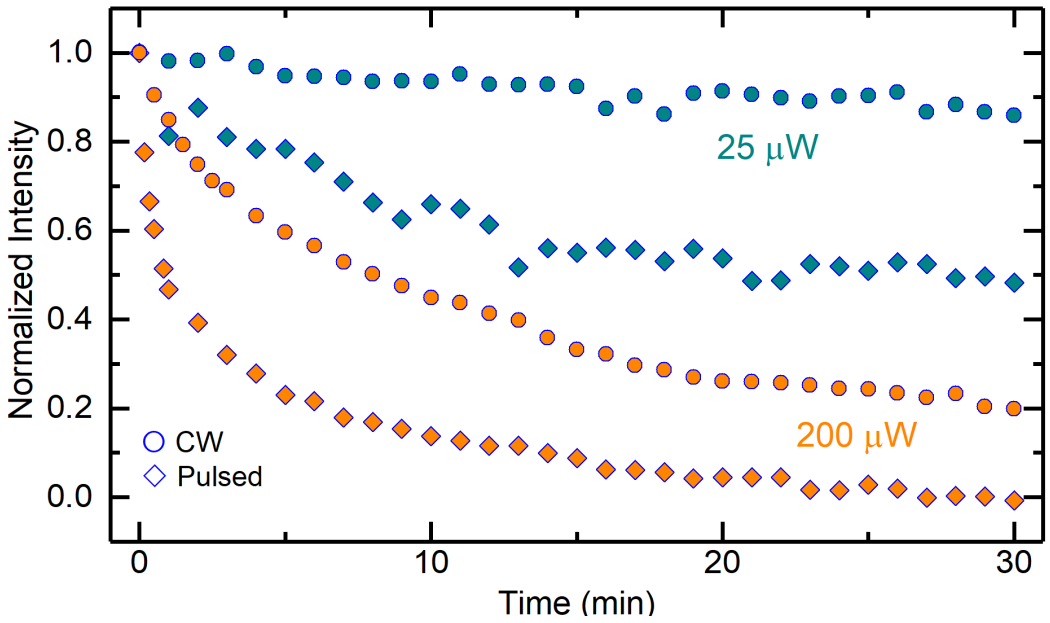

Figure 3.5: Temporal evolution of the PL intensity of the inter-layer exciton at different excitation powers under both CW and pulsed excitation.

3.6 Conclusion

In conclusion, we have investigated the effects of persistent photodoping on the exciton emission in a $MoS_2/MoSe_2/MoS_2$ heterostructure. Prolonged exposure to laser light increases the number of photoionization centers present, persistently increasing the photodoping effect (number of dynamically photoionized electrons in the conduction band), provided that the sample is kept under vacuum. This suggests that the effect is linked with laser induced desorption of water or oxygen molecules from the surface. The impact of the free carriers concentration on the interlayer emission might represent a possible step towards the control of the charge transfer rate in van der Waals heterostructures. If a more stable electrostatic environment is desired, doping following laser illumination can be prevented by encapsulating the van der Waals heterostructure in hBN [Courtade 2018].

Chapter 4

Moiré excitons

Contents

4.1 Introduction: intra- and inter-layer moiré excitons 37
4.2 Determination of the stacking angle in MoS_2/MoS_2 heterostructures 40
4.3 Fingerprints of intra-layer moiré Excitons 44
4.3.1 Moiré Excitons in $MoSe_2$ 44
4.3.2 Moiré Excitons in MoS_2 47
4.4 Properties of moiré excitons 47
4.4.1 Temperature dependence of the moiré exciton PL 48
4.4.2 PL dynamics of moiré excitons 49
4.4.3 Valley polarization of moiré excitons 51
4.5 Conclusions 52

-In this chapter, we discuss the results of the optical investigation of the $MoSe_2/MoS_2$ heterostructures with different twist angle. The twist angle was predetermined during the stacking procedure and subsequently confirmed using polarization resolved measurements of the second harmonic generation. We observed that for heterostructures with almost zero degree twist angle, the $MoSe_2$ excitonic emission and absorption is accompanied by side peaks on the high energy side of the spectrum. This is the first experimental observation of moiré intralayer excitons in an atomically thin TMDC.

4.1 Introduction: intra- and inter-layer moiré excitons

Th formation of a moiré pattern in TMDC stacks has been confirmed first using scanning tunneling microscopy [Zhang 2017, Pan 2018]. Theoretical calculations of the excitonic properties in a moiré potential suggested a splitting of the inter-layer exciton emission into two counter polarized emission peaks [Yu 2017]. This first principles calculation performed for MoS_2/WSe_2 heterostructures demonstrated two local minima for inter-layer excitons, as presented in the calculated potential landscape presented in the bottom panel of Fig. 4.1 (a). Further calculations of the oscillator strength demonstrated opposite helicity of the emission for the inter-layer excitons as shown in the color map in Fig 4.1 (a). Indeed in the first results obtained on different heterostructures, the inter-layer exciton was either counter polarized to the

excitation polarization[Baranowski 2017b, Surrente 2018] or two inter-layer excitons with opposite circular polarization were observed [Hanbicki 2018, Ciarrocchi 2018] which have been attributed to the effects of the moiré pattern at the time.

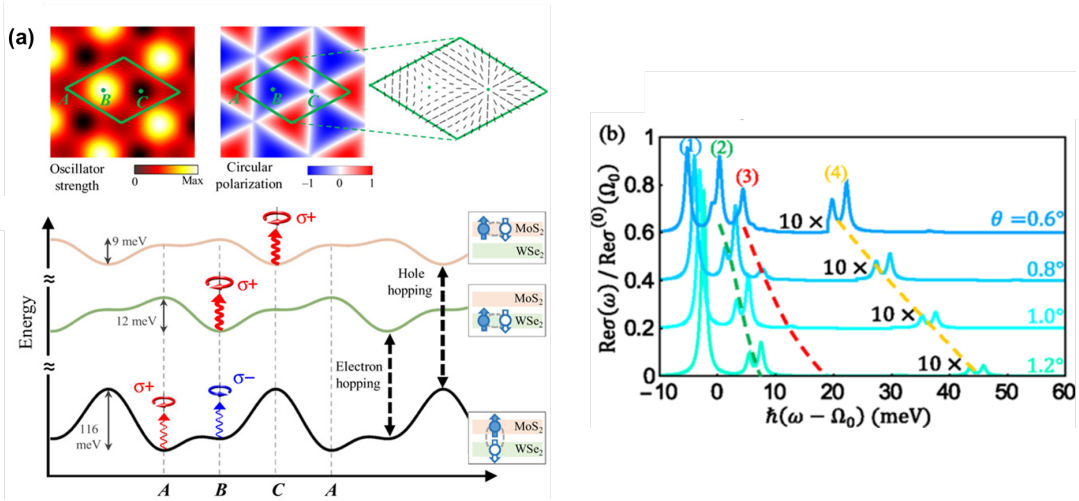

Figure 4.1: (a) The top left panel shows the oscillator strength of the interlayer exciton. The top right panel shows the optical selection rule for the spin-up inter-layer exciton (in the K valley). The bottom panel shows the contrasted potential landscapes for the intra- and inter-layer excitons, with the optical selection rule for the spin-up species shown at the energy minima. After [Yu 2017] (b) Optical conductivity of moiré excitons for several different twist angles. After[Wu 2017a]

Interestingly, in the theoretical work of Yu and co-authors, the intra-layer excitons in a moiré potential were also considered. In contrast to inter-layer excitons, the influence of a moiré pattern is much smaller for intra-layer excitons since the depth of the potential is of the order of only a few meV, as shown in the bottom panel of Fig. 4.1 (a) [Yu 2017]. Further theoretical calculations of the intra-layer excitons in a moiré potential have been performed by Wu and co-authors [Wu 2017a]. In these calculations, the absorption spectrum of intra-layer excitons in different van der Waals stacks were calculated for various different stacking angles. An example of these results is shown in Fig4.1, where a characteristic finger print of the impact the moiré pattern on the intra-layer exciton is observed on the high energy side of the excitonic absorption as serious of satellite peaks.

Recently, more studies concerning moiré excitons and their properties have been published. Choi and co-auhors' work reveals that the moiré potential in van der Waals heterostrutures impedes the diffusion of inter-layer exciton. The spatially- and spectrally resolved PL shows that there is no inter-layer exciton diffusion observed in a sample with a period of the moiré potential of 20 nm, while the inter-layer exciton diffusion with 1 μm diffusion length can be observed in samples with a period of the moiré potential of 5.7 nm [Choi 2019]. The moiré inter-layer exciton has been shown to have a quantum nature via the observation of photon anti-bunching.

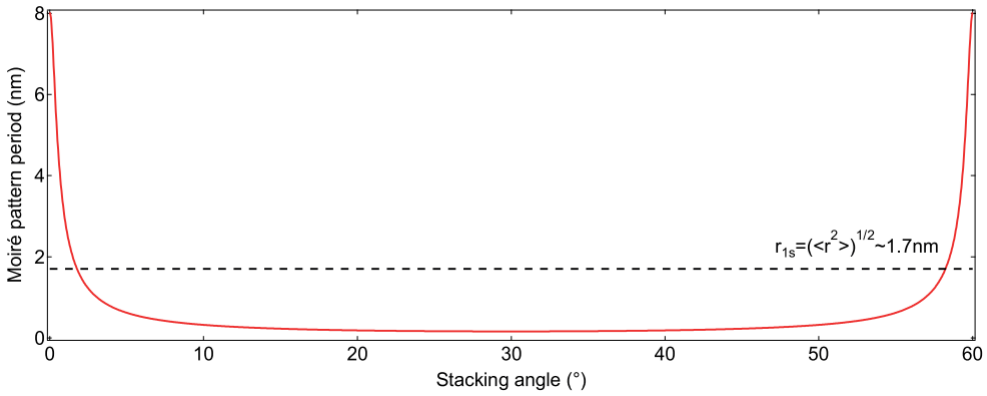

Figure 4.2: Period of the potential of the moiré pattern in a $MoS_2/MoSe_2$ heterostructure as a function of the stacking angle. The dashed lines corresponds to the exciton radius in a WSe_2 monolayer encapsulated in hBN extracted via high magnetic field measurements [Stier 2018]

The quantum emitter can be tuned up to 40 meV via the dc Stark effect due to the electron-hole pair separation in the heterostructure [Baek 2020]. First-principles MBPT results shows that the quasi-particle energy and inter-layer exciton energy vary by up to 100 meV between different local sites of the moiré potential, and the dipole oscillator strength and radiative lifetime of inter-layer excitons are modified by the local stacking styles by up to a few orders of magnitude [Lu 2019]. In the case of small twist angles ($\leq 1°$), conductive atomic force microscopy (CAFM) results show that the atomic reconstruction significantly modifies the rigid-lattice of the moiré pattern. This atomic reconstruction produces large commensurate domains and has significant implications for the electronic and optical properties of TMDC vdW heterostructures. [Rosenberger 2020].

The theoretical calculation suggest that the most pronounced impact of a moiré pattern should be observed for small twist angles between the layer forming heterostructure. A ball park explanation of this is that the period of the moiré potential has to be larger than the exciton radius if the exciton is to feel the modulation of potential. In other words the motion of the exciton center of mass occurs in a slowly varying potential, which locally modulates the band gap. In case of a short period moiré pattern, the exciton experience spatially averaged potential in analogy to conduction band electrons in crystal which behave as a free particles despite the periodic potential of the crystal lattice. To determine the relevant twist angel range we compare the exciton radius of intra-layer exciton ($r \simeq 1.7\,\text{nm}$) [ref] with the period of the moiré potential which in case of two twisted hexagonal lattices (with different lattice parameter) is described by following formula,

$$\Lambda = \frac{a_{MoS_2} a_{MoSe_2}}{\sqrt{a_{MoS_2}^2 + a_{MoSe_2}^2 - 2a_{MoS_2} a_{MoSe_2} \cos 3\theta}}, \tag{4.1}$$

where a_{MoS_2} (a_{MoSe_2}) is the lattice parameter of MoS_2 ($MoSe_2$), and θ is the

rotation angle [ref]. Fig. 4.2 shows the resulting period of moiré superlattice versus θ. It can be seen that θ has to be in the range of a single degree to provide a Λ significantly larger than exciton radius.

4.2 Determination of the stacking angle in MoS_2/MoS_2 heterostructures

The expected potential fluctuations are in the range of a few meV to a few tens of meV for intra- and inter-layer exciton (see Fig. 4.1)[Wu 2017a, Yu 2017]. Therefore, to observe excitons confined in different regions of the moiré potential, a sample with high optical quality, together with a precise control of the stacking angle θ is essential. To observe moiré intralayer excitons we have used high quality $MoS2_2/MoS_2$ heterostructures fully encapsulated in hexagonal boron nitride. The samples were prepared in the group of Professor Andres Castellano-Gomez in Madrid. A detailed description of the samples preparation procedure is provided in chapter 2.6.

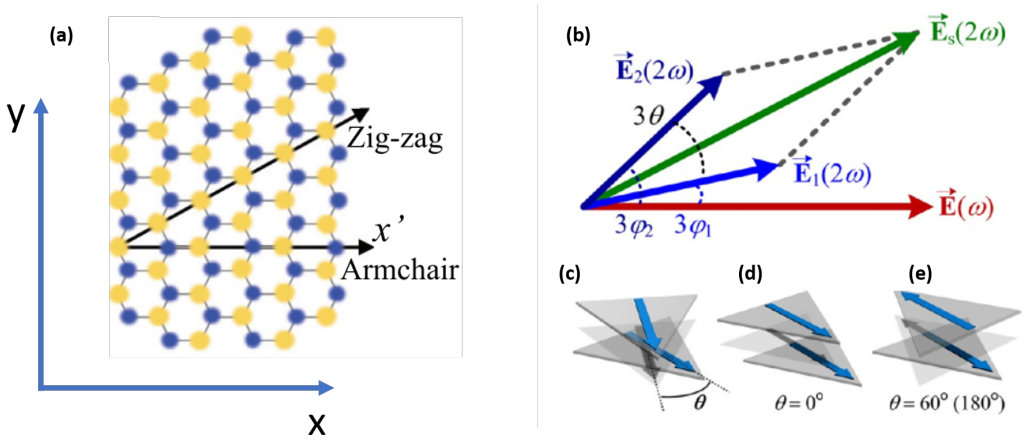

Figure 4.3: (a) Schematic showing the Zig-zag and Armchair directions in a TMDC monolayer, (b) A schematic illustration of electric field superposition in second harmonic generation (SHG) process, where $\vec{E}(\omega)$ is the electric field of incident light, $\vec{E}_1(2\omega)$ [$\vec{E}_2(2\omega)$] are SHG electric field generated in flake 1 (flake 2), and $\vec{E}_s(2\omega)$ is resulting SHG field from 2 TMDC stack. (c)-(e) Schematics for stacked bi layers with (b) an arbitrary stacking angle, 0° and 60°[Hsu 2014]

The investigated series consist of three structures with nominal twist angle close to 0, 20 and 60 degrees. The effect of the moiré potential is expected to be visible for only the first and last structure. The heterostructure with a 20 degree twist served as a additional reference, since for such an angle the coupling between the layers should vanish suppressing the moiré potential. In order to confirm the desired twist angle between layers we performed measurements of polarization resolved second harmonic generation (SHG) together with a spatial mapping of the SHG

efficiency. Second harmonic spectroscopy is very useful technique to gain information concerning the alignment of monolayers in van der Waals heterostructures. As previously discussed, monolayer transition metal dichalcogenides lack inversion symmetry, which is responsible for the specific selection rules. In addition, the lack of inversion symmetry gives rise to efficient SHG generation. The structure of monolayer TMDC is schematically shown in Fig. 4.3, where yellow circles are S or Se atoms, and blue circles indicate the plane of Mo or We atoms located between the two chalcogen atoms planes. Monolayers of TMDC have D_{3h} symmetry, and the nonzero elements of the second-order nonlinear susceptibility tensor are $\chi^{(2)}_{y'y'y'} = -\chi^{(2)}_{y'x'x'} = -\chi^{(2)}_{x'x'y'} = -\chi^{(2)}_{x'y'x'}$ where x' and y' are in plane crystalline coordinates, and, x' is defined as being along the armchair direction, which is 30° from the zigzag direction (see Fig. 4.3. Since TMDC have threefold rotational symmetry the x and y component of the generated second harmonic electric field are proportional to $\sin 3\alpha$ and $\cos 3\alpha$, respectively, where α is angle between electric field vector of incident light and armchair direction. Consequently, the intensity of the x and y components of the second harmonic signal depends as $\sin^2 3\alpha$ and $\cos^2 3\alpha$, however, the total intensity is independent of the direction of the polarization of the incident light. In TMDC stacks the situation is slightly more complicated since the SHG from the two overlaid layers is a coherent superposition of the second harmonic fields from the individual layers [Hsu 2014], with a phase difference depending on the twist angle. Therefore, the total second harmonic intensity depends on the relative twist of layers (θ). It can be shown that,

$$I_{SH} = I_1 + I_2 + 2\sqrt{I_1 I_2}\cos 3\theta. \tag{4.2}$$

As we can see for the particular case of natural bilayers, where the individual layers are twisted by 60° (Bernal stacking) the second harmonic signal vanish completely. This can be also understand as the effect of restored inversion symmetry.

Therefore, using the properties of SHG in TMDC, the relative orientation of layers in a stack can be precisely determined. The polarization resolved SHG signal taken from non overlapping (monolayer) regions of the sample provides information about the layer orientation up to ±60° (due to threefold symmetry), while the decrease or increase of signal in the heterostructure region provide useful information if the twist angle is close 0 or 60 degree (in a heterostructure, even in case of $\theta = 60\circ$ the signal does not vanish completely due to the different efficiency of SHG in the different layers).

Fig. 4.4 (a) shows the result of the SHG mapping. Unfortunately, since the entire MoS_2 flake is covered by the larger $MoSe_2$ monolayer, we were unable to access separately the second harmonic signal of MoS_2. Nevertheless, from the spatial dependence of the second harmonic signal we can see that in the area corresponding to the heterostructure, the second harmonic signal is with strongly enhanced with respect to the the isolated regions of $MoSe_2$. This constructive interference between the second harmonic signals coming from both monolayers is a strong indication that stacking angle is close to 0 degrees consistent with our observation based on the alignment of the straight edges of the exfoliated flakes. Further evidence to support

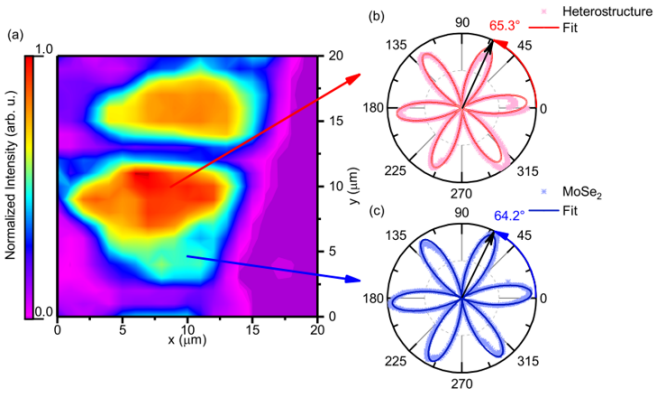

Figure 4.4: (a) Map of the second harmonic signal measured on the heterostructure device with nominal stacking angle $\simeq 0$ degrees presented in the main text. Polarization resolved second harmonic measured on (b) isolated $MoSe_2$ and (c) on the heterostructure.

this is provided by polarization resolved measurements of the second harmonic signal. The threefold symmetry of the crystals is reflected in the sixfold symmetry of the polar plot of one of the two perpendicular components of second harmonic signal observed in the heterostructure (panel (b)) and MoSe2 (panel(c)) regions. Fitting to the polar plots using $I \propto cos(3\theta)$ allows us to conclude that relative orientation of polar plots differ only by $1.1 \pm 2.0°$ which further confirms that twist between layers is close to 0°.

An optical microscope image of the second structure, which was intentionally fabricated with a twist angle of $\simeq 20$ between the layers, is presented in Fig. 4.5 (a). For this sample it was possible to collect the SHG signal from both layers independently. The polarization resolved intensity versus polar coordinate is presented in panel (b). Fitting to the SHG polar dependence we find that the two layers are rotated $\sim 19pm2°$ confirming the desired alignment of layers.

An optical microscope image of the third structure is presented in Fig. 4.6 (a). Also for this sample it was possible to collect the second harmonic signal independently from the single layer MoS_2 and $MoSe_2$ regions. The polarization resolved results are presented in panel (b) of Fig. 4.6. Both data sets overlap almost perfectly indicating that the twist angle is close to 0° or 60°. These two orientation are indistinguishable from polarization resolved studies due to the sixfold symmetry of the polarization resolved signal. To distinguish between the two possible orientations we have performed a mapping of second harmonic signal presented in Fig. 4.6 (c). On the heterostructure region (indicated by thick dashed white line) the intensity of second harmonic signal is (as expected for a 60° rotation between the layers) reduced with respect to isolated layer region (marked by thin yellow dashed lines). Therefore, we can be conclude that the layers are indeed rotated by $\simeq 60°$

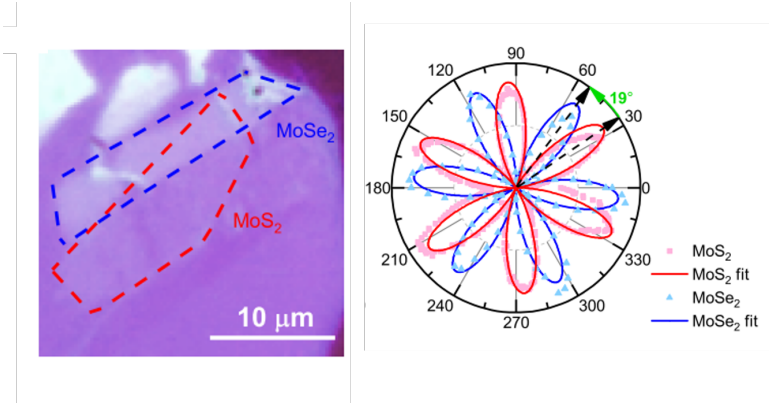

Figure 4.5: Optical microscope image of a hBN-encapsulated $MoS_2/MoSe_2$ heterostructure with $\simeq 20°$ stacking angle. Polarization resolved second harmonic measurement on the single layer regions of the same device.

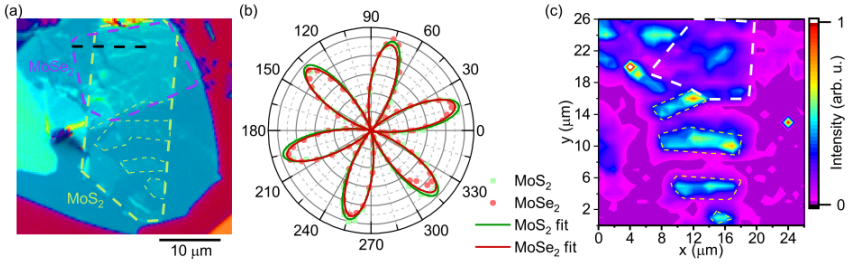

Figure 4.6: (a) Optical microscope image of a hBN-encapsulated $MoS_2/MoSe_2$ heterostructure with nominal 60° stacking angle. Isolated MoS_2 monolayers are framed by a thinner yellow lines and correspond to the yellow lines of panel (c). (b) Polarization resolved second harmonic measured on isolated areas of $MoSe_2$ and MoS_2. (c) Map of second harmonic generation. The area corresponding to the heterostructure is highlighted by a dashed white line. The dashed yellow lines frame the MoS_2 monolayers shown in panel (a).

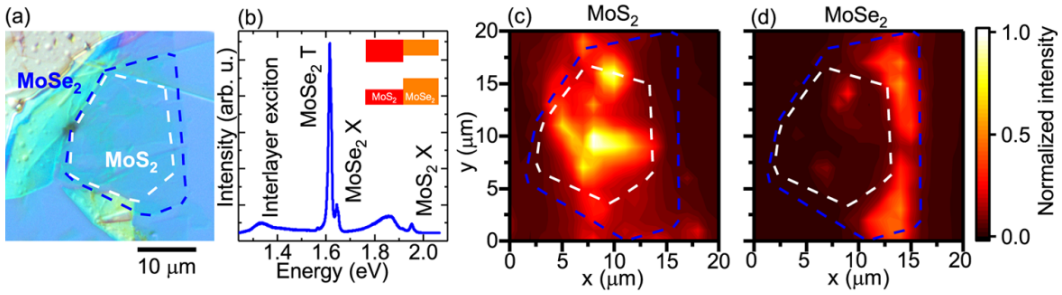

Figure 4.7: (a) Optical microscope image of the $MoS_2/MoSe_2$ heterostructure encapsulated in hBN. The blue and white dashed lines indicate the contours of the $MoSe_2$ and MoS_2 flakes. (b) PL spectrum of the heterostructure taken at $T = 5\,\mathrm{K}$. The inset shows the schematic band alignment of a $MoSe_2/MoS_2$ heterostructure. Normalized PL intensity maps of (c) MoS_2 and (d) $MoSe_2$.

4.3 Fingerprints of intra-layer moiré Excitons

Most of the data presented here have been obtained on the sample with near zero stacking angle. We have focused on the optical properties of the neutral and charge excitons in $MoSe_2$. We have also performed some measurements for the sample with 60 degrees stacking angle, and in addition, we have analyzed the emission spectra for MoS_2.

4.3.1 Moiré Excitons in $MoSe_2$

The typical data obtained on the sample with zero nominal stacking angle are presented in Fig. 4.7(a) where we show a micrograph of the fabricated heterostructure. It consists of a monolayer $MoSe_2$ flake, indicated by the blue dashed line, partially covered by a MoS_2 monolayer (white dashed lines). A representative PL spectrum of our heterostructure taken over a broad energy range at $T = 5\,\mathrm{K}$ is presented in Fig. 4.7(b). The peaks at 1.615 eV and 1.644 eV arise from the radiative recombination of the intra-layer trion and exciton of $MoSe_2$, respectively. The weaker PL peaks centered at 1.94 eV and 1.87 eV are assigned to the recombination of neutral excitons and to excitonic complexes bound to defects in MoS_2 [Surrente 2017, Cadiz 2017], respectively. The low energy peak at 1.37 eV stems from the inter-layer exciton emission, which originates following the charge transfer due to type II band alignment, as schematically shown in the inset of Fig. 4.7(b) [Baranowski 2017b, Surrente 2018]. Here, we focus on the properties of intra-layer excitons. PL intensity maps of intra-layer MoS_2 and $MoSe_2$ are presented in Fig. 4.7(c-d). The $MoSe_2$ PL intensity of Fig. 4.7(d) is suppressed in the heterostructure region, due to the inter-layer charge transfer [Ceballos 2014, Chen 2016]. The strongly modified optical properties in the heterostructure region are an indication of the good coupling between the layers, characteristic for $\simeq 0°$ stacking angle [Wang 2016b].

We focus on the emission and reflectivity spectra in the energy range corre-

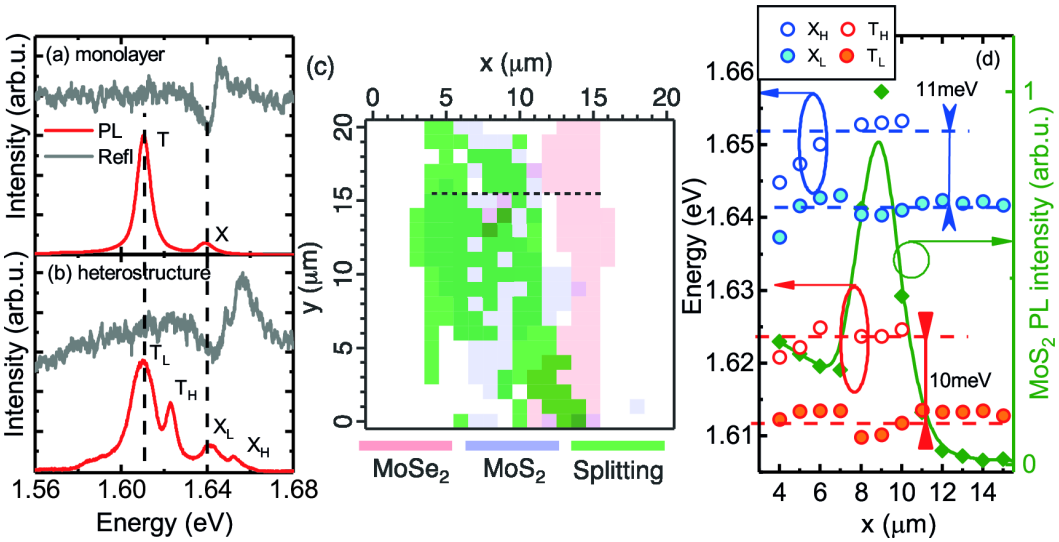

Figure 4.8: PL and reflectivity spectra of $MoSe_2$ measured in (a) monolayer and (b) heterostructure regions. (c) Spatial map showing the presence of a splitting of the $MoSe_2$ emission, overlaid with the areas of most intense PL of MoS_2 and $MoSe_2$. (d) Energy of the observed $MoSe_2$ transitions (blue and red dots) extracted along the horizontal dashed line of panel (c). Open circles correspond to high energy peaks observed only in the heterostructure, closed circles represent low energy transitions observed in all regions of the $MoSe_2$ flake. Green diamonds show the MoS_2 PL intensity.

sponding to the intra-layer excitons in $MoSe_2$. On a fully hBN-encaspulated $MoSe_2$ monolayer, the PL spectrum consists of two peaks, attributed to charged and neutral exciton (see Fig. 4.8(a)). In contrast, the $MoSe_2$ exciton and trion PL from the heterostructure region reveals a double peak structure, as shown in Fig. 4.8(b). We label these features X_L (T_L) and X_H (T_H), to refer to higher and lower energy transition of the exciton (trion). Importantly, the splitting of the exciton emission is also visible in the reflectivity spectrum of Fig. 4.8(b), unequivocally demonstrating that it is related to a free exciton transition rather than bound state emission. The presence of a double PL peak in the heterostructure region is consistent with the expected effect of the moiré pattern on the intralayer excitonic complexes. According to theoretical predictions, the stacking of two lattice mismatched TMDC monolayers induces a spatially periodic fluctuation of the potential felt by the excitons [Yu 2017, Zhang 2017, Wu 2018, Wu 2017a] with two local minima related to different atomic registries [Yu 2017]. The period of the moiré pattern is in the range of a few to tens of nanometers. Therefore, the spatial resolution of our far field optical measurements is insufficient to resolve the spatial variation of the emission energy of excitons located in different potential minima. Nevertheless, the emission from different optically active minima of the moiré pattern can be spectrally resolved in our high quality sample. The double structure of the exciton and trion

peaks is consistently observed in the heterostructure region, while it is completely absent in monolayer regions. This is summarized in Fig. 4.8(c), where the spatial map highlights the areas where the splitting is observed. To verify that the observed splitting is a direct consequence of the moiré pattern, we performed the same measurements on the $MoS_2/MoSe_2$ heterostructure with a stacking angle of $\sim 20°$. In this heterostructure, the period of the moiré pattern is significantly smaller than the spatial extension of the intra-layer exciton wavefunction and, as expected, we do not observe any splitting in the PL spectra of the $MoSe_2$ exciton or trion.

In Fig. 4.8(d), we show the spatial variation of the exciton and trion PL energy along the dashed line crossing the heterostructure in Fig. 4.8(c). The slice starts and ends at positions on the sample where PL is observed. A direct comparison of the spectrum measured in the heterostructure region with one measured outside (see Fig. 4.8(a,b)) reveals that the double structure results from the appearance of a new emision peak on the high energy side of the main exciton and trion emission. The energies of the emission lines observed in isolated monolayers are nearly identical to the X_L and T_L lines observed in the heterostructure, as highlighted by the vertical lines in Fig. 4.8(a,b). This is in agreement with the prediction that the exciton states related to the moiré pattern should appear as peaks on the high energy side of the main PL peaks [Yu 2017, Wu 2017a]. This observation, along with the fact that the double peak structure appears over a vast area in the heterostructure and not only at its edges [Raja 2017], allows us to rule out the variation of the dielectric screening related to the presence of the MoS_2 monolayer as the origin of the observed doublet structure. Since the dielectric constant of MoS_2 is higher than that of hBN [Laturia 2018], a dielectric screening effect would lead to the appearance of lower energy peaks when the excitation is performed on the heterostructure region [Raja 2017].

We can also exclude the presence of strain in the $MoSe_2$ layer in the heterostructure region by noting that the A_{1g} Raman mode of $MoSe_2$ occurs at the same energy as that of an isolated $MoSe_2$ monolayer. The observed energy scale of the splitting ($\sim$ 6–12 meV) is in agreement with the energy scale of potential variation predicted for our MoS_2/WSe_2 heterostructure [Yu 2017].

Moiré intralayer excitons are theoretically predicted also in the case of a heterobilayer with 60° stacking angle [Yu 2017]. Inspired by this theoretical prediction we have measured photoluminescence of MoS_2 on and outside the heterostructure region. In agreement with theoretical predictions, we observe systematically a splitting of the intra-layer PL emission, as shown in Fig. 4.9(a), throughout the heterostructure region. By performing a spatially resolved PL acquisition, we demonstrate that also in this sample the doublet in the PL spectrum of $MoSe_2$ is observed only whenever the $MoSe_2$ overlaps with the MoS_2 monolayer, as can be seen in Fig. 4.9(b). This additional result further corroborates our assignment of the double peak structure in the PL spectrum of $MoSe_2$ to the presence of a moiré pattern with a period larger than the spatial extent of the exciton wave function.

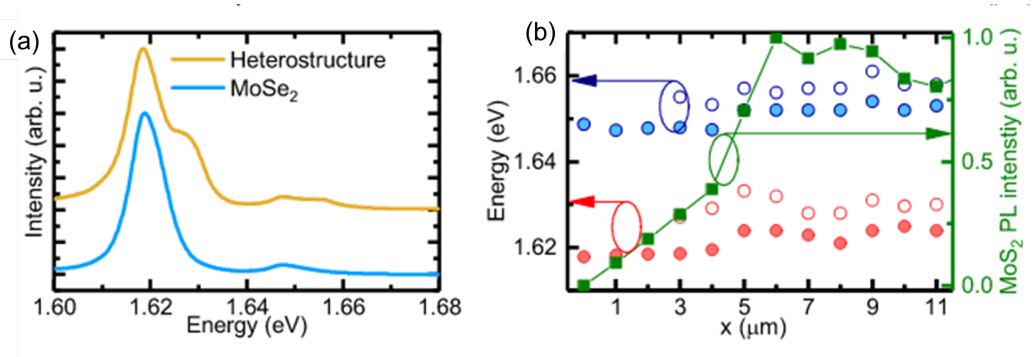

Figure 4.9: (a) PL spectrum of $MoSe_2$ measured in and out of the heterostructure region. (b) Energy of the observed $MoSe_2$ transitions (blue and red dots) extracted across the black dashed line of panel (a). Open circles correspond to high energy peaks observed only in the heterostructure region, closed circles represent low energy transitions observed over all the $MoSe_2$ flake. Green squares show MoS_2 PL intensity (indication of heterostructure region).

4.3.2 Moiré Excitons in MoS_2

Independently, we have measured the low temperature PL from MoS_2 layer in the heterostructure region. The results are presented in Fig. 4.10. We notice also in this case the presence of the splitting of the excitonic transitions induced by the moiré pattern, which amounts to $\simeq 11\,\text{meV}$, a similar value as for excitons in $MoSe_2$

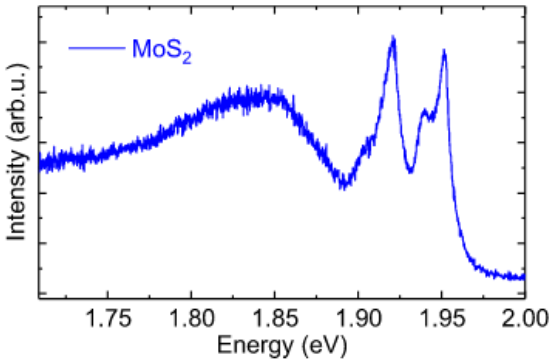

Figure 4.10: Low temperature μPL of MoS_2 showing the splitting of exciton and trion emission peaks.

4.4 Properties of moiré excitons

We have further investigated the properties of intra-layer moiré excitons to compare them with intra-layer excitons in a simple $MoSe_2$ monolayer. We have performed temperature dependent, time resolved and polarization resolved studies of photoluminescence of the moiré exciton and trion in $MoSe_2$.

Finally, we show in Fig. 4.11(a,b) detailed spatial maps of the splitting energy for the neutral and charged exciton of $MoSe_2$. The spatial uniformity of the energy of the fundamental excitonic transition is shown in the map of Fig. 4.11(c). Given the high spatial uniformity of the energy of the low energy exciton peak, the spatial variation of the energy of the high energy exciton peak can be inferred from the map of the energy splitting of Fig. 4.11(a).

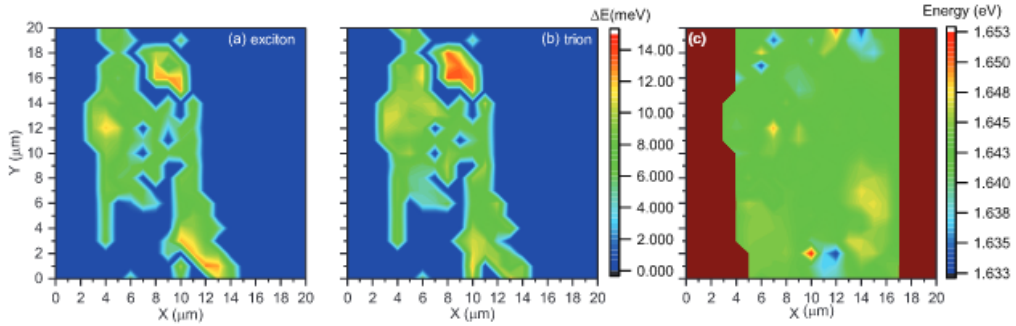

Figure 4.11: Spatial map of the splitting energy of the $MoSe_2$ (a) neutral and (b) charged exciton, and of (c) the energy of the fundamental excitonic transition.

4.4.1 Temperature dependence of the moiré exciton PL

In Fig. 4.12, we summarize the temperature dependence of the $MoSe_2$ PL measured on the heterostructure. As for all Mo-based TMDC, we observe a decrease of the PL intensity with increasing temperature [Zhang 2015]. We notice in particular a more rapid decrease of the intensity of the trion PL, which can be no longer resolved for temperatures above $\sim$ 100K [Surrente 2017], consistent with the smaller binding energy of this complex as compared to the exciton. Concerning the states split by the moiré potential, the intensity of the high energy peaks X_H and T_H decreases more rapidly than that of the low energy peaks. For temperatures higher than $\sim$ 90 K, corresponding to a thermal energy of $\sim$ 7.7 meV, the X_H and T_H features are no longer resolved. This is illustrated in the inset of Fig. 4.12, where we plot the ratio of the intensities of the high energy peaks I_H normalized by the intensities of the corresponding low energy peaks I_L. The faster quenching of the X_H and T_H emission further supports the moiré pattern as the origin of the trion and exciton doublet. A smaller confinement is expected for the higher energy states [Yu 2017], hence with increasing thermal energy these exciton can be detrapped more easily via thermally activated phonon scattering out of the moiré potential.

From the temperature dependence of the intensity of X_H, an activation energy can be estimated. We extracted the temperature dependence of the intensity of high energy peak of the $MoSe_2$ exciton $I_H(T)$, which we summarize in Fig. 4.13. To estimate the energy required to detrap this exciton, we fit an Arrhenius function to

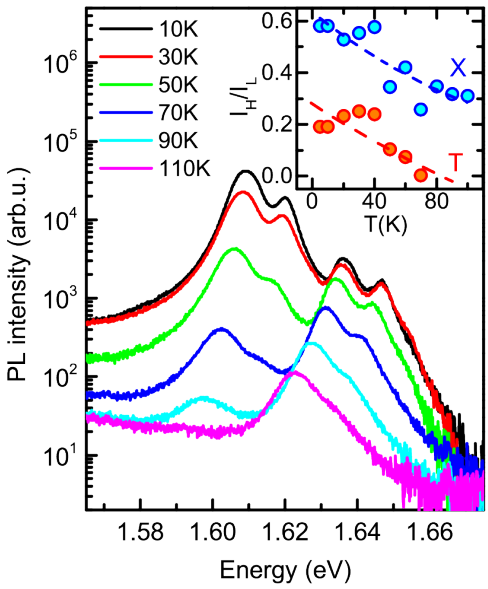

Figure 4.12: Temperature dependence of $MoSe_2$ PL. Inset shows the ratio of intensities of the high to low energy exciton and trion.

the experimental data,

$$\frac{I_{\mathrm{H}}(T)}{I_{\mathrm{H}}(T=0)} = \frac{1}{1 + a\exp(-E_{\mathrm{A}}/k_b T)},$$

where E_{A} represents the energy scale required for the activation from the high energy moiré state. Our fit yields $E_{\mathrm{A}} \sim 26\,\mathrm{meV}$. This value is comparable to the depth of the moiré potential for intralayer excitons of 12–19 meV, depending on the stacking of the heterobilayer [Yu 2017]. This behaviour is fully consistent with the observation of a more rapid thermal quenching of the PL of high energy moiré states observed in the inter-layer exciton [Tran 2018].

4.4.2 PL dynamics of moiré excitons

We have investigated the trion and exciton dynamics in $MoSe_2$. The spectrally resolved temporal evolution the PL measured in the heterostructure area is shown in Fig. 4.14(a). Similar data acquired on an isolated $MoSe_2$ monolayer is shown in Fig. 4.14(b). In the streak image of Fig. 4.14(c), the four PL peaks are well resolved, with the dynamics of the excitonic transition being significantly faster than those of the trions. To obtain more quantitative information, we extract the decay curves corresponding to $MoSe_2$ trion and exciton transitions in monolayer and heterostructure regions in Fig. 4.14(d,e), respectively. PL decays of all trion and exciton species can be fitted well using a single exponential, convoluted with a Gaussian curve to account for the instrument response function of the system.

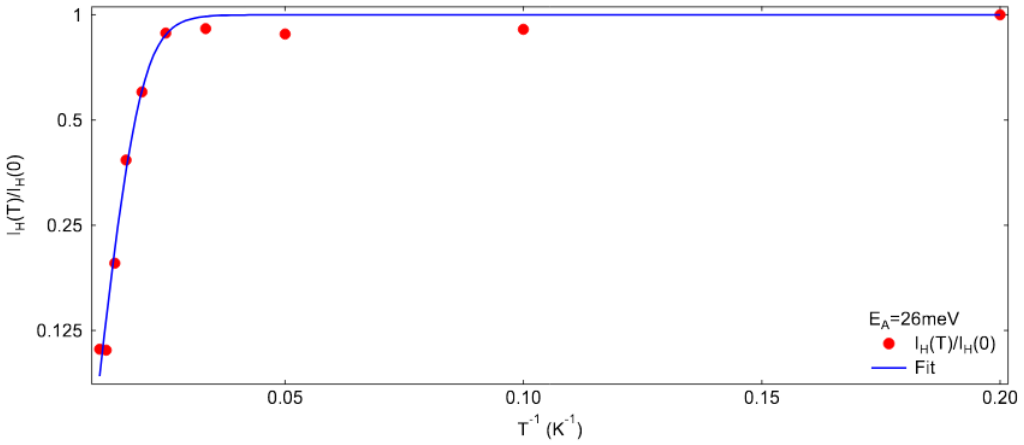

Figure 4.13: Circles: Temperature dependence of the PL intensity of the high energy peak of $MoSe_2$ exciton. The blue line represents the fit to the Arrhenius function described in the text.

From this fitting, we extract the PL life times. There are no significant differences between PL decay times in the monolayer and heterostructure areas or between X_H (T_H) and X_L (T_L) transitions. For the exciton transitions, the PL decay time is $\simeq 14$ ps, while for the trion it is $\simeq 70$ ps. We notice, however, that the PL decay time of the exciton is close to the resolution of our system, therefore the dynamics of the two exciton states might be slightly different. The faster decay of the high energy trion is consistent with the observation of the dynamics of high energy inter-layer exciton states in a moiré potential, where this behaviour has been attributed to the possible relaxation of high energy states to the low energy states [Tran 2018].

The overall similar decay times of the high and low energy transitions suggest that the moiré potential does not affect significantly the oscillator strength of the transitions. This can be understood as a result of the slow spatial variation of moiré potential (a few to tens of nm, depending on the stacking angle and the lattice mismatch of the heterobilayer) compared to the exciton size in TMDC monolayers ($\simeq 1$ nm) [Stier 2018, Stier 2016b]. Therefore, the wave function of intra-layer excitons is not significantly affected by the confinement induced by the moiré pattern. Interestingly, despite a clear drop of the PL intensity in the heterostructure area, the decay times of the trion and exciton PL are very similar to those observed in monolayer regions. This indicates that the charge transfer between the layers occurs immediately after excitation and is effective only for hot carriers (in agreement with previous pump probe measurements [Ceballos 2014]). The observed PL emission is related to thermalized excitons and the unchanged decay times show that they are not affected by the inter-layer transfer. This might be the result of the weak localization potential induced by the moiré pattern. A larger intensity of the inter-layer exciton PL has been observed in $MoSe_2/MoS_2$ heterostructures [Baranowski 2017b] with increasing temperature. This is probably the hallmark

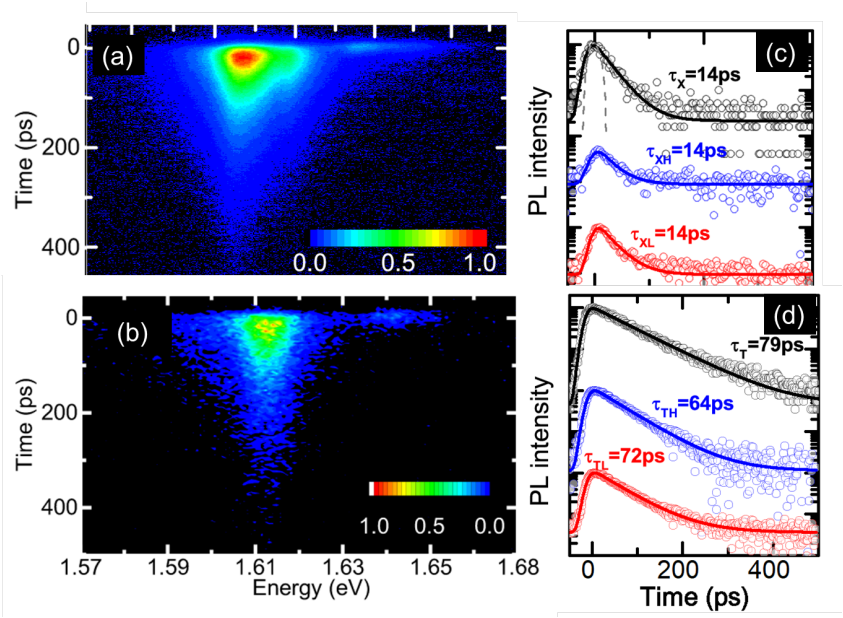

Figure 4.14: Spectrally resolved PL time evolution measured in the (a) heterostructure and (b) isolated $MoSe_2$ monolayer area. Decay curves (open circles) corresponding to low (red) and high (blue) energy of $MoSe_2$ (c) exciton and (d) trion from the heterostructure and decay of exciton PL outside heterostructure (black) together with fitted monoexponential decays. The extracted decay time constants are specified above the corresponding curves. The instrument response function is traced as a dashed line in panel (c).

of the thermal activation of excitons from shallow traps, represented by the moiré potential, followed by inter-layer transfer. However, further studies are needed to clarify this aspect, notably to distinguish it from a possible indirect character in k-space of the inter-layer transitions [Miller 2017, Kunstmann 2018].

4.4.3 Valley polarization of moiré excitons

We have investigated the valley polarization properties of the intra-layer $MoSe_2$ excitons by exciting the PL with circularly polarized light and detecting the co-polarized and cross-polarized circular polarization PL component. We show the PL spectra of the isolated monolayer and of the monolayer in the heterostructure region in Fig. 4.15(a,b). The degree of circular polarization P_c of the PL $P_c = (I_{co} - I_{cross})/(I_{co} + I_{cross})$ is always positive (see green bars in Fig. 4.15). The degree of circular polarization is very similar for the heterostructure and monolayer regions and amounts to about 10% and 13% for the trion and the exciton, respectively. There is no significant difference between the polarization of the high and low energy transitions in the heterostructure region. This suggests that, consistent with theoretical predictions [Yu 2017], the selection rules for the intra-layer exciton transitions are not influenced by the presence of the moiré pattern, thus all tran-

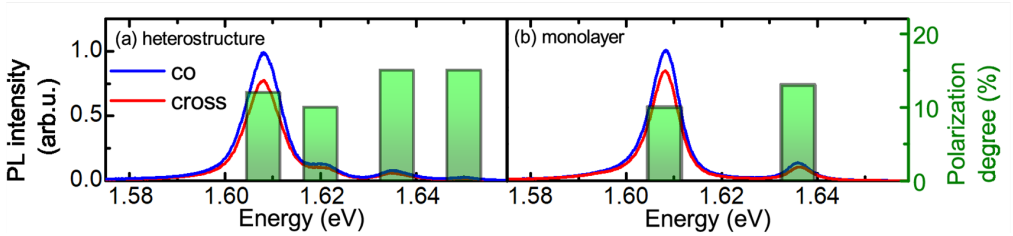

Figure 4.15: Circularly polarization resolved PL spectrum of $MoSe_2$ measured (a) in and (b) out of the heterostructure. The green bars represent the degree of circular polarization of the peaks.

sitions have the same polarization. This can be explained by considering that the rotational symmetry of the transitions does not change in the plane of the monolayers, in contrast to the inter-layer transition for which the helicity of the emitted light varies across the moiré pattern [Yu 2017, Wu 2018]. The observed significant polarization is surprising considering that we excite far from the excitonic transitions of $MoSe_2$ [Wang 2015c, Kioseoglou 2016, Baranowski 2017a, Surrente 2017]. This effect might be related to the encapsulation in hBN because we observe a similar degree of circular polarization in both the heterostructure and monolayer regions, although the exact reason for the relatively high degree of polarization after encapsulation requires additional investigation.

4.5 Conclusions

In conclusion, we have demonstrated the impact of the moiré pattern formed in a $MoS_2/MoSe_2$ heterostructure on the optical spectra of the intra-layer exciton species. The potential fluctuations resulting from locally different atomic registries, cause the trion and exciton transitions of $MoSe_2$ and MoS_2 to split into two peaks related to optically active local minima of the moiré potential. The nature of the observed doublets has been confirmed by detailed spatial mapping of the PL and by its temperature dependence. Polarization resolved measurements reveal that the selection rules of the transitions do not change with respect to the case of isolated monolayers. The PL dynamics shows that moiré induced potential does not change significantly the oscillator strength of the transitions. However, the moiré potential may be responsible for the suppression of the inter-layer transfer of thermalized excitons. All of the results presented are in agreement with the theoretically predicted influence of moiré pattern on intra-layer excitons in transition metal dichalcogenides.

Chapter 5

Magneto optics of the $MoS_2/MoSe_2$ heterostructures

Contents

5.1 Magneto optics of TMDC 53
5.2 $MoSe_2$ neutral and charged excitons in magnetic field . . . 55
5.3 Valley polarization of the neutral and charged excitons in magnetic field 58
5.4 Conclusions 59

In this chapter, we discuss the results of the optical properties of the excitons and charged excitons in high magnetic field. We compare the magneto optical properties of the excitons in isolated MoS_2 and $MoSe_2$ moolayers with the moiré intra-layer excitons in $MoS_2/MoSe_2$.We also compare the valley polarization for the excitons in monolayer $MoSe_2$ grown by CVD and in high quality exfoliated monolayer $MoSe_2$ encapsulated in hexagonal BN.

5.1 Magneto optics of TMDC

The existence of a valley-contrasting magnetic moment opens the possibility of controlling the valley pseudospin with an external magnetic field.[Rose 2013, Li 2014b, MacNeill 2015, Mitioglu 2015, Srivastava 2015b, Wang 2015a]. The application of a magnetic field, perpendicular to the layer lifts the valley degeneracy, splitting the exciton transitions. The lifting of the degeneracy induced by the magnetic field is enabled by the unequal magnetic moments of the conduction μ^{c} and valence bands μ^{v} involved in the transition. In the framework of magneto-optical spectroscopy of intra-layer excitons, three possible contributions have been identified. The contributions related to the spin magnetic moment $\mu_s^{c,v}$ cancel out since the optical transitions are spin-conserving, leading to $\mu_s^{c} = \mu_s^{v}$. Conversely, the atomic orbital contribution μ_l is expected to be non-zero, owing to the different orbitals which form the band edge states of the conduction and the valence band [Liu 2013b], with a total contribution adding up to $\mu_l = -4\mu_B$. The third contribution is associated with the Berry curvature and is referred to as valley magnetic moment [Xiao 2012], with values $\pm\mu_k^{c} = \pm(m_0/m_e)\mu_B$ for the conduction band and $\pm\mu_k^{v} = \pm(m_0/m_h)\mu_B$ for the valence band, in the K^+ and K^- valleys, respectively. Here, m_0 represents

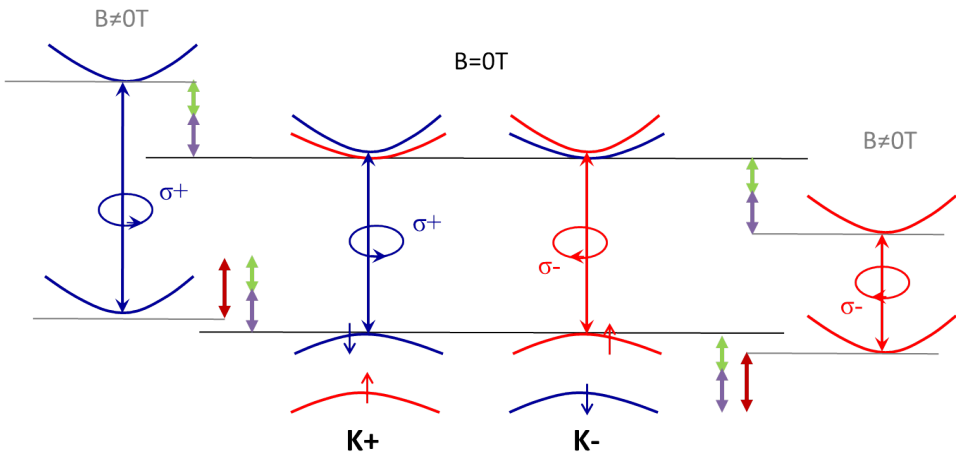

Figure 5.1: Scheme of the magnetic field induced shift for both valleys. The shift originating from each contribution is marked by different colours: green corresponds to the spin magnetic moment, violet and red to the inter and intra cellular magnetic moments, respectively.

the free electron mass, while m_e and m_h denote the effective mass of the electrons and holes, respectively. The shift induced by the magnetic field for each valley for all three contribution is presented in Fig5.1. The shift originating from each contribution is marked by different colours: green corresponds to the spin magnetic moment, violet and red to the inter and intra cellular magnetic moments, respectively. The total shift is a sum of all the contributions. In experiment we measure typically the energy difference between emission in both circular polarizations. In a simple two band model, the masses of the valence and the conduction band are identical so that the intercellular valley magnetic moment is the same for the valence and conduction bands. Thus, there is no intercellular contribution to the valley splitting which arises solely from the $\mu_k = \pm 2\mu_B$ angular momentum of the valence d-orbitals giving a valley g-factor $g_v = -4$, close to the reported values from photoluminescence (PL) studies in transition metal diselenides.[MacNeill 2015, Li 2014b, Srivastava 2015b, Aivazian 2015b, Mitioglu 2015, Wang 2015a].

The resulting Zeeman effect influences the carrier and exciton populations in the two valleys and can potentially enable their manipulation. The chiral selection rules provide a convenient tool to monitor the valley polarization by measuring the degree of circular polarization (DCP) of the monolayer photoluminescence (PL) defined as $P_c = \left(I_{\sigma_+} - I_{\sigma_-}\right) / \left(I_{\sigma_+} + I_{\sigma_-}\right)$, where $I_{\sigma_\pm}$ denote the PL intensities in $\sigma_\pm$ polarizations [Zeng 2012, Mak 2012]. However, the understanding of the magnetic field influence on DCP is not complete. For monolayer WS_2 and WSe_2 a counterintuitive intensity gain of the neutral exciton PL line shifting towards higher energy has been shown [Aivazian 2015b, Plechinger 2016a, Neumann 2017, Koperski 2018]. On the other hand, for monolayer $MoSe_2$ and $MoTe_2$ an opposite behavior was reported; the intensity of the lower energy line increases with

the field as expected for the exciton system tending to a thermal equilibrium [MacNeill 2015, Wang 2015a, Arora 2016, Koperski 2018]. Furthermore, some reports showed negligible impact on the DCP of the magnetic field even for fields as large as 30 T [Wang 2015a, Koperski 2018, Mitioglu 2015, Mitioglu 2018]. Moreover, different behaviors were reported for neutral and charged excitons (trions) [Aivazian 2015b, Mitioglu 2015].

5.2 $MoSe_2$ neutral and charged excitons in magnetic field

We have performed measurements of the neutral and charged excitons in the $MoSe_2$ monolayers and moiré intralayer excitons in $MoS_2/MoSe_2$ in high magnetic field in the High Field Magnet Laboratory (HFML) in Nijmegen. We went there a visitors working with Marion Severijnen as a local contact. The detailed description of the experimental techniques used is provided in the Chapter 2. We worked with two samples: CVD-grown monolayer $MoSe_2$ film sandwiched between two CVD-grown MoS_2 monolayer films and highly aligned $MoS_2/MoSe_2$ heterobilayer fabricated by mechanical exfoliation [Castellanos-Gomez 2014a] and fully encapsulated in hBN, both samples are described in details in Chapter 2. Importantly, on the last sample, part of the $MoSe_2$ flake does not overlap with the MoS_2 monolayer, so we were able to look at the properties of pure $MoSe_2$. On the heterostructure area of this sample, the presence of a two highly aligned monolayers with commensurate lattice leads to the formation of a moiré pattern. This portion of the sample displays a significantly different PL and absorption spectra [Zhang 2017], and is referred to as moiré in the following.

We present the magneto-PL spectra of the three investigated samples measured up to 9 T in Fig. 5.2. The spectra of the trilayer and of the monolayer samples, shown in Fig. 5.2(a,b), consist of two emission lines. The weaker, higher energy peak is assigned to the recombination of the neutral exciton. The stronger peak, which is red shifted by approximately 30 meV with respect to the neutral exciton, originates from the recombination of the trion, in agreement with previous reports [Ross 2013]. The exciton and trion have Gaussian line shapes, with a full width at half maximum (FWHM) of about 10 meV. The encapsulation of mechanically exfoliated $MoSe_2$ in hBN leads to a change of the line shape to Lorentzian and a reduction of the line width to less than 5 meV, as visible in Fig. 5.2(b). This reduced broadening points out a weaker exciton scattering on defects and attests to their lower density in the monolayer sample.

Fig. 5.2(c) shows the magneto-PL spectrum of intra-layer moiré excitons hosted in a hBN-encapsulated $MoSe_2$ that overlaps with a MoS_2 monolayer.The presence of a moiré pattern induces a splitting of the excitonic transitions as described in detail in the previous chapter. The splitting is nicely illustrated by the multiple excitonic resonances visible in the PL spectrum of Fig. 5.2(c).

For all three samples, at zero magnetic field the PL intensity resolved in the

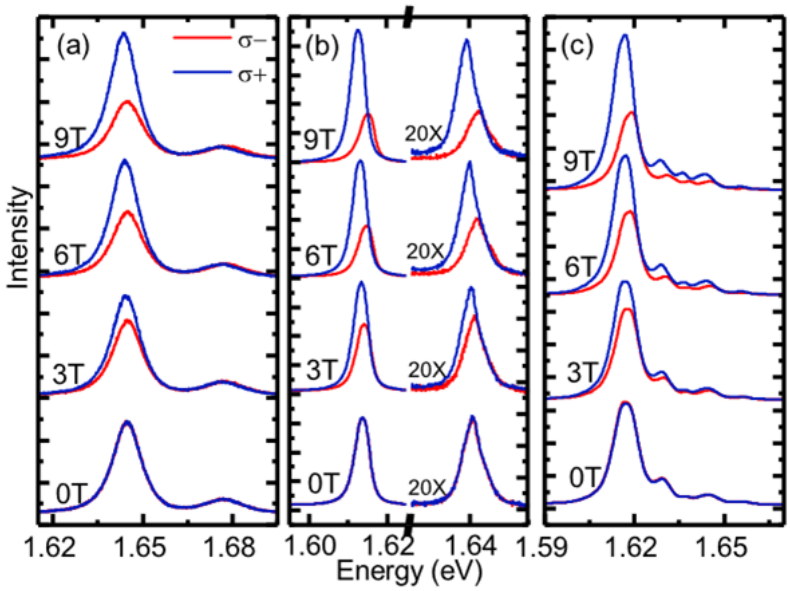

Figure 5.2: Magneto-PL spectra up to 9 T of (a) trilayer, (b) hBN-encapsulated monolayer and (c) moiré sample. The high energy (exciton) peak in panel (b) has been renormalized for clarity. Blue and red lines denote PL signals in σ_+ and σ_- circular polarizations. respectively. The excitation beam in circularly polarized in (a) and linearly polarized in (b) and (c).

two circular polarizations is the same, which yields a negligible DCP. This results from the use of a linearly polarized excitation beam in the case of Fig. 5.2(b), which injects excitons in both the K_+ and K_- valleys. The spectra shown in Fig. 5.2(a) have been excited with a circularly polarized laser. However, the valley-selective excitation in this case is neutralized by the very efficient inter-valley scattering in $MoSe_2$, owing to a large excess energy of the photo-created excitons [Baranowski 2017a, Tornatzky 2018]. This effectively equalizes the exciton populations in the two valleys in the same way as a linearly polarized excitation would. Applying a magnetic field results in two effects which can be noted in Fig. 5.2, namely a splitting of the PL peaks and a change of the relative intensities of the two circular polarization components of the PL.

We will first examine the trend of the the splitting of the PL peaks, defined as $\Delta E = E_{\sigma_+} - E_{\sigma_-} = g\mu_B B$, where $E_{\sigma_\pm}$ denotes the PL transition energies observed in $\sigma_\pm$ polarizations, g is the effective g-factor, μ_B is 58 μeV/T is the Bohr magneton and B is the applied magnetic field. To extract the transition energies, we fit the experimental data with Gaussian functions. As shown in Fig. 5.3, the experimentally observed splitting is linear for all the investigated excitonic species, which allowed us to evaluate the g-factors. In monolayer TMDC, the magnetic field-induced splitting is commonly attributed to three contributions as discussed in the introduction to this chapter. Indeed, as seen

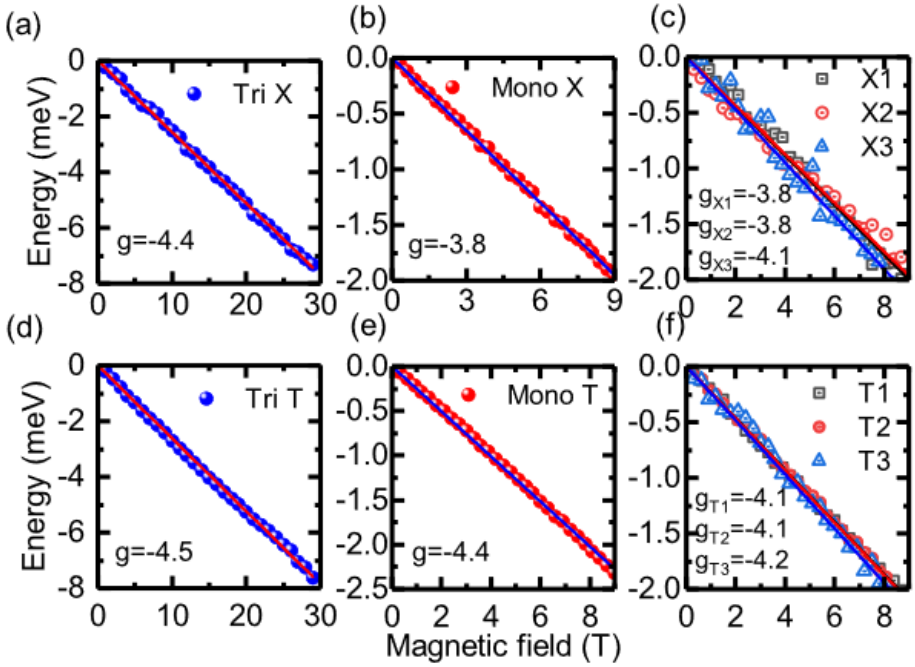

Figure 5.3: Valley Zeeman splitting of neutral and charged exciton measured on the trilayer (a,d, respectively), monolayer (b,e, respectively) and moiré samples (c,f, respectively).

in Fig. 5.3, the observed splitting of the neutral exciton PL lines scales with g-factors in range from -3.8 to -4.4, in agreement with a multitude of prior reports [Li 2014a, MacNeill 2015, Srivastava 2015b, Aivazian 2015a, Wang 2015a, Plechinger 2016a, Stier 2016a, Mitioglu 2016, Koperski 2018, Zipfel 2018, Li 2019, Arora 2016, Mitioglu 2018]. The small deviations of the experimentally observed g-factor from the value of -4 are usually ascribed to the contribution from the intercellular magnetic moment [Mitioglu 2016] and to a contribution of the p-orbitals to the band edge states [Liu 2015]. We report for the first time in Fig. 5.3(c) the magnetic field induced splitting of moiré intralayer excitons. Their g-factor is the same within experimental error as that of the neutral exciton measured on monolayer areas of the same sample. This observation can be understood based on the fact that K point states in TMDC heterobilayer are known not to hybridize, thus keeping their original monolayer character [Gao 2017, Hanbicki 2018]. Moreover, the moiré pattern induces a spatial modulation of the band gap [Wu 2017b], which does not introduce a variation in the nature of the band edge states. The orbital angular momentum matrix elements of intra-layer moiré excitons are expected to be the same as those of free excitons in isolated monolayers. Hence, the deviation of the g-factor of moiré excitons from that of neutral excitons should be negligible, as indeed experimentally observed.

As for the charged exciton, the captured negative charge provides an additional

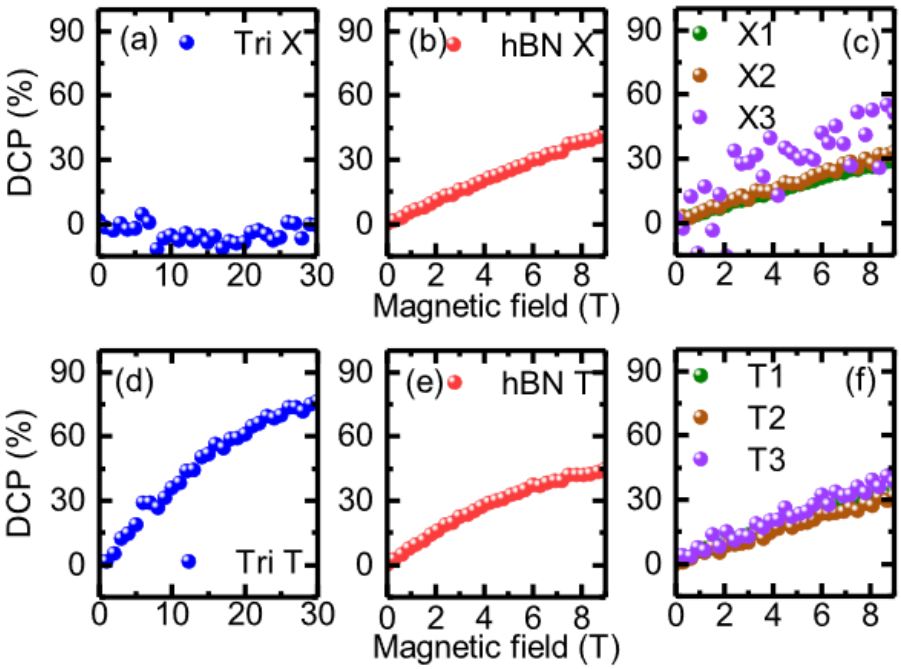

Figure 5.4: Magnetic field induced DCP of neutral and charged exciton measured on the trilayer (a,d, respectively), hBN-encapsulated monolayer (b,e, respectively) and moiré samples (c,f, respectively).

magnetic moment to the complex, which contributes in the same way to the initial and final energy of the charged exciton. Thus, the g-factor of the charged exciton is approximately the same as for the neutral exciton, as shown in Fig. 5.3(c,d) [Li 2014a, MacNeill 2015, Srivastava 2015b, Aivazian 2015a, Wang 2015a, Li 2019].

5.3 Valley polarization of the neutral and charged excitons in magnetic field

The splitting of the neutral and charged exciton levels via the valley Zeeman effect can lead to an unbalanced population in the K_+ and K_- valleys. As a result of the chiral selection rules, the PL intensities in the two circular polarizations are expected to be different. Indeed as observed in Fig. 5.2(a), (b) only for the charged exciton, the low energy PL line observed in σ^+ polarization exhibits a higher intensity. This leads to a positive DCP, as required by thermal occupation of the Zeeman split states. This result is in agreement with earlier reports on monolayer $MoSe_2$ [MacNeill 2015, Li 2014b, Wang 2015a]. This behavior is opposite to the one reported for WSe_2 and WS_2 monolayers, where the high energy line showed stronger intensity than the low energy one, leading to a negative DCP [Aivazian 2015a, Plechinger 2016a]. In these cases, the negative DCP was ascribed

to different exciton formation rates in K_+ and K_- valleys. In our case, if present, this mechanism is clearly less efficient than the valley relaxation, which drives the exciton system toward thermal equilibrium. An exception to this general trend is represented by the DCP of exciton PL in the trilayer, where we observed very similar intensities in the two circular polarizations, as shown in Fig. 5.2(a).

To investigate the magnetic field influence on DCP in more detail, we plot the experimentally evaluated DCP for the three samples in Fig. 5.4. For the exciton PL from the trilayer sample (see Fig. 5.4(a)) the DCP is virtually absent up to about 22 T. In the same sample, the charged exciton reaches instead a considerably larger DCP of 75% at 30 T, as shown in Fig. 5.4(d). In the mechanically exfoliated $MoSe_2$ monolayer, the magnetic field induced DCP of both the neutral and the charged exciton increases steadily, as shown in Fig. 5.4(b,e). A similar behaviour is displayed by the excitons in the moiré sample (see Fig. 5.4(c,f)), which suggests that the optically bright excitonic species are all subject to similar relaxation processes.

5.4 Conclusions

We have performed measurements of the neutral and charged excitons in the $MoSe_2$ monolayers and moiré intralayer excitons in $MoS_2/MoSe_2$ in high magnetic field. The behaviour of moiré excitons in a magnetic field is essentially the same as normal excitons. Notably the g-factors $\simeq -4$ are identical within experimental error. Using high magnetic field it is possible to control the degree of valley polarization. The difference in the enhancement of the valley polarization by magnetic field are the subject of further studies and modeling.

Chapter 6

Conclusions

We have used optical spectroscopy, in particular photoluminescence, reflectivity, Raman scattering and time resolved photoluminescence to investigate TMDC heterostructures. Magneto-optical experiments have been performed at the EMFL high field facility in Nijmegen.

We have observed a persistent photodoping effect on the exciton emission in a $MoS_2/MoSe_2/MoS_2$ heterostructure. The intensity of the inter-layer exciton PL emission is decreased under laser illumination. The simultaneous change of the neutral and charged exciton emission indicates the increased doping level. The increased intensity of intra-layer exciton emission and decreased intensity of inter-layer exciton suggests that the photodoping reduces the inter-layer charge transfer efficiency. This phenomenon is persistent at low temperature and under vacuum unless the sample is exposed to air, which indicates this photodoping is related to the physically absorbed water and oxygen molecules on the surface. The results provide a concise method to modulate the inter-layer charge transfer efficiency.

We have investigated $MoSe_2/MoS_2$ heterostructures with different twist angle. The twist angle was predetermined during the stacking procedure and subsequently confirmed using polarization resolved measurements of the second harmonic generation. We observed that for heterostructures with almost zero degree twist angle, the $MoSe_2$ excitonic emission and absorption is accompanied by side peaks on the high energy side of the spectrum. This is the first experimental observation of moiré intralayer excitons in an atomically thin TMDC. The PL dynamics shows that moiré induced potential does not change significantly the oscillator strength of the transitions. However, the moiré potential may be responsible for the suppression of the inter-layer transfer of thermalized excitons. All of the results presented are in agreement with the theoretically predicted influence of moiré pattern on intra-layer excitons in transition metal dichalcogenides.

Finally, we have investigated the optical properties of the excitons and charged excitons in high magnetic field. We compare the magneto optical properties of the excitons in isolated MoS_2 and $MoSe_2$ monolayers with the moiré intra-layer excitons in $MoS_2/MoSe_2$. The behaviour of moiré excitons in a magnetic field is essentially the same as normal excitons. Notably the g-factors $\simeq -4$ are identical within experimental error. We also compare the valley polarization for the excitons in monolayer $MoSe_2$ grown by CVD and in high quality exfoliated monolayer $MoSe_2$ encapsulated in hexagonal BN. Using polarisation resolved optics to measure the degree of circular polarisation (DCP) of the PL emission, we have demonstrated that high magnetic field can be used to control the degree of valley polarisation.

The difference in the enhancement of the valley polarization by magnetic field are the subject of further studies and modeling.

Appendix A

Publications

Publications based on the results of this thesis:

1. **N. Zhang**, A. Surrente, M. Baranowski, D. Dumcenco, Y. -C. Kung, D. K. Maude, A. Kis, and P. Plochocka
   "Impact of photodoping on inter- and intralayer exciton emission in a $MoS_2/MoSe_2/MoS_2$ heterostructure "
   Applied Physics Letters, **113**, 062107 (2018)

2. **N. Zhang**, A. Surrente, M. Baranowski, D. K. Maude, P. Gant, A. Castellanos and P. Plochocka
   "Moiré Intralayer Excitons in a $MoSe_2/MoS_2$ Heterostructure"
   Nano Letters, **18(12)**, 7651-7657 (2018)

3. **N. Zhang**, A. Surrente, Ł. Klopotowski, M. Baranowski, A. A. Mitioglu, M. V. Ballottin, P. C. M. Cristianen, M. Aleszkiewicz, D. Dumcenco, Y. -C. Kung, D. K. Maude, A. Kis and P. Plochocka
   "Influence of the magnetic field on the circular polarization of photoluminescence frommonolayer $MoSe_2$"
   Under preparation

Other publications:

1. A. M. Soufiani, Z. Yang, T. Young, A. Miyata, A. Surrente, A. Pascoe, K. Galkowski, M. Abdi-Jalebi, R. Brenes, J. Urban, **N. Zhang**, V. Bulovic, O. Portugall, Y. B. Cheng, R. J. Nicholas, A. Ho-Baillie, M. A. Green, P. Plochocka and S. D. Stranks
   "Impact of microstructure on the electron - hole interaction in lead halide perovskites"
   Energy and Enviromental Science, **10**, 1358-1366 (2017)

2. M. Baranowski, J. M. Urban, **N. Zhang**, A. Surrente, D. K. Maude, Z. Andaji-Garmaroudi, S. D. Stranks and P. Płochocka
   Static and Dynamic Disorder in Triple-Cation Hybrid Perovskites.
   The Journal of Physical Chemistry C, **122 (30)**, 17473–17480 (2018)

3. M. Baranowski, A. Surrente, Ł. Klopotowski, J. M. Urban, **N. Zhang**, D. K. Maude, K. Wiwatowski, S. Mackowski, Y. -C. Kung, D. Dumcenco, A. Kis , and P. Płochocka
   Probing the Interlayer Exciton Physics in a $MoS_2/MoSe_2/MoS_2$ van der

Waals Heterostructure.
Nano Letters, **17 (10)**, 6360–6365,(2017)

4. A. Surrente, Ł. Klopotowski, **N. Zhang**, M. Baranowski, A. A. Mitioglu, M. V. Ballottin, P. C. M. Cristianen, D. Dumcenco, Y. -C. Kung, D. K. Maude, A. Kis , and P. Płochocka
Intervalley Scattering of Interlayer Excitons in a $MoS_2/MoSe_2/MoS_2$ Heterostructure in High Magnetic Field.
Nano Letters, **18 (6)**, 3994–4000, (2018)

Bibliography

[Acerce 2015] Muharrem Acerce, Damien Voiry and Manish Chhowalla. *Metallic 1T phase MoS2 nanosheets as supercapacitor electrode materials.* Nature Nanotechnology, vol. 10, no. 4, pages 313–318, April 2015. (Cited on page 3.)

[Aivazian 2015a] Grant Aivazian, Zhirui Gong, Aaron M Jones, Rui-Lin Chu, Jiaqiang Yan, David G Mandrus, Chuanwei Zhang, David Cobden, Wang Yao and Xiaodong Xu. *Magnetic control of valley pseudospin in monolayer WSe_2.* Nature Physics, vol. 11, no. 2, page 148, 2015. (Cited on pages 33, 57 and 58.)

[Aivazian 2015b] Grant Aivazian, Zhirui Gong, Aaron M Jones, Rui-Lin Chu, Jiaqiang Yan, David G Mandrus, Chuanwei Zhang, David Cobden, Wang Yao and Xiaodong Xu. *Magnetic control of valley pseudospin in monolayer WSe_2.* Nature Physics, vol. 11, no. 2, pages 148–152, 2015. (Cited on pages 54 and 55.)

[Arora 2016] Ashish Arora, Robert Schmidt, Robert Schneider, Maciej R Molas, Ivan Breslavetz, Marek Potemski and Rudolf Bratschitsch. *Valley Zeeman splitting and valley polarization of neutral and charged excitons in monolayer $MoTe_2$ at high magnetic fields.* Nano Letters, vol. 16, no. 6, pages 3624–3629, 2016. (Cited on pages 55 and 57.)

[Asahina 1983] Hideo Asahina, Yusei Maruyama and Akira Morita. *Optical reflectivity and band structure of black phosphorus.* Physica B+C, vol. 117–118, Part 1, pages 419 – 421, 1983. (Cited on page 2.)

[Baek 2020] Hyeonjun Baek, Mauro Brotons-Gisbert, Zhe Xian Koong, Aidan Campbell, Markus Rambach, Kenji Watanabe, Takashi Taniguchi and Brian D Gerardot. *Highly tunable quantum light from moir\'e trapped excitons.* arXiv preprint arXiv:2001.04305, 2020. (Cited on page 39.)

[Bandurin 2017] Denis A Bandurin, Anastasia V Tyurnina, L Yu Geliang, Artem Mishchenko, Viktor Zólyomi, Sergey V Morozov, Roshan Krishna Kumar, Roman V Gorbachev, Zakhar R Kudrynskyi, Sergio Pezzini, Zakhar D Kovalyuk, Uli Zeitler, Konstantin S Novoselov, Amalia Patanè, Laurence Eaves, Irina V Grigoreva, Vladimir I Falko, Andre K Geim and Yang Cao. *High electron mobility, quantum Hall effect and anomalous optical response in atomically thin InSe.* Nature Nanotechnology, vol. 12, no. 3, pages 223–227, 2017. (Cited on page 15.)

[Baranowski 2017a] M Baranowski, A Surrente, DK Maude, M Ballottin, AA Mitioglu, PCM Christianen, YC Kung, D Dumcenco, A Kis and P Plochocka.

Dark excitons and the elusive valley polarization in transition metal dichalcogenides. 2D Materials, vol. 4, no. 2, page 025016, 2017. (Cited on pages 12, 52 and 56.)

[Baranowski 2017b] Michal Baranowski, Alessandro Surrente, L Klopotowski, JM Urban, Nan Zhang, Duncan K Maude, Kamil Wiwatowski, Sebastian Mackowski, Yen-Cheng Kung, Dumitru Dumcenco, Andras Kis and Paulina Plochocka. *Probing the Interlayer Exciton Physics in a MoS2/MoSe2/MoS2 van der Waals Heterostructure.* Nano Letters, vol. 17, no. 10, pages 6360–6365, 2017. (Cited on pages 16, 30, 38, 44 and 50.)

[Butler 2013] Sheneve Z. Butler, Shawna M. Hollen, Linyou Cao, Yi Cui, Jay A. Gupta, Humberto R. Gutiérrez, Tony F. Heinz, Seung Sae Hong, Jiaxing Huang, Ariel F. Ismach, Ezekiel Johnston-Halperin, Masaru Kuno, Vladimir V. Plashnitsa, Richard D. Robinson, Rodney S. Ruoff, Sayeef Salahuddin, Jie Shan, Li Shi, Michael G. Spencer, Mauricio Terrones, Wolfgang Windl and Joshua E. Goldberger. *Progress, Challenges, and Opportunities in Two-Dimensional Materials Beyond Graphene.* ACS Nano, vol. 7, no. 4, pages 2898–2926, 2013. PMID: 23464873. (Cited on page 2.)

[Cadiz 2016a] Fabian Cadiz, Cedric Robert, Gang Wang, Wilson Kong, Xi Fan, Mark Blei, Delphine Lagarde, Maxime Gay, Marco Manca, Takashi Taniguchi*et al. Ultra-low power threshold for laser induced changes in optical properties of 2D molybdenum dichalcogenides.* 2D Materials, vol. 3, no. 4, page 045008, 2016. (Cited on page 30.)

[Cadiz 2016b] Fabian Cadiz, Simon Tricard, Maxime Gay, Delphine Lagarde, Gang Wang, Cedric Robert, Pierre Renucci, Bernhard Urbaszek and Xavier Marie. *Well separated trion and neutral excitons on superacid treated MoS2 monolayers.* Applied Physics Letters, vol. 108, no. 25, page 251106, 2016. (Cited on page 13.)

[Cadiz 2017] F. Cadiz, E. Courtade, C. Robert, G. Wang, Y. Shen, H. Cai, T. Taniguchi, K. Watanabe, H. Carrere, D. Lagarde, M. Manca, T. Amand, P. Renucci, S. Tongay, X. Marie and B. Urbaszek. *Excitonic linewidth approaching the homogeneous limit in MoS 2-based van der Waals heterostructures.* Physical Review X, vol. 7, no. 2, page 021026, 2017. (Cited on pages 15 and 44.)

[Cao 2018] Yuan Cao, Valla Fatemi, Shiang Fang, Kenji Watanabe, Takashi Taniguchi, Efthimios Kaxiras and Pablo Jarillo-Herrero. *Unconventional superconductivity in magic-angle graphene superlattices.* Nature, vol. 556, no. 7699, pages 43–50, April 2018. (Cited on page 17.)

[Castellanos-Gomez 2013] Andres Castellanos-Gomez, Rafael Roldán, Emmanuele Cappelluti, Michele Buscema, Francisco Guinea, Herre SJ van der Zant and

Gary A Steele. *Local strain engineering in atomically thin MoS2.* Nano letters, vol. 13, no. 11, pages 5361–5366, 2013. (Cited on page 27.)

[Castellanos-Gomez 2014a] Andres Castellanos-Gomez, Michele Buscema, Rianda Molenaar, Vibhor Singh, Laurens Janssen, Herre SJ Van Der Zant and Gary A Steele. *Deterministic transfer of two-dimensional materials by all-dry viscoelastic stamping.* 2D Materials, vol. 1, no. 1, page 011002, 2014. (Cited on page 55.)

[Castellanos-Gomez 2014b] Andres Castellanos-Gomez, Leonardo Vicarelli, Elsa Prada, Joshua O Island, K L Narasimha-Acharya, Sofya I Blanter, Dirk J Groenendijk, Michele Buscema, Gary A Steele, J V Alvarez, Henny W Zandbergen, J J Palacios and Herre S J van der Zant. *Isolation and characterization of few-layer black phosphorus.* 2D Materials, vol. 1, no. 2, page 025001, 2014. (Cited on page 2.)

[Ceballos 2014] Frank Ceballos, Matthew Z Bellus, Hsin-Ying Chiu and Hui Zhao. *Ultrafast charge separation and indirect exciton formation in a MoS2–MoSe2 van der Waals heterostructure.* ACS Nano, vol. 8, no. 12, pages 12717–12724, 2014. (Cited on pages 44 and 50.)

[Chen 2016] Hailong Chen, Xiewen Wen, Jing Zhang, Tianmin Wu, Yongji Gong, Xiang Zhang, Jiangtan Yuan, Chongyue Yi, Jun Lou, Pulickel M Ajayan, Wei Zhuang, Guangyu Zhang and Junrong Zheng. *Ultrafast formation of interlayer hot excitons in atomically thin MoS_2/WS_2 heterostructures.* Nature Communications, vol. 7, page 12512, 2016. (Cited on page 44.)

[Chen 2018a] Shao-Yu Chen, Thomas Goldstein, Takashi Taniguchi, Kenji Watanabe and Jun Yan. *Coulomb-bound four- and five-particle intervalley states in an atomically-thin semiconductor.* Nature Communications, vol. 9, no. 1, page 3717, September 2018. (Cited on page 14.)

[Chen 2018b] Shao-Yu Chen, Thomas Goldstein, Jiayue Tong, Takashi Taniguchi, Kenji Watanabe and Jun Yan. *Superior Valley Polarization and Coherence of 2s Excitons in Monolayer WSe_2.* Physical Review Letters, vol. 120, no. 4, page 046402, 2018. (Cited on page 15.)

[Chen 2018c] Yabin Chen, Chaoyu Chen, Robert Kealhofer, Huili Liu, Zhiquan Yuan, Lili Jiang, Joonki Suh, Joonsuk Park, Changhyun Ko, Hwan Sung Choe, José Avila, Mianzeng Zhong, Zhongming Wei, Jingbo Li, Shushen Li, Hongjun Gao, Yunqi Liu, James Analytis, Qinglin Xia, Maria C. Asensio and Junqiao Wu. *Black Arsenic: A Layered Semiconductor with Extreme In-Plane Anisotropy.* Advanced Materials, vol. 30, no. 30, page 1800754, 2018. (Cited on page 2.)

[Chernikov 2014] Alexey Chernikov, Timothy C Berkelbach, Heather M Hill, Albert Rigosi, Yilei Li, Ozgur Burak Aslan, David R Reichman, Mark S Hybertsen

and Tony F Heinz. *Exciton binding energy and nonhydrogenic Rydberg series in monolayer WS 2*. Physical review letters, vol. 113, no. 7, page 076802, 2014. (Cited on pages 9 and 10.)

[Chiu 2015] Ming-Hui Chiu, Chendong Zhang, Hung-Wei Shiu, Chih-Piao Chuu, Chang-Hsiao Chen, Chih-Yuan S Chang, Chia-Hao Chen, Mei-Yin Chou, Chih-Kang Shih and Lain-Jong Li. *Determination of band alignment in the single-layer MoS 2/WSe 2 heterojunction*. Nature communications, vol. 6, no. 1, pages 1–6, 2015. (Cited on page 16.)

[Choi 2019] Junho Choi, Wei-Ting Hsu, Li-Syuan Lu, Liuyang Sun, Hui-Yu Cheng, Ming-Hao Lee, Jiamin Quan, Kha Tran, Chun-Yuan Wang, Matthew Staab*et al. Moir\'e Potential Impedes Interlayer Exciton Diffusion in van der Waals Heterostructures*. arXiv preprint arXiv:1912.11101, 2019. (Cited on page 38.)

[Ciarrocchi 2018] Alberto Ciarrocchi, Dmitrii Unuchek, Ahmet Avsar, Kenji Watanabe, Takashi Taniguchi and Andras Kis. *Control of interlayer excitons in two-dimensional van der Waals heterostructures*. arXiv preprint arXiv:1803.06405, 2018. (Cited on page 38.)

[Ciarrocchi 2019] Alberto Ciarrocchi, Dmitrii Unuchek, Ahmet Avsar, Kenji Watanabe, Takashi Taniguchi and Andras Kis. *Polarization switching and electrical control of interlayer excitons in two-dimensional van der Waals heterostructures*. Nature photonics, vol. 13, no. 2, pages 131–136, 2019. (Cited on page 33.)

[Conley 2013] Hiram J Conley, Bin Wang, Jed I Ziegler, Richard F Haglund Jr, Sokrates T Pantelides and Kirill I Bolotin. *Bandgap engineering of strained monolayer and bilayer MoS2*. Nano letters, vol. 13, no. 8, pages 3626–3630, 2013. (Cited on page 27.)

[Courtade 2018] E Courtade, B Han, S Nakhaie, Cédric Robert, Xavier Marie, Pierre Renucci, T Taniguchi, K Watanabe, L Geelhaar, JMJ Lopes*et al. Spectrally narrow exciton luminescence from monolayer MoS2 and MoSe2 exfoliated onto epitaxially grown hexagonal BN*. Applied Physics Letters, vol. 113, no. 3, page 032106, 2018. (Cited on page 36.)

[Cudazzo 2011] Pierluigi Cudazzo, Ilya V. Tokatly and Angel Rubio. *Dielectric screening in two-dimensional insulators: Implications for excitonic and impurity states in graphane*. Phys. Rev. B, vol. 84, page 085406, Aug 2011. (Cited on page 10.)

[Currie 2015] M Currie, AT Hanbicki, G Kioseoglou and BT Jonker. *Optical control of charged exciton states in tungsten disulfide*. Applied Physics Letters, vol. 106, no. 20, page 201907, 2015. (Cited on pages 30 and 32.)

[Das 2019] Sonali Das, Deepak Pandey, Jayan Thomas and Tania Roy. *The Role of Graphene and Other 2D Materials in Solar Photovoltaics*. Advanced Materials, vol. 31, no. 1, page 1802722, 2019. (Cited on page 2.)

[Dean 2013] CR Dean, L Wang, P Maher, C Forsythe, F Ghahari, Y Gao, J Katoch, M Ishigami, P Moon, M Koshino, T Taniguchi, K Watanabe, K L Shepard, J Hone and P Kim. *Hofstadter's butterfly and the fractal quantum Hall effect in moiré superlattices*. Nature, vol. 497, no. 7451, pages 598–602, 2013. (Cited on page 17.)

[Dong 2017] Rui Dong and Irma Kuljanishvili. *Progress in fabrication of transition metal dichalcogenides heterostructure systems*. Journal of Vacuum Science & Technology B, Nanotechnology and Microelectronics: Materials, Processing, Measurement, and Phenomena, vol. 35, no. 3, page 030803, 2017. (Cited on page 16.)

[Duong 2017] Dinh Loc Duong, Seok Joon Yun and Young Hee Lee. *van der Waals Layered Materials: Opportunities and Challenges*. ACS Nano, vol. 11, no. 12, pages 11803–11830, 2017. PMID: 29219304. (Cited on pages 2 and 9.)

[Eda 2011] Goki Eda, Hisato Yamaguchi, Damien Voiry, Takeshi Fujita, Mingwei Chen and Manish Chhowalla. *Photoluminescence from Chemically Exfoliated MoS2*. Nano Letters, vol. 11, no. 12, pages 5111–5116, 2011. (Cited on page 2.)

[Fallahazad 2016] Babak Fallahazad, Hema CP Movva, Kyounghwan Kim, Stefano Larentis, Takashi Taniguchi, Kenji Watanabe, Sanjay K Banerjee and Emanuel Tutuc. *Shubnikov–de Haas oscillations of high-mobility holes in monolayer and bilayer WSe 2: Landau level degeneracy, effective mass, and negative compressibility*. Physical Review Letters, vol. 116, no. 8, page 086601, 2016. (Cited on page 15.)

[Finkelstein 1995] Gleb Finkelstein, Hadas Shtrikman and Israel Bar-Joseph. *Optical Spectroscopy of a Two-Dimensional Electron Gas near the Metal-Insulator Transition*. Phys. Rev. Lett., vol. 74, pages 976–979, Feb 1995. (Cited on page 13.)

[Fox 2001] A.M. Fox and D.P.A.M. Fox. Optical properties of solids. Oxford master series in condensed matter physics. Oxford University Press, 2001. (Cited on page 8.)

[Gao 2017] Shiyuan Gao, Li Yang and Catalin D Spataru. *Interlayer coupling and gate-tunable excitons in transition metal dichalcogenide heterostructures*. Nano Letters, vol. 17, no. 12, pages 7809–7813, 2017. (Cited on page 57.)

[Geim 2013] Andre K Geim and Irina V Grigorieva. *Van der Waals heterostructures*. Nature, vol. 499, no. 7459, pages 419–425, 2013. (Cited on pages 2 and 15.)

[Gomes 2015] Lídia C. Gomes and A. Carvalho. *Phosphorene analogues: Isoelectronic two-dimensional group-IV monochalcogenides with orthorhombic structure.* Phys. Rev. B, vol. 92, page 085406, Aug 2015. (Cited on page 2.)

[Gutiérrez 2013] Humberto R Gutiérrez, Nestor Perea-López, Ana Laura Elías, Ayse Berkdemir, Bei Wang, Ruitao Lv, Florentino López-Urías, Vincent H Crespi, Humberto Terrones and Mauricio Terrones. *Extraordinary room-temperature photoluminescence in triangular WS2 monolayers.* Nano letters, vol. 13, no. 8, pages 3447–3454, 2013. (Cited on page 2.)

[Hanbicki 2018] Aubrey T Hanbicki, Hsun-Jen Chuang, Matthew R Rosenberger, C Stephen Hellberg, Saujan V Sivaram, Kathleen M McCreary, Igor I Mazin and Berend T Jonker. *Double Indirect Interlayer Exciton in a MoSe2/WSe2 van der Waals Heterostructure.* ACS Nano, vol. 12, no. 5, pages 4719–4726, 2018. (Cited on pages 38 and 57.)

[Heo 2015] Hoseok Heo, Ji Ho Sung, Soonyoung Cha, Bo-Gyu Jang, Joo-Youn Kim, Gangtae Jin, Donghun Lee, Ji-Hoon Ahn, Myoung-Jae Lee, Ji Hoon Shim*et al.* *Interlayer orientation-dependent light absorption and emission in monolayer semiconductor stacks.* Nature communications, vol. 6, no. 1, pages 1–7, 2015. (Cited on page 16.)

[Hsu 2014] Wei-Ting Hsu, Zi-Ang Zhao, Lain-Jong Li, Chang-Hsiao Chen, Ming-Hui Chiu, Pi-Shan Chang, Yi-Chia Chou and Wen-Hao Chang. *Second harmonic generation from artificially stacked transition metal dichalcogenide twisted bilayers.* ACS Nano, vol. 8, no. 3, pages 2951–2958, 2014. (Cited on pages 40 and 41.)

[Huard 2000] V Huard, RT Cox, K Saminadayar, A Arnoult and S Tatarenko. *Bound states in optical absorption of semiconductor quantum wells containing a two-dimensional electron gas.* Physical Review Letters, vol. 84, no. 1, page 187, 2000. (Cited on page 32.)

[Hunt 2013] B Hunt, JD Sanchez-Yamagishi, AF Young, M Yankowitz, Brian J LeRoy, K Watanabe, T Taniguchi, Pilkyung Moon, M Koshino, P Jarillo-Herrero and R C Ashoori. *Massive Dirac fermions and Hofstadter butterfly in a van der Waals heterostructure.* Science, vol. 340, no. 6139, pages 1427–1430, 2013. (Cited on page 17.)

[Huo 2017] Nengjie Huo, Yujue Yang and Jingbo Li. *Optoelectronics based on 2D TMDs and heterostructures.* Journal of Semiconductors, vol. 38, no. 3, page 031002, mar 2017. (Cited on page 2.)

[Island 2017] Joshua O Island, Aday J Molina-Mendoza, Mariam Barawi, Robert Biele, Eduardo Flores, José M Clamagirand, José R Ares, Carlos Sánchez, Herre S J van der Zant, Roberto D'Agosta, Isabel J Ferrer and Andres

Castellanos-Gomez. *Electronics and optoelectronics of quasi-1D layered transition metal trichalcogenides.* 2D Materials, vol. 4, no. 2, page 022003, apr 2017. (Cited on page 2.)

[Kang 2013] Jun Kang, Sefaattin Tongay, Jian Zhou, Jingbo Li and Junqiao Wu. *Band offsets and heterostructures of two-dimensional semiconductors.* Applied Physics Letters, vol. 102, no. 1, page 012111, 2013. (Cited on pages 15 and 16.)

[Keldysh 1979] L. V. Keldysh. *Coulomb interaction in thin semiconductor and semimetal films.* Soviet Journal of Experimental and Theoretical Physics Letters, vol. 29, page 658, June 1979. (Cited on page 10.)

[Kelly 2017] Adam G. Kelly, Toby Hallam, Claudia Backes, Andrew Harvey, Amir Sajad Esmaeily, Ian Godwin, João Coelho, Valeria Nicolosi, Jannika Lauth, Aditya Kulkarni, Sachin Kinge, Laurens D. A. Siebbeles, Georg S. Duesberg and Jonathan N. Coleman. *All-printed thin-film transistors from networks of liquid-exfoliated nanosheets.* Science, vol. 356, no. 6333, pages 69–73, 2017. (Cited on page 2.)

[Keyes 1953] R. W. Keyes. *The Electrical Properties of Black Phosphorus.* Physical Review, vol. 92, pages 580–584, 1953. (Cited on page 2.)

[Kheng 1993] K. Kheng, R. T. Cox, Merle Y. d' Aubigné, Franck Bassani, K. Saminadayar and S. Tatarenko. *Observation of negatively charged excitons X^- in semiconductor quantum wells.* Phys. Rev. Lett., vol. 71, pages 1752–1755, Sep 1993. (Cited on pages 12, 13 and 15.)

[Kioseoglou 2012] G. Kioseoglou, A. T. Hanbicki, M. Currie, A. L. Friedman, D. Gunlycke and B. T. Jonker. *Valley polarization and intervalley scattering in monolayer MoS2.* Applied Physics Letters, vol. 101, no. 22, page 221907, 2012. (Cited on pages 5 and 6.)

[Kioseoglou 2016] George Kioseoglou, Aubrey T Hanbicki, Marc Currie, Adam L Friedman and Berend T Jonker. *Optical polarization and intervalley scattering in single layers of MoS_2 and $MoSe_2$.* Scientific Reports, vol. 6, page 25041, 2016. (Cited on page 52.)

[Kobayashi 1995] Katsuyoshi Kobayashi and Jun Yamauchi. *Electronic structure and scanning-tunneling-microscopy image of molybdenum dichalcogenide surfaces.* Physical Review B, vol. 51, no. 23, page 17085, 1995. (Cited on page 4.)

[Komsa 2013] Hannu-Pekka Komsa and Arkady V Krasheninnikov. *Electronic structures and optical properties of realistic transition metal dichalcogenide heterostructures from first principles.* Physical Review B, vol. 88, no. 8, page 085318, 2013. (Cited on page 16.)

[Koperski 2018] Maciej Koperski, Maciej R Molas, Ashish Arora, Karol Nogajewski, Miroslav Bartos, Jan Wyzula, Diana Vaclavkova, Piotr Kossacki and Marek Potemski. *Orbital, spin and valley contributions to Zeeman splitting of excitonic resonances in $MoSe_2$, WSe_2 and WS_2 Monolayers.* 2D Materials, vol. 6, no. 1, page 015001, 2018. (Cited on pages 54, 55 and 57.)

[Kozawa 2014] Daichi Kozawa, Rajeev Kumar, Alexandra Carvalho, Kiran Kumar Amara, Weijie Zhao, Shunfeng Wang, Minglin Toh, Ricardo M. Ribeiro, A. H. Castro Neto, Kazunari Matsuda and Goki Eda. *Photocarrier relaxation pathway in two-dimensional semiconducting transition metal dichalcogenides.* Nature Communications, vol. 5, no. 1, page 4543, July 2014. (Cited on page 11.)

[Kuc 2015] Agnieszka Kuc and Thomas Heine. *The electronic structure calculations of two-dimensional transition-metal dichalcogenides in the presence of external electric and magnetic fields.* Chem. Soc. Rev., vol. 44, pages 2603–2614, 2015. (Cited on page 3.)

[Kunstmann 2018] Jens Kunstmann, Fabian Mooshammer, Philipp Nagler, Andrey Chaves, Frederick Stein, Nicola Paradiso, Gerd Plechinger, Christoph Strunk, Christian Schüller, Gotthard Seifert, David R Reichman and Tobias Korn. *Momentum-space indirect interlayer excitons in transition metal dichalcogenide van der Waals heterostructures.* Nature Physics, vol. 14, no. 7, pages 801–805, 2018. (Cited on page 51.)

[Lagarde 2014a] D. Lagarde, L. Bouet, X. Marie, C. R. Zhu, B. L. Liu, T. Amand, P. H. Tan and B. Urbaszek. *Carrier and polarization dynamics in monolayer MoS_2.* Physical Review Letters, vol. 112, no. 4, page 047401, 2014. (Cited on page 16.)

[Lagarde 2014b] D Lagarde, L Bouet, X Marie, CR Zhu, BL Liu, T Amand, PH Tan and B Urbaszek. *Carrier and polarization dynamics in monolayer MoS 2.* Physical Review Letters, vol. 112, no. 4, page 047401, 2014. (Cited on page 32.)

[Lampert 1958] Murray A Lampert. *Mobile and immobile effective-mass-particle complexes in nonmetallic solids.* Physical Review Letters, vol. 1, no. 12, page 450, 1958. (Cited on page 12.)

[Laturia 2018] Akash Laturia, Maarten L Van de Put and William G Vandenberghe. *Dielectric properties of hexagonal boron nitride and transition metal dichalcogenides: from monolayer to bulk.* npj 2D Materials and Applications, vol. 2, no. 1, page 6, 2018. (Cited on page 46.)

[Lee 2016] Youngbin Lee, Jaehyun Yang, Dain Lee, Yong-Hoon Kim, Jin-Hong Park, Hyoungsub Kim and Jeong Ho Cho. *Trap-induced photoresponse of*

solution-synthesized MoS 2. Nanoscale, vol. 8, no. 17, pages 9193–9200, 2016. (Cited on page 35.)

[Li 2014a] Yilei Li, Jonathan Ludwig, Tony Low, Alexey Chernikov, Xu Cui, Ghidewon Arefe, Young Duck Kim, Arend M Van Der Zande, Albert Rigosi, Heather M Hill, Suk H. Kim, James Hone, Zhiqiang Li, Dmitry Smirnov and Tony F. Neinz. *Valley splitting and polarization by the Zeeman effect in monolayer $MoSe_2$*. Physical Review Letters, vol. 113, no. 26, page 266804, 2014. (Cited on pages 57 and 58.)

[Li 2014b] Yilei Li, Jonathan Ludwig, Tony Low, Alexey Chernikov, Xu Cui, Ghidewon Arefe, Young Duck Kim, Arend M. van der Zande, Albert Rigosi, Heather M. Hill, Suk Hyun Kim, James Hone, Zhiqiang Li, Dmitry Smirnov and Tony F. Heinz. *Valley Splitting and Polarization by the Zeeman Effect in Monolayer $MoSe_2$*. Phys. Rev. Lett., vol. 113, page 266804, Dec 2014. (Cited on pages 53, 54 and 58.)

[Li 2018] Liang Li, Weike Wang, Penglai Gong, Xiangde Zhu, Bei Deng, Xingqiang Shi, Guoying Gao, Huiqiao Li and Tianyou Zhai. *2D GeP: An Unexploited Low-Symmetry Semiconductor with Strong In-Plane Anisotropy*. Advanced Materials, vol. 30, no. 14, page 1706771, 2018. (Cited on page 2.)

[Li 2019] Zhipeng Li, Tianmeng Wang, Chenhao Jin, Zhengguang Lu, Zhen Lian, Yuze Meng, Mark Blei, Shiyuan Gao, Takashi Taniguchi, Kenji Watanabe, Tianhui Ren, Sefaattin Tongay, Li Yang, Dmitry Smirnov, Ting Cao and Su-Fei Shi. *Emerging photoluminescence from the dark-exciton phonon replica in monolayer WSe_2*. Nature Communications, vol. 10, no. 1, page 2469, 2019. (Cited on pages 57 and 58.)

[Liu 2013a] Gui-Bin Liu, Wen-Yu Shan, Yugui Yao, Wang Yao and Di Xiao. *Three-band tight-binding model for monolayers of group-VIB transition metal dichalcogenides*. Phys. Rev. B, vol. 88, page 085433, Aug 2013. (Cited on pages 4, 5 and 11.)

[Liu 2013b] Gui-Bin Liu, Wen-Yu Shan, Yugui Yao, Wang Yao and Di Xiao. *Three-band tight-binding model for monolayers of group-VIB transition metal dichalcogenides*. Physical Review B, vol. 88, no. 8, page 085433, 2013. (Cited on page 53.)

[Liu 2014] Han Liu, Adam T. Neal, Zhen Zhu, Zhe Luo, Xianfan Xu, David Tománek and Peide D. Ye. *Phosphorene: An Unexplored 2D Semiconductor with a High Hole Mobility*. ACS Nano, vol. 8, no. 4, pages 4033–4041, 2014. (Cited on pages 2 and 11.)

[Liu 2015] Gui-Bin Liu, Di Xiao, Yugui Yao, Xiaodong Xu and Wang Yao. *Electronic structures and theoretical modelling of two-dimensional group-VIB*

transition metal dichalcogenides. Chemical Society Reviews, vol. 44, no. 9, pages 2643–2663, 2015. (Cited on page 57.)

[Lloyd 2016] David Lloyd, Xinghui Liu, Jason W Christopher, Lauren Cantley, Anubhav Wadehra, Brian L Kim, Bennett B Goldberg, Anna K Swan and J Scott Bunch. *Band gap engineering with ultralarge biaxial strains in suspended monolayer MoS2*. Nano Letters, vol. 16, no. 9, pages 5836–5841, 2016. (Cited on page 27.)

[Lu 2014] Chih-Pin Lu, Guohong Li, Jinhai Mao, Li-Min Wang and Eva Y Andrei. *Bandgap, mid-gap states, and gating effects in MoS2*. Nano Letters, vol. 14, no. 8, pages 4628–4633, 2014. (Cited on page 32.)

[Lu 2019] Xiaobo Lu, Xiaoqin Li and Li Yang. *Modulated interlayer exciton properties in a two-dimensional moiré crystal*. Physical Review B, vol. 100, no. 15, page 155416, 2019. (Cited on page 39.)

[Lyons 2019] T. P. Lyons, S. Dufferwiel, M. Brooks, F. Withers, T. Taniguchi, K. Watanabe, K. S. Novoselov, G. Burkard and A. I. Tartakovskii. *The valley Zeeman effect in inter- and intra-valley trions in monolayer WSe2*. Nature Communications, vol. 10, no. 1, page 2330, May 2019. (Cited on page 14.)

[Lédée 2017] Ferdinand Lédée, Gaëlle Trippé-Allard, Hiba Diab, Pierre Audebert, Damien Garrot, Jean-Sébastien Lauret and Emmanuelle Deleporte. *Fast growth of monocrystalline thin films of 2D layered hybrid perovskite*. CrystEngComm, vol. 19, pages 2598–2602, 2017. (Cited on page 2.)

[MacNeill 2015] David MacNeill, Colin Heikes, Kin Fai Mak, Zachary Anderson, Andor Kormányos, Viktor Zólyomi, Jiwoong Park and Daniel C. Ralph. *Breaking of Valley Degeneracy by Magnetic Field in Monolayer $MoSe_2$*. Phys. Rev. Lett., vol. 114, page 037401, Jan 2015. (Cited on pages 53, 54, 55, 57 and 58.)

[Mak 2010] Kin Fai Mak, Changgu Lee, James Hone, Jie Shan and Tony F Heinz. *Atomically thin MoS 2: a new direct-gap semiconductor*. Physical review letters, vol. 105, no. 13, page 136805, 2010. (Cited on pages 2 and 4.)

[Mak 2012] Kin Fai Mak, Keliang He, Jie Shan and Tony F Heinz. *Control of valley polarization in monolayer MoS_2 by optical helicity*. Nature Nanotechnology, vol. 7, no. 8, pages 494–498, 2012. (Cited on pages 5, 6, 16 and 54.)

[Mak 2013] Kin Fai Mak, Keliang He, Changgu Lee, Gwan Hyoung Lee, James Hone, Tony F Heinz and Jie Shan. *Tightly bound trions in monolayer MoS 2*. Nature materials, vol. 12, no. 3, pages 207–211, 2013. (Cited on page 13.)

[Manca 2017] M Manca, MM Glazov, C Robert, F Cadiz, T Taniguchi, K Watanabe, E Courtade, T Amand, P Renucci, X Marie, G Wang and B Urbaszek.

Enabling valley selective exciton scattering in monolayer WSe_2 through upconversion. Nature Communications, vol. 8, page 14927, 2017. (Cited on page 15.)

[Miller 2017] Bastian Miller, Alexander Steinhoff, Borja Pano, Julian Klein, Frank Jahnke, Alexander Holleitner and Ursula Wurstbauer. *Long-lived direct and indirect interlayer excitons in van der Waals heterostructures.* Nano Letters, vol. 17, no. 9, pages 5229–5237, 2017. (Cited on page 51.)

[Mitioglu 2013] AA Mitioglu, P Plochocka, JN Jadczak, W Escoffier, GLJA Rikken, L Kulyuk and DK Maude. *Optical manipulation of the exciton charge state in single-layer tungsten disulfide.* Physical Review B, vol. 88, no. 24, page 245403, 2013. (Cited on page 32.)

[Mitioglu 2015] A. A. Mitioglu, P. Plochocka, A. Granados del Aguila, P. C. M. Christianen, G. Deligeorgis, S. Anghel, L. Kulyuk and D. K. Maude. *Optical Investigation of Monolayer and Bulk Tungsten Diselenide (WSe2) in High Magnetic Fields.* Nano Letters, vol. 15, no. 7, pages 4387–4392, 2015. PMID: 26065723. (Cited on pages 53, 54 and 55.)

[Mitioglu 2016] AA Mitioglu, K Galkowski, A Surrente, L Klopotowski, D Dumcenco, A Kis, DK Maude and P Plochocka. *Magnetoexcitons in large area CVD-grown monolayer MoS_2 and $MoSe_2$ on sapphire.* Physical Review B, vol. 93, no. 16, page 165412, 2016. (Cited on page 57.)

[Mitioglu 2018] A Mitioglu, J Buhot, MV Ballottin, S Anghel, K Sushkevich, L Kulyuk and PCM Christianen. *Observation of bright exciton splitting in strained WSe_2 monolayers.* Physical Review B, vol. 98, no. 23, page 235429, 2018. (Cited on pages 55 and 57.)

[Movva 2017] Hema CP Movva, Babak Fallahazad, Kyounghwan Kim, Stefano Larentis, Takashi Taniguchi, Kenji Watanabe, Sanjay K Banerjee and Emanuel Tutuc. *Density-Dependent Quantum Hall States and Zeeman Splitting in Monolayer and Bilayer WSe_2.* Physical Review Letters, vol. 118, no. 24, page 247701, 2017. (Cited on page 15.)

[Nayak 2017] Pramoda K Nayak, Yevhen Horbatenko, Seongjoon Ahn, Gwangwoo Kim, Jae-Ung Lee, Kyung Yeol Ma, A-Rang Jang, Hyunseob Lim, Dogyeong Kim, Sunmin Ryu, Hyeonsik Cheong, Noejung Park and Hyeon Suk Shin. *Probing evolution of twist-angle-dependent interlayer excitons in MoSe2/WSe2 van der Waals heterostructures.* ACS Nano, vol. 11, no. 4, pages 4041–4050, 2017. (Cited on page 16.)

[Neumann 2017] Andre Neumann, Jessica Lindlau, Léo Colombier, Manuel Nutz, Sina Najmaei, Jun Lou, Aditya D Mohite, Hisato Yamaguchi and Alexander Högele. *Opto-valleytronic imaging of atomically thin semiconductors.* Nature nanotechnology, vol. 12, no. 4, page 329, 2017. (Cited on page 54.)

[Novoselov 2004] Kostya S Novoselov, Andre K Geim, Sergei V Morozov, D Jiang, Y_ Zhang, Sergey V Dubonos, Irina V Grigorieva and Alexandr A Firsov. *Electric field effect in atomically thin carbon films*. science, vol. 306, no. 5696, pages 666–669, 2004. (Cited on page 2.)

[Novoselov 2016] KS Novoselov, A Mishchenko, A Carvalho and AH Castro Neto. *2D materials and van der Waals heterostructures*. Science, vol. 353, no. 6298, page aac9439, 2016. (Cited on pages 2 and 15.)

[Pan 2018] Yi Pan, Stefan Fölsch, Yifan Nie, Dacen Waters, Yu-Chuan Lin, Bhakti Jariwala, Kehao Zhang, Kyeongjae Cho, Joshua A Robinson and Randall M Feenstra. *Quantum-Confined Electronic States arising from Moiré Pattern of MoS_2-WSe_2 Heterobilayers*. Nano Letters, vol. 18, no. 3, pages 1849–1855, 2018. (Cited on page 37.)

[Park 2008] Cheol-Hwan Park, Li Yang, Young-Woo Son, Marvin L Cohen and Steven G Louie. *Anisotropic behaviours of massless Dirac fermions in graphene under periodic potentials*. Nature Physics, vol. 4, no. 3, pages 213–217, 2008. (Cited on page 17.)

[Pelant 2012] Ivan Pelant and Jan Valenta. Luminescence spectroscopy of semiconductors. Oxford University Press, 2012. (Cited on pages 6 and 7.)

[Plechinger 2016a] Gerd Plechinger, Philipp Nagler, Ashish Arora, Andrés Granados del Águila, Mariana V Ballottin, Tobias Frank, Philipp Steinleitner, Martin Gmitra, Jaroslav Fabian, Peter CM Christianen, Rudolf Bratschitsch, Christian Schüller and Tobias Korn. *Excitonic valley effects in monolayer WS_2 under high magnetic fields*. Nano Letters, vol. 16, no. 12, pages 7899–7904, 2016. (Cited on pages 54, 57 and 58.)

[Plechinger 2016b] Gerd Plechinger, Philipp Nagler, Ashish Arora, Robert Schmidt, Alexey Chernikov, Andrés Granados del Águila, Peter C. M. Christianen, Rudolf Bratschitsch, Christian Schüller and Tobias Korn. *Trion fine structure and coupled spin-valley dynamics in monolayer tungsten disulfide*. Nature Communications, vol. 7, no. 1, page 12715, September 2016. (Cited on page 14.)

[Ponomarenko 2013] LA Ponomarenko, RV Gorbachev, GL Yu, DC Elias, R Jalil, AA Patel, A Mishchenko, AS Mayorov, CR Woods, JR Wallbank, M Mucha-Kruszynski, B A Piot, M Potemski, I V Grigorieva, K S Novoselov, F Guinea, V I Falko and Geim A K. *Cloning of Dirac fermions in graphene superlattices*. Nature, vol. 497, no. 7451, pages 594–597, 2013. (Cited on page 17.)

[Prada 2015] Elsa Prada, J. V. Alvarez, K. L. Narasimha-Acharya, F. J. Bailen and J. J. Palacios. *Effective-mass theory for the anisotropic exciton in two-dimensional crystals: Application to phosphorene*. Phys. Rev. B, vol. 91, page 245421, Jun 2015. (Cited on page 10.)

[Pumera 2017] Martin Pumera and Zdeněk Sofer. *2D Monoelemental Arsenene, Antimonene, and Bismuthene: Beyond Black Phosphorus.* Advanced Materials, vol. 29, no. 21, page 1605299, 2017. (Cited on page 2.)

[Radisavljevic 2011] B. Radisavljevic, A. Radenovic, J. Brivio, V. Giacometti and A. Kis. *Single-layer MoS2 transistors.* Nature Nanotechnology, vol. 6, no. 3, pages 147–150, March 2011. (Cited on page 2.)

[Raja 2017] Archana Raja, Andrey Chaves, Jaeeun Yu, Ghidewon Arefe, Heather M Hill, Albert F Rigosi, Timothy C Berkelbach, Philipp Nagler, Christian Schüller, Tobias Korn, Colin Nuckolls, Jamnes Hone, Louis E Brus, Tony F Heinz, David R Reichman and Alexey Chernikov. *Coulomb engineering of the bandgap and excitons in two-dimensional materials.* Nature Communications, vol. 8, page 15251, 2017. (Cited on pages 9, 15 and 46.)

[Ramasubramaniam 2012] Ashwin Ramasubramaniam. *Large excitonic effects in monolayers of molybdenum and tungsten dichalcogenides.* Phys. Rev. B, vol. 86, page 115409, Sep 2012. (Cited on pages 4 and 5.)

[Rivera 2015] Pasqual Rivera, John R. Schaibley, Aaron M. Jones, Jason S. Ross, Sanfeng Wu, Grant Aivazian, Philip Klement, Kyle Seyler, Genevieve Clark, Nirmal J. Ghimire, Jiaqiang Yan, D. G. Mandrus, Wang Yao and Xiaodong Xu. *Observation of long-lived interlayer excitons in monolayer $MoSe_2$-WSe_2 heterostructures.* Nature Communications, vol. 6, page 6242, 2015. (Cited on page 16.)

[Rivera 2016] Pasqual Rivera, Kyle L. Seyler, Hongyi Yu, John R. Schaibley, Jiaqiang Yan, David G. Mandrus, Wang Yao and Xiaodong Xu. *Valley-polarized exciton dynamics in a 2D semiconductor heterostructure.* Science, vol. 351, no. 6274, pages 688–691, 2016. (Cited on page 16.)

[Robert 2016] C. Robert, D. Lagarde, F. Cadiz, G. Wang, B. Lassagne, T. Amand, A. Balocchi, P. Renucci, S. Tongay, B. Urbaszek and X. Marie. *Exciton radiative lifetime in transition metal dichalcogenide monolayers.* Physical Review B, vol. 93, no. 20, page 205423, 2016. (Cited on page 16.)

[Robert 2018] C Robert, MA Semina, F Cadiz, M Manca, E Courtade, T Taniguchi, K Watanabe, H Cai, S Tongay, B Lassagne, P Renucci, T Amand, X Marie, M M Glazov and B Urbaszek. *Optical spectroscopy of excited exciton states in MoS_2 monolayers in van der Waals heterostructures.* Physical Review Materials, vol. 2, no. 1, page 011001, 2018. (Cited on page 15.)

[Roldán 2015] Rafael Roldán, Andrés Castellanos-Gomez, Emmanuele Cappelluti and Francisco Guinea. *Strain engineering in semiconducting two-dimensional crystals.* Journal of physics. Condensed matter : an Institute of Physics journal, vol. 27, no. 31, page 313201, August 2015. (Cited on page 2.)

[Rose 2013] Félix Rose, M. O. Goerbig and Frédéric Piéchon. *Spin- and valley-dependent magneto-optical properties of MoS_2*. Phys. Rev. B, vol. 88, page 125438, Sep 2013. (Cited on page 53.)

[Rosenberger 2020] Matthew R Rosenberger, Hsun-Jen Chuang, Madeleine Phillips, Vladimir P Oleshko, Kathleen M McCreary, Saujan V Sivaram, C Stephen Hellberg and Berend T Jonker. *Twist Angle-Dependent Atomic Reconstruction and Moiré Patterns in Transition Metal Dichalcogenide Heterostructures*. ACS nano, vol. 14, no. 4, pages 4550–4558, 2020. (Cited on page 39.)

[Ross 2013] Jason S Ross, Sanfeng Wu, Hongyi Yu, Nirmal J Ghimire, Aaron M Jones, Grant Aivazian, Jiaqiang Yan, David G Mandrus, Di Xiao, Wang Yao*et al.* *Electrical control of neutral and charged excitons in a monolayer semiconductor*. Nature communications, vol. 4, no. 1, pages 1–6, 2013. (Cited on page 55.)

[Ross 2017] Jason S Ross, Pasqual Rivera, John Schaibley, Eric Lee-Wong, Hongyi Yu, Takashi Taniguchi, Kenji Watanabe, Jiaqiang Yan, David Mandrus, David Cobden*et al.* *Interlayer exciton optoelectronics in a 2D heterostructure p–n junction*. Nano letters, vol. 17, no. 2, pages 638–643, 2017. (Cited on pages 16 and 33.)

[Rytova 1967] N S. Rytova. *The screened potential of a point charge in a thin film*. Moscow University Physics Bulletin, vol. 3, no. 3, page 18, 1967. (Cited on page 10.)

[Shields 1995] A.J. Shields, J.L. Osborne, M.Y. Simmons, M. Pepper and D.A. Ritchie. *Magneto-optical spectroscopy of positively charged excitons in GaAs quantum wells*. Phys. Rev. B, vol. 52, pages R5523–R5526, Aug 1995. (Cited on page 13.)

[Silva-Guillén 2017] J A Silva-Guillén, E Canadell, P Ordejón, F Guinea and R Roldán. *Anisotropic features in the electronic structure of the two-dimensional transition metal trichalcogenide TiS3: electron doping and plasmons*. 2D Materials, vol. 4, no. 2, page 025085, may 2017. (Cited on page 2.)

[Singh 2016] Akshay Singh, Galan Moody, Kha Tran, Marie E Scott, Vincent Overbeck, Gunnar Berghäuser, John Schaibley, Edward J Seifert, Dennis Pleskot, Nathaniel M Gabor, Jiaqiang Yan, David G Madrus, Marten Richter, Ermin Malic, Xiaodong Xu and Xiaoqin Li. *Trion formation dynamics in monolayer transition metal dichalcogenides*. Physical Review B, vol. 93, no. 4, page 041401, 2016. (Cited on page 32.)

[Splendiani 2010] Andrea Splendiani, Liang Sun, Yuanbo Zhang, Tianshu Li, Jonghwan Kim, Chi-Yung Chim, Giulia Galli and Feng Wang. *Emerging*

photoluminescence in monolayer MoS2. Nano letters, vol. 10, no. 4, pages 1271–1275, 2010. (Cited on pages 2 and 4.)

[Srivastava 2015a] Ajit Srivastava, Meinrad Sidler, Adrien V Allain, Dominik S Lembke, Andras Kis and A Imamoğlu. *Optically active quantum dots in monolayer WSe 2*. Nature Nanotechnology, vol. 10, no. 6, page 491, 2015. (Cited on page 32.)

[Srivastava 2015b] Ajit Srivastava, Meinrad Sidler, Adrien V. Allain, Dominik S. Lembke, Andras Kis and A. Imamoglu. *Valley Zeeman effect in elementary optical excitations of monolayer WSe2*. Nature Physics, vol. 11, no. 2, pages 141–147, February 2015. (Cited on pages 53, 54, 57 and 58.)

[Stier 2016a] Andreas V Stier, Kathleen M McCreary, Berend T Jonker, Junichiro Kono and Scott A Crooker. *Exciton diamagnetic shifts and valley Zeeman effects in monolayer WS_2 and MoS_2 to 65 Tesla*. Nature Communications, vol. 7, page 10643, 2016. (Cited on page 57.)

[Stier 2016b] Andreas V Stier, Nathan P Wilson, Genevieve Clark, Xiaodong Xu and Scott A Crooker. *Probing the influence of dielectric environment on excitons in monolayer WSe_2: insight from high magnetic fields*. Nano Letters, vol. 16, no. 11, pages 7054–7060, 2016. (Cited on page 50.)

[Stier 2018] Andreas V Stier, Nathan P Wilson, Kirill A Velizhanin, Junichiro Kono, Xiaodong Xu and Scott A Crooker. *Magnetooptics of exciton Rydberg states in a monolayer semiconductor*. Physical Review Letters, vol. 120, no. 5, page 057405, 2018. (Cited on pages 15, 39 and 50.)

[Surrente 2017] Alessandro Surrente, Dumitru Dumcenco, Zhuo Yang, Agnieszka Kuc, Yu Jing, Thomas Heine, Yen-Cheng Kung, Duncan K Maude, Andras Kis and Paulina Plochocka. *Defect healing and charge transfer-mediated valley polarization in MoS2/MoSe2/MoS2 trilayer van der Waals heterostructures*. Nano letters, vol. 17, no. 7, pages 4130–4136, 2017. (Cited on pages 34, 44, 48 and 52.)

[Surrente 2018] A. Surrente, Ł. Klopotowski, N. Zhang, M. Baranowski, A. Mitioglu, M. V. Ballottin, P. CM Christianen, D. Dumcenco, Y.-C. Kung, D. K. Maude, A. Kis and P. Plochocka. *Intervalley Scattering of Interlayer Excitons in a $MoS_2/MoSe_2/MoS_2$ Heterostructure in High Magnetic Field*. Nano Letters, vol. 18, no. 6, pages 3994–4000, 2018. (Cited on pages 38 and 44.)

[Thomas 1977] G.A. Thomas and T.M. Rice. *Trions, molecules and excitons above the Mott density in Ge*. Solid State Communications, vol. 23, no. 6, pages 359 – 363, 1977. (Cited on page 12.)

[Thygesen 2017] Kristian Sommer Thygesen. *Calculating excitons, plasmons, and quasiparticles in 2D materials and van der Waals heterostructures.* 2D Materials, vol. 4, no. 2, page 022004, jun 2017. (Cited on page 9.)

[Toh 2017] Rou Jun Toh, Zdeněk Sofer, Jan Luxa, David Sedmidubský and Martin Pumera. *3R phase of MoS2 and WS2 outperforms the corresponding 2H phase for hydrogen evolution.* Chem. Commun., vol. 53, pages 3054–3057, 2017. (Cited on page 3.)

[Tongay 2013a] Sefaattin Tongay, Jian hou, Can Ataca, Jonathan Liu, Jeong Seuk Kang, Tyler S Matthews, Long You, Jingbo Li, Jeffrey C Grossman and Junqiao Wu. *Broad-range modulation of light emission in two-dimensional semiconductors by molecular physisorption gating.* Nano letters, vol. 13, no. 6, pages 2831–2836, 2013. (Cited on page 30.)

[Tongay 2013b] Sefaattin Tongay, Joonki Suh, Can Ataca, Wen Fan, Alexander Luce, Jeong Seuk Kang, Jonathan Liu, Changhyun Ko, Rajamani Raghunathanan, Jian Zhou, Frank Ogletree, Jingbo Li, Jeffrey C Grossman and Junqiao Wu. *Defects activated photoluminescence in two-dimensional semiconductors: interplay between bound, charged, and free excitons.* Scientific Reports, vol. 3, page 2657, 2013. (Cited on page 34.)

[Tonndorf 2013] Philipp Tonndorf, Robert Schmidt, Philipp Böttger, Xiao Zhang, Janna Börner, Andreas Liebig, Manfred Albrecht, Christian Kloc, Ovidiu Gordan, Dietrich R. T. Zahn, Steffen Michaelis de Vasconcellos and Rudolf Bratschitsch. *Photoluminescence emission and Raman response of monolayer MoS2, MoSe2, and WSe2.* Opt. Express, vol. 21, no. 4, pages 4908–4916, Feb 2013. (Cited on page 4.)

[Tornatzky 2018] Hans Tornatzky, Anne-Marie Kaulitz and Janina Maultzsch. *Resonance Profiles of Valley Polarization in Single-Layer MoS_2 and $MoSe_2$.* Physical Review Letters, vol. 121, no. 16, page 167401, 2018. (Cited on page 56.)

[Tran 2014] Vy Tran, Ryan Soklaski, Yufeng Liang and Li Yang. *Layer-controlled band gap and anisotropic excitons in few-layer black phosphorus.* Physical Review B, vol. 89, page 235319, 2014. (Cited on page 2.)

[Tran 2018] Kha Tran, Galan Moody, Fengcheng Wu, Xiaobo Lu, Junho Choi, Akshay Singh, Jacob Embley, André Zepeda, Marshall Campbell, Kyounghwan Kim, Amritesh Rai, Travis Autry, Daniel A Sanchez, Takashi Taniguchi, Kenki Watanabe, Nanshu Lu, Sanjay K Banerjee, Emanuel Tutuc, Li Yang, Allan H MacDonal, Kevin L Silverman and Xiaoqin Li. *Moiré Excitons in Van der Waals Heterostructures.* arXiv preprint arXiv:1807.03771, 2018. (Cited on pages 49 and 50.)

[Wang 2012] Qing Hua Wang, Kourosh Kalantar-Zadeh, Andras Kis, Jonathan N Coleman and Michael S Strano. *Electronics and optoelectronics of two-dimensional transition metal dichalcogenides.* Nature Nanotechnology, vol. 7, no. 11, pages 699–712, 2012. (Cited on pages 2 and 16.)

[Wang 2014] G. Wang, L. Bouet, D. Lagarde, M. Vidal, A. Balocchi, T. Amand, X. Marie and B. Urbaszek. *Valley dynamics probed through charged and neutral exciton emission in monolayer WSe_2.* Physical Review B, vol. 90, no. 7, page 075413, 2014. (Cited on page 16.)

[Wang 2015a] G. Wang, L. Bouet, M. M. Glazov, T .Amand, E. L. Ivchenko, E. Palleau, X. Marie and B. Urbaszek. *Magneto-optics in transition metal diselenide monolayers.* 2D Materials, vol. 2, no. 3, page 034002, 2015. (Cited on pages 53, 54, 55, 57 and 58.)

[Wang 2015b] G. Wang, E. Palleau, T. Amand, S. Tongay, X. Marie and B. Urbaszek. *Polarization and time-resolved photoluminescence spectroscopy of excitons in $MoSe_2$ monolayers.* Applied Physics Letters, vol. 106, no. 11, page 112101, mar 2015. (Cited on page 16.)

[Wang 2015c] G Wang, E Palleau, T Amand, S Tongay, X Marie and B Urbaszek. *Polarization and time-resolved photoluminescence spectroscopy of excitons in MoSe2 monolayers.* Applied Physics Letters, vol. 106, no. 11, page 112101, 2015. (Cited on page 52.)

[Wang 2016a] Eryin Wang, Xiaobo Lu, Shijie Ding, Wei Yao, Mingzhe Yan, Guoliang Wan, Ke Deng, Shuopei Wang, Guorui Chen, Liguo Ma, Jeil Jung, Alexei V Fedorov, Yuanbo Zhang, Guangyu Zhang and Shuyun Zhou. *Gaps induced by inversion symmetry breaking and second-generation Dirac cones in graphene/hexagonal boron nitride.* Nature Physics, vol. 12, no. 12, pages 1111–1115, 2016. (Cited on page 17.)

[Wang 2016b] Kai Wang, Bing Huang, Mengkun Tian, Frank Ceballos, Ming-Wei Lin, Masoud Mahjouri-Samani, Abdelaziz Boulesbaa, Alexander A Puretzky, Christopher M Rouleau, Mina Yoon, Hui Zhao, Kai Xiao, Gerd Duscher and David B Geohegan. *Interlayer coupling in twisted WSe_2/WS_2 bilayer heterostructures revealed by optical spectroscopy.* ACS Nano, vol. 10, no. 7, pages 6612–6622, 2016. (Cited on page 44.)

[Wang 2017] Yong Wang, Zhan Wang, Wang Yao, Gui-Bin Liu and Hongyi Yu. *Interlayer coupling in commensurate and incommensurate bilayer structures of transition-metal dichalcogenides.* Physical Review B, vol. 95, no. 11, page 115429, 2017. (Cited on page 16.)

[Wilson 2017] Neil R Wilson, Paul V Nguyen, Kyle Seyler, Pasqual Rivera, Alexander J Marsden, Zachary PL Laker, Gabriel C Constantinescu, Viktor Kandyba, Alexei Barinov, Nicholas DM Hine*et al.* *Determination of band*

offsets, hybridization, and exciton binding in 2D semiconductor heterostructures. Science advances, vol. 3, no. 2, page e1601832, 2017. (Cited on page 16.)

[Wu 2016] Zefei Wu, Shuigang Xu, Huanhuan Lu, Armin Khamoshi, Gui-Bin Liu, Tianyi Han, Yingying Wu, Jiangxiazi Lin, Gen Long, Yuheng He, Yuheng He, Yuan Cai, Yugui Yao, Fan Zhang and Ning Wang. *Even–odd layer-dependent magnetotransport of high-mobility Q-valley electrons in transition metal disulfides.* Nature Communications, vol. 7, page 12955, 2016. (Cited on page 15.)

[Wu 2017a] Fengcheng Wu, Timothy Lovorn and A. H. Macdonald. *Topological Exciton Bands in Moiré Heterojunctions.* Physical Review Letters, vol. 118, no. 14, page 147401, 2017. (Cited on pages 17, 38, 40, 45 and 46.)

[Wu 2017b] Fengcheng Wu, Timothy Lovorn and Allan H MacDonald. *Topological exciton bands in moiré heterojunctions.* Physical Review Letters, vol. 118, no. 14, page 147401, 2017. (Cited on page 57.)

[Wu 2018] Fengcheng Wu, Timothy Lovorn and AH MacDonald. *Theory of optical absorption by interlayer excitons in transition metal dichalcogenide heterobilayers.* Physical Review B, vol. 97, no. 3, page 035306, 2018. (Cited on pages 17, 45 and 52.)

[Xiao 2012] Di Xiao, Gui-Bin Liu, Wanxiang Feng, Xiaodong Xu and Wang Yao. *Coupled spin and valley physics in monolayers of MoS 2 and other group-VI dichalcogenides.* Physical review letters, vol. 108, no. 19, page 196802, 2012. (Cited on pages 5, 6, 16 and 53.)

[Xiao 2017] Jun Xiao, Mervin Zhao, Yuan Wang and Xiang Zhang. *Excitons in atomically thin 2D semiconductors and their applications.* Nanophotonics, vol. 6, no. 6, pages 1309–1328, 2017. (Cited on page 9.)

[Xu 2014] Xiaodong Xu, Wang Yao, Di Xiao and Tony F Heinz. *Spin and pseudospins in layered transition metal dichalcogenides.* Nature Physics, vol. 10, no. 5, pages 343–350, 2014. (Cited on page 16.)

[Xu 2017] Shuigang Xu, Junying Shen, Gen Long, Zefei Wu, Zhi-qiang Bao, Cheng-Cheng Liu, Xiao Xiao, Tianyi Han, Jiangxiazi Lin, Yingying Wu, Huanhuan Lu, Jianqiang Hou, Liheng An, Yuanwei Wang, Yuan Cai, K M Ho, Yuheng He, Rolf Lortz, Fan Zhang and Ning Wang. *Odd-Integer Quantum Hall States and Giant Spin Susceptibility in p-Type Few-Layer WSe_2.* Physical Review Letters, vol. 118, no. 6, page 067702, 2017. (Cited on page 15.)

[Xue 2011] Jiamin Xue, Javier Sanchez-Yamagishi, Danny Bulmash, Philippe Jacquod, Aparna Deshpande, K Watanabe, T Taniguchi, Pablo Jarillo-Herrero and Brian J LeRoy. *Scanning tunnelling microscopy and spec-*

troscopy of ultra-flat graphene on hexagonal boron nitride. Nature Materials, vol. 10, no. 4, pages 282–285, 2011. (Cited on page 17.)

[Yankowitz 2012] Matthew Yankowitz, Jiamin Xue, Daniel Cormode, Javier D Sanchez-Yamagishi, K Watanabe, T Taniguchi, Pablo Jarillo-Herrero, Philippe Jacquod and Brian J LeRoy. *Emergence of superlattice Dirac points in graphene on hexagonal boron nitride*. Nature Physics, vol. 8, no. 5, pages 382–386, 2012. (Cited on page 17.)

[Yu 2014] Hongyi Yu, Gui-Bin Liu, Pu Gong, Xiaodong Xu and Wang Yao. *Dirac cones and Dirac saddle points of bright excitons in monolayer transition metal dichalcogenides*. Nature Communications, vol. 5, no. 1, page 3876, May 2014. (Cited on page 14.)

[Yu 2017] Hongyi Yu, Gui-Bin Liu, Jianju Tang, Xiaodong Xu and Wang Yao. *Moiré excitons: From programmable quantum emitter arrays to spin-orbit–coupled artificial lattices*. Science Advances, vol. 3, no. 11, page e1701696, 2017. (Cited on pages 17, 37, 38, 40, 45, 46, 48, 49, 51 and 52.)

[Zaitsev 2007] SV Zaitsev, AA Maksimov, II Tartakovskii, DR Yakovlev, M Bayer and A Waag. *Radiative and nonradiative recombination in type-II Zn Se/ Be Te quantum wells*. Physical Review B, vol. 76, no. 3, page 035312, 2007. (Cited on page 33.)

[Zaslow 1967] B Zaslow and Melvin E Zandler. *Two-dimensional analog to the hydrogen atom*. American Journal of Physics, vol. 35, no. 12, pages 1118–1119, 1967. (Cited on page 8.)

[Zeng 2012] Hualing Zeng, Junfeng Dai, Wang Yao, Di Xiao and Xiaodong Cui. *Valley polarization in MoS_2 monolayers by optical pumping*. Nature Nanotechnology, vol. 7, no. 8, pages 490–493, 2012. (Cited on pages 16 and 54.)

[Zeng 2015] Hualing Zeng and Xiaodong Cui. *An optical spectroscopic study on two-dimensional group-VI transition metal dichalcogenides*. Chemical Society Reviews, vol. 44, no. 9, pages 2629–2642, 2015. (Cited on page 3.)

[Zhang 2013] Wenjing Zhang, Jing-Kai Huang, Chang-Hsiao Chen, Yung-Huang Chang, Yuh-Jen Cheng and Lain-Jong Li. *High-gain phototransistors based on a CVD MoS2 monolayer*. Advanced Materials, vol. 25, no. 25, pages 3456–3461, 2013. (Cited on page 34.)

[Zhang 2015] Xiao-Xiao Zhang, Yumeng You, Shu Yang Frank Zhao and Tony F Heinz. *Experimental evidence for dark excitons in monolayer WSe 2*. Physical Review Letters, vol. 115, no. 25, page 257403, 2015. (Cited on pages 12, 13 and 48.)

[Zhang 2017] Chendong Zhang, Chih-Piao Chuu, Xibiao Ren, Ming-Yang Li, Lain-Jong Li, Chuanhong Jin, Mei-Yin Chou and Chih-Kang Shih. *Interlayer*

couplings, Moiré patterns, and 2D electronic superlattices in MoS_2/WSe_2 hetero-bilayers. Science Advances, vol. 3, no. 1, page e1601459, 2017. (Cited on pages 17, 37, 45 and 55.)

[Zhao 2013] Weijie Zhao, Zohreh Ghorannevis, Leiqiang Chu, Minglin Toh, Christian Kloc, Ping-Heng Tan and Goki Eda. *Evolution of Electronic Structure in Atomically Thin Sheets of WS2 and WSe2*. ACS Nano, vol. 7, no. 1, pages 791–797, 2013. (Cited on page 4.)

[Zhou 2018] Xing Zhou, Xiaozong Hu, Jing Yu, Shiyuan Liu, Zhaowei Shu, Qi Zhang, Huiqiao Li, Ying Ma, Hua Xu and Tianyou Zhai. *2D Layered Material-Based van der Waals Heterostructures for Optoelectronics*. Advanced Functional Materials, vol. 28, no. 14, page 1706587, 2018. (Cited on page 16.)

[Zhu 2014] C. R. Zhu, K. Zhang, M. Glazov, B. Urbaszek, T. Amand, Z. W. Ji, B. L. Liu and X. Marie. *Exciton valley dynamics probed by Kerr rotation in WSe_2 monolayers*. Physical Review B, vol. 90, no. 16, page 161302, 2014. (Cited on page 16.)

[Zhu 2015] Xiaoyang Zhu, Nicholas R Monahan, Zizhou Gong, Haiming Zhu, Kristopher W Williams and Cory A Nelson. *Charge transfer excitons at van der Waals interfaces*. Journal of the American Chemical Society, vol. 137, no. 26, pages 8313–8320, 2015. (Cited on page 16.)

[Zhu 2018] Yue Zhu, Lele Peng, Zhiwei Fang, Chunshuang Yan, Xiao Zhang and Guihua Yu. *Structural Engineering of 2D Nanomaterials for Energy Storage and Catalysis*. Advanced Materials, vol. 30, no. 15, page 1706347, 2018. (Cited on page 2.)

[Zipfel 2018] Jonas Zipfel, Johannes Holler, Anatolie A Mitioglu, Mariana V Ballottin, Philipp Nagler, Andreas V Stier, Takashi Taniguchi, Kenji Watanabe, Scott A Crooker, Peter CM Christianen, T Korn and A Chernikov. *Spatial extent of the excited exciton states in WS_2 monolayers from diamagnetic shifts*. Physical Review B, vol. 98, no. 7, page 075438, 2018. (Cited on page 57.)